

# Tuning spin-dependent transport properties of atomic-scale junctions: an *ab initio* Study

Dissertation

zur Erlangung des Doktorgrades der Naturwissenschaften  
(*Dr. rer. nat.*)

der

Naturwissenschaftlichen Fakultät II  
Chemie, Physik und Mathematik

der Martin-Luther-Universität  
Halle - Wittenberg

vorgelegt von Herrn Ilia N. Sivkov  
geb. am 2 Dezember 1987 in Krasnouralsk, Russland

angefertigt am  
Max-Planck-Institut für Mikrostrukturphysik  
Halle (Saale)

verteidigt am 03.11.2015

Gutachterin/Gutachter:

1. Prof. Dr. W. Hergert
2. PD Dr. L. Sandratskii
3. Prof. Dr. K. Kokko

Halle (Saale), 03.11.2015



## Abstract

In der vorliegenden Arbeit werden theoretische Untersuchungen der Transporteigenschaften von magnetischen Nanokontakten präsentiert und neue Methoden zur Herstellung und Kontrolle des hochspinpolarisierten Stromes und Magnetowiderstandes vorgeschlagen. Die Berechnungen wurden mit Hilfe von *ab-initio* Methoden durchgeführt, die auf der Dichtefunktionaltheorie (SIESTA, SMEAGOL) und Nichtgleichgewichts-Green-Funktionen Formalismus (SMEAGOL) basieren.

Die untersuchende, zwischen zwei Co-Elektroden hängende, Au-Atomketten zeigten hohe Magnetowiderstandratio und Spinpolarisation der Leitfähigkeit, die von der Grenzflächenhybridisierung zwischen Au und Co verursacht sind. Der Effekt ist stabil gegen geometrischen Deformationen.

Spinpolarisierte Leitfähigkeit und Strom in den platten GdN - Nanokontakten, die zwischen Cu-Elektroden platziert sind, werden untersucht. Es wurde festgestellt, dass das System ideale Spinfiltereigenschaften besitzt, was sich durch die halbmetallische Natur von GdN erklären lässt.

Am Beispiel von Fe-Pt, Fe-Pd und Fe-Rh Nanokontakten zwischen Pt, Pd bzw. Rh wurde gezeigt, dass sich die Stromspinpolarisation mit Hilfe vom Gate-Elektrode steuern lässt. Es wurde gezeigt, dass die angelegte Gate-Spannung die lokalisierten spinpolarisierten Zustände von Fe verschiebt und somit zu einer starken Änderung oder sogar Umkehrung der Stromspinpolarisation führt.

## Abstract in English

In the current work the theoretical investigations of transport properties of nano-sized magnetic contacts are presented and the new methods to obtain and control high spin-polarized current and magnetoresistance are proposed. The studies were performed by means of *ab-initio* methods based on the density functional theory (SIESTA, SMEAGOL) and the non-equilibrium Green's functions formalism (SMEAGOL).

Investigated Au atomic chain suspended between Co electrodes revealed a high magnetoresistance ratio and a spin polarization of a conductance caused by interfacial hybridization between Au and Co. This effect is found to be stable against geometry deformations.

Spin-polarized conductance and current in the plane GdN nanocontacts placed between Cu electrodes were studied. It was found that the system has ideal spin-filtering properties caused by a half-metallic nature of the GdN.

The possibility to control a current spin polarization by a gate electrode was demonstrated in the investigations of Fe-Pt, Fe-Pd and Fe-Rh nanocontacts between Pt, Pd and Rh electrodes respectively. It was shown that the applied gate voltage shifts the spin-polarized confined Fe states leading to a strong change or even an inverse of the current spin polarization.



# Foreword

In the rapidly evolving world of modern electronics, one of the priority goals is the development of technologies capable of accommodating the constant demand in rapid processing and efficient storage of exponentially growing amounts of information, generated mostly by the booming consumer electronics market, but also by various scientific big-data projects. [1, 2]

A vivid example of how technological demand can be a stimulus for fundamental research is “spintronics”, an area of solid state science and electronics dealing with the use of electron spin as an information carrier with a capability for extremely high information densities and short switching/evolution time scales (atomic dimensions setting a spatial limit in the Ångström range and evolution times of the order of attoseconds) [3]. Spintronics was born with the discovery of the GMR effect in 1988 by Fert and Grünberg and eventually led, f.e., to the creation of spin-valve devices which found successful application in memory storage and sensorics. Later, GMR based devices were replaced by more advanced magnetic tunnel junction (MTJ) ones, another product of fundamental spintronics research. While the size of the studied systems continuously shrunk, eventually reaching nano-scale dimensions, the main principle of spintronics, meticulous control of atomic spins and spin-polarized electron currents, remains the same, having endured decades of active research. Moreover it still seems to offer “plenty of room at the bottom” for more fundamental studies to come.

The present thesis is committed to researching novel possibilities of controlling spin injection and transport in atomic-scale contacts – systems of both fundamental and technological importance. The dependence of spin injection and transport on chemical composition and geometry of nano-contacts and on external influences is inspected with the eventual goal of finding ways to voluntarily tailor the latter properties for potential technological applications.

To put the presented original research in a correct frame, the first chapter of the thesis presents a brief historical overview of research done on the subject over the past decades. After a short outline of the path of spin-polarized transport from discovery to technological applications, the feasibility of controlling the latter by electronic means is discussed and a related class of systems (planar micro- and nano-scale contacts) is introduced.

This brief introduction is followed in Chapter II by a comprehensive discussion of the theoretical and calculation methodology employed in the present thesis. A brief introduction to density functional theory (DFT) is followed by an overview of state-of-the-art ways of treating electron transport with first-principles means. The chapter is finalized by a detailed description of DFT codes used in the study and a sample workflow illustrating the capabilities of the theoretical and numerical formalisms to describe electronic and magnetic properties of both simple model- and complex realistic systems.

With the stage set for the presentation of original research, Chapter III addresses the question of spin-injection in Au–Co mixed chains between Co electrodes. It is shown that efficient spin injection in pure and mixed Au/Co nano-contacts opens a path to tailoring spin-transport in purely metallic systems by tuning geometry and chemical composition of

the latter. The high spin-polarization of conductance, caused by interfacial effects between Co and Au atoms, explains the high GMR values observed in experiments. [4, 5] Moreover, we show that high spin polarization of conductance and high GMR ratios are generally robust against changes in geometry and chemical composition of both the electrodes and the chain.

As a logical continuation of the investigation related to spin-polarized current control methods, in Chapter IV electric gating – an approach widely used in electronics – is shown to be also applicable in spin-transport systems. The spin-polarization of the current through a nano-contact is shown to depend on the bias of a gate electrode brought laterally into the proximity of the junction. The effect of gate electrostatic field on the spin-polarized transport properties in mixed Fe–Pt(Pd,Rh) nano-wires is studied. The redistribution of electrons in the chain in response to the electrostatic potential imposed by the biased gate electrode is found to be strongly spin-dependent and to result in a shift of the confined states of the chain which act as transmission channels. Furthermore, the impact of the gate is found to vary for chains with linear and compressed/buckled geometries. As a result, even small gate biases are found to cause conductance changes of as much as 200%. More importantly, by adjusting the bias the spin-polarization of conductance can be enhanced, quenched or even reversed.

For the cases when planar contact geometry might be preferable to the single-atomic-junction one, in Chapter V an interesting compound, GdN, is considered as a spin filter, a choice motivated by recent experimental observations. [6] Transport properties of a junction consisting of a GdN layer sandwiched between Cu electrodes are investigated and found to depend strongly on the thickness of GdN. This thickness dependence is found to have two distinct regimes. For thick layers the conductance polarization is high and governed by the half-metallic properties of the GdN bulk, while for thin GdN layers the conductance is found to depend on the hybridization at the GdN–Cu interface and be strongly reduced thereby. In the thick-layer regime the conductance is found to have a ballistic character in majority channel and be provided for by  $p$  states of GdN, while in the minority channel the conductance has a purely tunneling character and falls off exponentially with GdN layer thickness. This allows one to tune the spin-polarization of the current to a desired value by adjusting the thickness of the GdN layer.

The thesis is completed by a short summary.

# Contents

<b>Foreword</b>	<b>iii</b>
<b>1 Introduction</b>	<b>1</b>
1.1 Spin-polarized transport in atomic-sized contacts . . . . .	1
1.1.1 From discovery to application . . . . .	1
Model descriptions . . . . .	2
Application of spin valves . . . . .	8
1.1.2 Current through atomic chains and point contacts . . . . .	8
Experimental techniques . . . . .	8
Quantized conductance . . . . .	9
Spin-polarized quantized conductance . . . . .	10
Spin-polarized conductance and magnetoresistance of nano-contacts .	11
1.2 Electric control of the transport properties of nano-contacts. . . . .	13
1.2.1 Single electron tunneling, Coulomb blockade . . . . .	13
1.2.2 Application and achievements . . . . .	15
1.2.3 Gate controlled spin-polarized current . . . . .	17
1.3 Spin polarization in planar tunnel contacts . . . . .	17
1.3.1 Amorphous barrier . . . . .	17
1.3.2 Jullier model . . . . .	18
1.3.3 Symmetry filtering barrier . . . . .	19
1.3.4 Spin-filtering materials . . . . .	20
Spin splitting of the band gap as a spin filter . . . . .	20
Determining spin polarization of the tunneling current . . . . .	21
1.3.5 Gadolinium nitride – a spin-filter material candidate . . . . .	22
<b>2 Theoretical framework of the study</b>	<b>23</b>
2.1 Many-particle problem . . . . .	23
2.2 Density functional theory . . . . .	24
2.2.1 Hohenberg-Kohn theorems and Kohn-Sham equations . . . . .	25
2.2.2 LDA and LSDA approximations . . . . .	26
2.2.3 GGA approximation . . . . .	27
2.2.4 Correlated systems, LDA+U . . . . .	27
2.3 Electron transport problem . . . . .	28
2.3.1 Landauer-Büttiker approach . . . . .	28
2.3.2 Scattering matrix . . . . .	29
2.3.3 Non-equilibrium Keldysh-Green’s functions formalism . . . . .	30
2.3.4 Non-equilibrium Green’s function method for transport calculations .	34

2.4	Calculation methods . . . . .	36
2.4.1	SIESTA . . . . .	36
2.4.2	Smeagol . . . . .	38
2.5	Typical calculation workflow . . . . .	41
<b>3</b>	<b>Spin-injection in mixed Au-Co chains between Co electrodes</b>	<b>45</b>
3.1	Calculation details . . . . .	46
3.2	Pure gold chain between cobalt electrodes . . . . .	46
3.2.1	Geometry of the system . . . . .	46
3.2.2	Magnetic moments of the junction . . . . .	47
3.2.3	Spin-polarized conductance . . . . .	47
3.2.4	Projected density of states analysis . . . . .	49
3.2.5	Magnetoresistance . . . . .	52
3.2.6	I(V) characteristics . . . . .	53
3.3	Modified Co-Au junctions . . . . .	54
3.3.1	System with mixed Co-Au electrode . . . . .	54
3.3.2	Other modifications of Au-Co junction . . . . .	56
	Mixed chains . . . . .	56
	Zigzag chain . . . . .	56
	5-atomic Au chains . . . . .	57
3.3.3	Tunnel Au-Co junction . . . . .	57
<b>4</b>	<b>Gate control of 5d-3d metal nano-contacts</b>	<b>59</b>
4.1	Settings of the calculations . . . . .	59
4.2	Fe-Pt atomic contact . . . . .	60
4.2.1	Geometry . . . . .	60
	Relaxation of the system . . . . .	61
	Gate geometry . . . . .	61
4.2.2	Magnetic configuration . . . . .	62
4.2.3	Gate influence . . . . .	62
4.2.4	Spin-polarized electron transport under bias . . . . .	64
4.2.5	Spin-dependent screening of the gate . . . . .	66
4.2.6	Analysis of the density of states . . . . .	68
4.2.7	I(V) characteristic . . . . .	71
4.2.8	The role of Pt in mixed chains . . . . .	73
4.3	Fe-Pd contact . . . . .	74
4.3.1	Geometry . . . . .	74
4.3.2	Gating Fe-Pd nano-contacts . . . . .	75
4.3.3	Transport calculations . . . . .	75
4.4	Rh-Fe atomic contact . . . . .	78
4.5	Summary . . . . .	79
<b>5</b>	<b>GdN-based systems as a spin-filter devices</b>	<b>81</b>
5.1	Details of calculations . . . . .	82
5.2	Thin GdN film between plane Cu contacts . . . . .	82
5.2.1	Geometry of the system . . . . .	82
5.2.2	Spin-polarization of conductance . . . . .	83
5.2.3	Ballistic view of transport . . . . .	84



5.2.4	Hybridization and tunneling effects . . . . .	87
5.2.5	I(V) characteristics . . . . .	88
5.3	Gd-N chains . . . . .	89
<b>Conclusions</b>		<b>93</b>
<b>References</b>		<b>94</b>
<b>Publications (Veröffentlichungen)</b>		<b>105</b>
<b>Curriculum</b>		<b>107</b>



# Chapter 1

## Introduction

### 1.1 Spin-polarized transport in atomic-sized contacts

#### 1.1.1 From discovery to application

The increased interest of the solid state physics and engineering communities in spin-polarized electron transport can be dated back to the discovery of the giant magnetoresistance (GMR) effect by Fert (1988) and Grünberg (1989). [7, 8] In both works the resistance of Fe/Cr layered systems has been studied in dependence of the magnetization alignment of the layers. By that time it was already established [9] that two Fe layers divided by a Cr spacer are antiferromagnetically coupled but could be ferromagnetically aligned by an external magnetic field. Fert and coworkers [7] observed a decrease of resistance of a Fe(001)/Cr(001) bcc superlattice [grown on GaAs(001)] by a factor of two as the Fe layers' magnetization alignment was switched from antiparallel to parallel by exposing the sample to external magnetic field. The dependence of resistivity of a material on the applied magnetic field (called “magnetoresistance”) was first reported by Thomson/Kelvin [10] in 1856. However, while *ordinary* (or *anisotropic*) magnetoresistance discovered by Thomson rarely exceeds a few percent, the effect discovered by Fert amounted to a resistance change as high as 100%. Since the resistance was found to depend on the relative alignment of Fe layer magnetizations rather than on the strength or direction of the applied magnetic field, a new measure “magnetoresistive ratio” (MRR) was used to quantitatively describe the effect. From the resistances in parallel  $R_P$  and antiparallel  $R_{AP}$  configurations the MRR can be expressed as  $MRR = (R_{AP} - R_P)/R_P \times 100\%$ .<sup>1</sup> The MRR found by Baibich and coworkers was as high as 100% which gave the effect its well-known name “giant magnetoresistance” or GMR. The system of Baibich *et al.* was constructed using the so called *current-in-plane* (CIP) geometry [see Fig. 1.1(a)], meaning that the current flowed through the device parallel to the Fe/Cr interfaces and the magnetization was directed along the [110] axis (in-plane of the Fe films). [7]

Independently, Binasch and Grünberg [8] measured an MRR of 1.5% in a CIP Fe/Cr/Fe(110) layered system, which was grown epitaxially on GaAs(110). Binasch and coworkers have found the resistance of a Fe/Cr system with three Fe layers to decrease by 3% as the magnetization alignment of Fe layers was switched from antiparallel to parallel. Moreover, with increasing Cr layer thickness, MR was found to decrease.

Both Fert and Grünberg groups independently came to a conclusion, that the difference

---

<sup>1</sup>In some definitions the  $R_{AP}$  is taken in the denominator, which usually results in lower MRR values

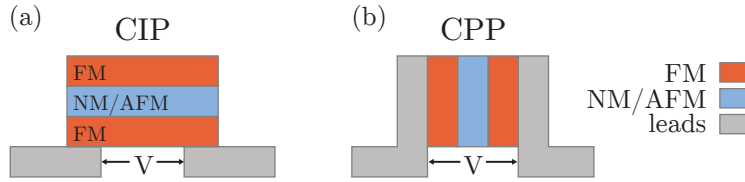


Figure 1.1: (a) CIP and (b) CPP geometries of FM/NF/FM junctions (yellow/blue/yellow colors respectively). Bias voltage  $V$  is applied to the electrodes (red color).

in resistivity was caused by spin-dependence of the transmission of the conduction electrons in a ferromagnet.

While in the original works of both Fert and Grünberg *current-in-plane* (CIP) geometry was used (Fig. 1.1a), which was mainly motivated by available sample preparation techniques, soon after the seminal publications several theoretical works [11, 12] suggested that the use of *current-perpendicular-to-plane* geometry (CPP) [Fig. 1.1(b)] should result in still larger MRR values, than those possible in CIP configuration, due to the differences in spin transport and accumulation conditions for different current orientations. Subsequent experiments [13–16] have confirmed that CPP GMR values in Fe/Cr/Fe junctions exceed several times the CIP MRR values of the same system. [17]

## Model descriptions

Since many of the main ideas put forth to describe the original planar-junction GMR experiments can also be applied to spin-dependent transport through nano-contacts (as shall be seen in the course of the present thesis) it is worthwhile to briefly introduce here the basic semiclassical picture of the GMR effect in FM/NM/FM<sup>2</sup> junctions. [11, 12, 18, 19]

The fact that spin plays a role in determining the resistivity or conductivity of a ferromagnet was introduced by Mott [20] as early as 1936, theoretically formalized by Fert and Campbell a few decades later [21, 22] and subsequently confirmed in a series of studies of different transitional metal alloys. [21–25] The experimental results could be accounted for in a simplified picture of the “two-current model”. [21, 24] The basis of the model is the assumption that charge carriers in different spin-channels ( $\uparrow$  and  $\downarrow$ ) contribute independently to the total current and experience different resistances from the material they propagate in (resistivities of  $\rho_{\uparrow}$  and  $\rho_{\downarrow}$ , respectively). Additionally, a transfer of charge carriers from one spin channel into the other is possible by spin-mixing scattering events (resistivity of  $\rho_{\parallel}$ ). Within this formalism the resistivity of a ferromagnetic conductor is expressed as

$$\rho = \frac{\rho_{\uparrow}\rho_{\downarrow} + \rho_{\parallel}(\rho_{\uparrow} + \rho_{\downarrow})}{\rho_{\uparrow} + \rho_{\downarrow} + 4\rho_{\parallel}}. \quad (1.1.1)$$

The spin-mixing term mainly originates from the electron-magnon and electron-electron exchange scatterings. The latter term is usually considered negligible. [24] Additionally, in the low temperature limit, also the spin flip scattering of the conduction electrons by magnons is frozen out, and the overall spin mixing rate becomes much smaller than the momentum relaxation rate and the resistivity of the ferromagnet can be expressed in an even shorter relation:

$$\rho = \frac{\rho_{\uparrow}\rho_{\downarrow}}{\rho_{\uparrow} + \rho_{\downarrow}}. \quad (1.1.2)$$

---

<sup>2</sup>ferromagnet/non-magnet/ferromagnet

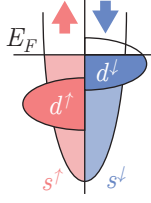


Figure 1.2: A cartoon representation of a typical transitional metal ferromagnet electronic structure. Majority/spin-up (red) and minority/spin-down (blue) densities of dispersive  $s$  and localized  $d$  electron states (DOS). At the Fermi level majority DOS is predominantly of  $s$  character, allowing for long coherence lengths. Minority  $s$ -DOS at the Fermi level are mixed with the *heavy*  $d$ -states, which allows them to be scattered into the bulk and shortens their coherence/momentum relaxation lengths.

This correspond to the situation with conduction in parallel by two independent channels as illustrated in the lower panel of Fig. 1.3(a). This simplified version of the two current model has been generally adopted in the theories of GMR and surprisingly few models take into account the spin mixing term as well.

An important quantity here is the asymmetry between the two channels which can be quantified as *spin asymmetry coefficients*  $\alpha = \rho_{\downarrow}/\rho_{\uparrow}$  or alternatively  $\beta = (\rho_{\downarrow} - \rho_{\uparrow})/(\rho_{\downarrow} + \rho_{\uparrow}) = (\alpha - 1)/(\alpha + 1)$ .

To address the physics of the difference between  $\rho_{\uparrow}$  and  $\rho_{\downarrow}$  one can consider single factors which the resistivity  $\rho_{\sigma}$  for spin channel  $\sigma$  depends on. Schematically it can be written [24] as a function of number  $n_{\sigma}$ , defining the scattering efficiency of the channel, effective mass  $m_{\sigma}$ , relaxation time  $\tau_{\sigma}$  and, most importantly, the density of states (DOS) at the Fermi level  $n_{\sigma}(E_F)$  as:

$$\rho_{\sigma} = \frac{m_{\sigma}}{n_{\sigma} e^2 \tau_{\sigma}}. \quad (1.1.3)$$

For a given type of scattering potential (without spin-flip) characterized by the matrix elements  $V_{\sigma}$  and in the Born approximation, relaxation time  $\tau_{\sigma}$  can be expressed as  $\tau_{\sigma}^{-1} \propto |V_{\sigma}|^2 n_{\sigma}(E_F)$

While the intrinsic origins of the spin dependence of  $\rho_{\sigma}$  that are related to the spin dependence of  $n_{\sigma}$  and  $m_{\sigma}$  cannot, in general, be neglected, in transition metals the strongest impact comes from the dependence of the spin relaxation rate on the Fermi level DOS ( $n_{\sigma}(E_F)$ ) in Eq. 1.1.3. The major part of the current in a metal is carried by nearly-free conduction electrons which can be scattered into the “heavy”  $d$ -states by impurities or by the atoms of the ferromagnet itself (see Fig. 1.2). The electronic structure of a typical transitional metal ferromagnet exhibits a spin-split  $d$  band. Taking as an example an element from the second half to the transitional metal row, one can expect to find a filled majority ( $\sigma = \uparrow$ ) band (residing well below the Fermi level, so that  $n_{d,\uparrow}(E_F) = 0$ ) and a partially filled minority band ( $\sigma = \downarrow$ ), residing close or at the Fermi level (high  $n_{d,\downarrow}(E_F)$ , see Fig. 1.2) so that the  $s$  states are hybridized with it and are more readily scattered/*thermalized* into the bulk. Thus there is a general intrinsic tendency for stronger scattering and larger resistivity in the spin- $\downarrow$  channel. However the largest asymmetries between  $\rho_{\downarrow}$  and  $\rho_{\uparrow}$  can be induced by extrinsic effects, in particular by impurities in form of single atoms or inter-material interfaces, which present a strong spin dependent scattering cross section. [21, 23, 24]

*Resistor model.* The two-current concept can be applied to understand the effect of GMR in layered ferromagnet(FM)/non-magnet(NM) CIP systems, where, in the limit of interlayer

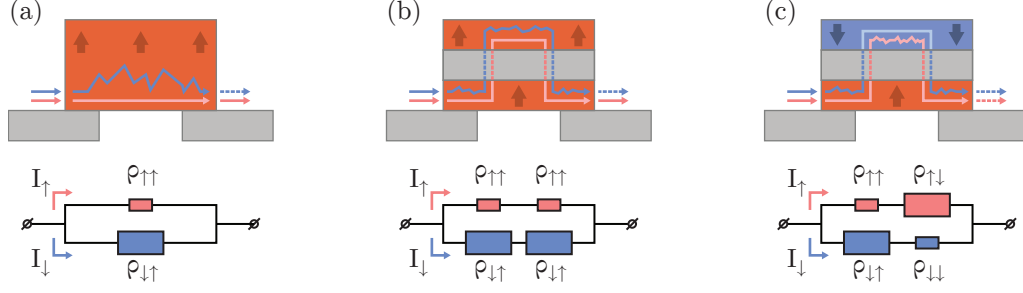


Figure 1.3: Simplified *current in plane* (CIP) scheme of the two current model of a pure ferromagnet (a) and magnetoresistive junction (FM/NF/FM) with ferro- (b) and antiferromagnetic (c) ordering of the magnetic layers. In the top sketches colors red and blue signify the two opposite magnetization orientations of the ferromagnetic layers (rectangles) and the conduction electron spins (arrows). Strait lines denote propagation with little scattering. Zig-zag lines illustrate the scattering electrons with spins co-aligned with the magnetization of the ferromagnet. In the lower sketches the top and bottom branches of the electric circuit denote the two independent currents of minority and majority electrons.

distances being much smaller than the electron mean free path, so that inter- and intra-layer scattering effects can be taken to have the same weight, the two-current concept translates into the so-called “resistor model” of GMR [Fig. 1.3(b,c)]. For the case of parallel alignment (P) of the magnetizations of neighboring ferromagnetic layers  $m$  [shown in Fig. 1.3(b)], where, without limiting the generality,  $m$  is set to  $\uparrow$ ], the junction has a high resistivity  $\rho_{\downarrow\uparrow}$  for spin- $\downarrow$  electrons in both layers, no matter how complex the actual scattering path (represented by larger resistors in the equivalent electric circuit in the lower panel of Fig. 1.3). Spin- $\uparrow$  electrons, on the contrary experience little resistance ( $\rho_{\uparrow\uparrow}$ ) in both FM layers (small resistors in the electric circuit). Neglecting of spin-flip scattering and spin-dependent processes at the interfaces of FM and NM films, the two-current model tells one that the resistivity in a ferromagnet  $\rho_{\sigma,m}$  only depends on the mutual alignment of  $\sigma$  and  $m$ . For reasons of clarity it the following notation can be introduced:  $\rho_{\uparrow\uparrow} = \rho_{\downarrow\downarrow} = \rho_+/2$  and  $\rho_{\uparrow\downarrow} = \rho_{\downarrow\uparrow} = \rho_-/2$ . Then the total resistance of the junction in P configuration can be written as:

$$r^P = \frac{\rho_+ \rho_-}{\rho_+ + \rho_-}. \quad (1.1.4)$$

For the antiparallel (AP) alignment of neighboring FM layer magnetizations [Fig. 1.3(c)] the electrons with spin- $\uparrow$  feel the resistivity  $\rho_+$  when they are scattered in the FM layer with  $m = \uparrow$  and resistivity  $\rho_-$  when their scattering path takes them into the FM layer with  $m = \downarrow$ . Again, in the limit of interlayer distance being much smaller than the electron mean free path and with no spin-flips in the system, this translates into each electron experiencing a series of alternating  $\rho_+$  and  $\rho_-$  resistivities [resistors connected serially in the equivalent electric circuit in the lower panel of Fig. 1.3(c)]. The total resistance of the junction can then be written as

$$r^{AP} = \frac{\rho_+ + \rho_-}{4}. \quad (1.1.5)$$

Now the resulting GMR ratio can be estimated as follows:

$$\text{GMR} = \frac{r^{AP} - r^P}{r^P}. \quad (1.1.6)$$

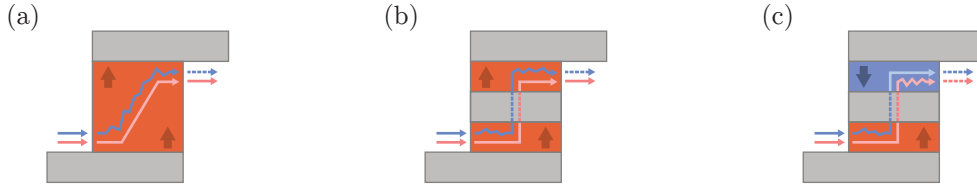


Figure 1.4: *Current perpendicular to plane* (CPP) scheme of the two current model of a pure ferromagnet (a) and magnetoresistive junction (FM/NF/FM) with ferro- (b) and antiferromagnetic (c) ordering of the magnetic layers.

Within the framework of the two-current model the same considerations hold for a junction in *current perpendicular to the layer planes* (CPP) configuration as is not hard to see from the schematic representation in Fig. 1.3. The CPP geometry has been exclusively used during the first years of the research on GMR. It was only in 1991 that GMR experiments with the CPP-GMR began to be performed. Initially this was done by sandwiching a magnetic multilayer between superconducting electrodes, [13, 16] later by electrodepositing multilayers into the pores of a polycarbonate membrane [15, 26] and, finally, evolved into the nowadays ubiquitous vertical nanostructures (pillars) fabricated by e-beam lithographic techniques. [27] In the CPP-geometry, the GMR is not only definitely higher than in CIP, as has been briefly mentioned before, but also persists in multilayers with relatively thick dimensions, up to the micron range. [25] The physics responsible for the high values and larger length scales of GMR in CPP junctions was elucidated in a model proposed by Valet and Fert. [11]

*Valet-Fert model*, is based on the assumption that spin-polarized currents flowing perpendicularly to the layers induce spin accumulation at the layer boundaries (effects described for single interfaces by Johnson and Silsbee [28]). The final result is that the length scale governing the thickness dependence of GMR becomes the *long* spin diffusion length (related to the spin relaxation) in place of the *short* mean free path in the CIP-geometry.

The physics of the spin-accumulation occurring when an electron flux crosses an interface between a ferromagnetic (F) and a nonmagnetic (N) material is sketched for a simple case (single interface, no interface resistance, no band bending, single polarity) in Fig. 1.5. In Fig. 1.5, the incoming electron flux is predominantly carried by majority electrons whereas the outgoing flux is carried equally by both spins. The result is an accumulation of spin-up electrons at the interface and this accumulation spreads out to both sides of the F/N interface to a distance of the order of the spin diffusion length ( $l_{sd}$ ). This inhomogeneity of charge distribution leads to a splitting of the spin up and spin down chemical potentials (Fermi energies) as shown in Fig. 1.5. The spin-flips incited by this out-of-equilibrium electron distribution in the spin accumulation zone serves to adjust the current imbalance between the incoming and outgoing spin currents. In short, the current spin-polarization just at the interface depends on the proportion of the polarizing/depolarizing (depending on the current flow direction) spin-flips induced by the spin accumulation.

In a multi-layer CPP-GMR junction there is an interplay between the spin accumulation effects at successive interfaces [Figs. 1.5(b) and 1.5(c)]. Spin accumulation in the non-magnetic spacer is larger for an AP magnetic configuration [Fig. 1.5(c)] in which the electrons with spins that are easily injected from a FM into NM are also the ones hard to extract into the neighboring FM with the opposite magnetization. The CPP-GMR is related to the difference in spin accumulations in the P and AP configuration.

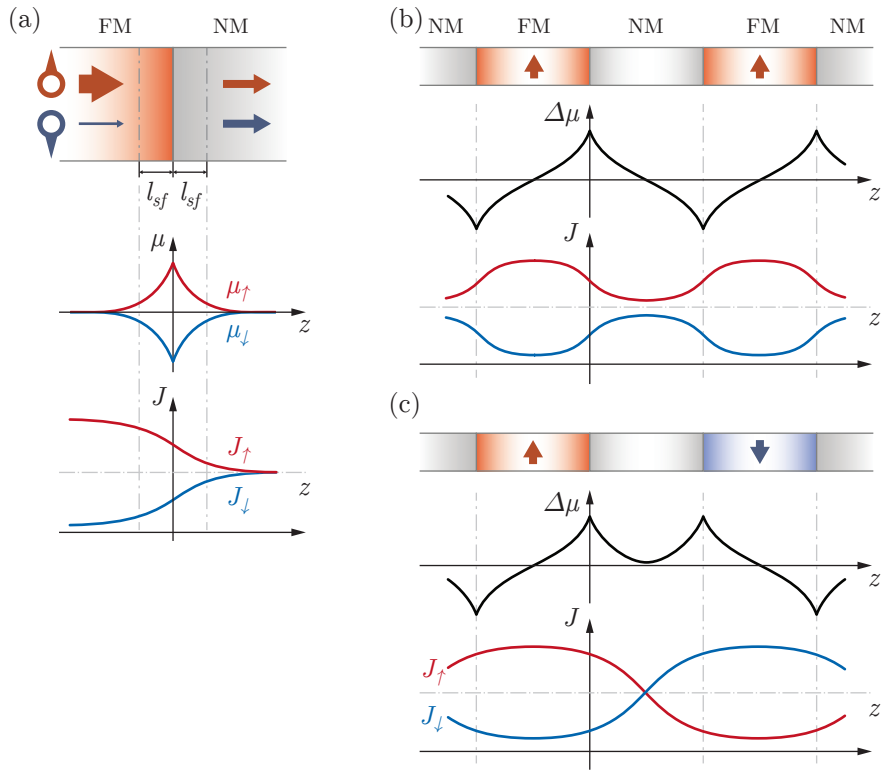


Figure 1.5: Spin-accumulation. Schematic representation of the spin accumulation at (a) an interface between a ferromagnetic metal and a non-magnetic layer and in a FM (b) and AFM (c) coupled GMR junctions. The graphs next to system sketches show the splitting of the chemical potentials of the two spin channels  $\mu^{\uparrow}$  and  $\mu^{\downarrow}$  in the vicinity of the interface due to spin accumulation and the variation of the spin-polarized current spin polarization when there is an approximate balance between the spin flips on both sides. Figure after Refs. 11 and 29.



A quantitative description of the process was given in a new types of transport equations by Valet and Fert, often called drift/diffusion equations. The electrical potential is replaced by a spin and position dependent electro-chemical potential, which is assumed to be independent for the two spin channels. The electro-chemical potentials in different layers are coupled by boundary conditions involving spin dependent interface resistances. To give an example of the application of these equation to a direct FM/FM interface where the two FM have opposite magnetization orientations, the difference between the chemical potentials  $\Delta\mu$  near the interface of those two ferromagnetic films is given by

$$\Delta\mu(z) = \frac{\beta}{1 - \beta^2} e E_0 l_{sf} \exp\left[\frac{z}{l_{sf}}\right], \quad (1.1.7)$$

where  $e$  is the electron charge,  $E_0$  is the unperturbed electric field far from the interface, which is related to full current density  $J$  as  $E_0 = (1 - \beta^2)\rho_F J$ .  $\rho_F$  is an average resistivity of the ferromagnetic film (it is similar to average resistance  $R_F$ ). The origin of coordinate  $z$  is placed at the interface between the films. Current density for spin-up  $J_\uparrow$  and spin-down  $J_\downarrow$  electrons is written as

$$J_{\uparrow(\downarrow)} = [1 \mp \beta] \frac{J}{2} \left[ 1 \pm \frac{\beta}{1 \mp \beta} \exp\left[\frac{z}{l_{sf}}\right] \right] \quad (1.1.8)$$

The splitting of chemical potentials causes accumulation of electrons with a certain spin at the interface and causes additional interfacial resistance  $r_{SI}$ , which significantly reduces current asymmetry in the system [11]

$$r_{SI} = 2\beta^2 \rho_F l_{sf}. \quad (1.1.9)$$

In the more complicate FM/NF/FM system [Figs. 1.5(b) and 1.5(c)] magnetoresistance is determined by the interfacial resistances for ( $r_{SI}^P$  and  $r_{SI}^{AP}$ ). They are written as

$$\begin{aligned} r_{SI}^P &= 2\beta^2 \frac{\rho_F \rho_N}{\rho_F \coth\left[\frac{t_N}{2l_{sf}}\right] + \rho_N \coth\left[\frac{t_F}{2l_{sf}}\right]} l_{sf}, \\ r_{SI}^{AP} &= 2\beta^2 \frac{\rho_F \rho_N}{\rho_F \tanh\left[\frac{t_N}{2l_{sf}}\right] + \rho_N \coth\left[\frac{t_F}{2l_{sf}}\right]} l_{sf}, \end{aligned} \quad (1.1.10)$$

where  $t_N$  and  $t_F$  are the thicknesses of the nonmagnetic and ferromagnetic films respectively.

It is illustrative to consider the two extreme cases, when  $t_N, t_F \ll l_{sf}$  and  $t_N, t_F \gg l_{sf}$ . In the first case the two interfaces of FM/NF/FM structure are independent from each other and, since  $\lim \coth(t_{N,F}/2l_{sf} \rightarrow \infty) \rightarrow 1$ ,

$$r_{SI}^P = r_{SI}^{AP} = 2\beta^2 \frac{\rho_F \rho_N}{\rho_F + \rho_N} l_{sf}. \quad (1.1.11)$$

Here, of course, the system does not exhibit any magnetoresistance. In the second case, assuming that  $l_{sf}/t_{N,F} \rightarrow \infty$ , one arrives at the two current resistor model introduced above, where spin-up and spin-down currents flow without spin-flip interaction.<sup>3</sup> The difference  $r_{SI}^P - r_{SI}^{AP}$ , determining absolute magnetoresistance, is then given by

$$r_{SI}^P - r_{SI}^{AP} = \beta^2 \frac{(\rho_F t_F)^2}{\rho_N t_N + \rho_F t_F}. \quad (1.1.12)$$

---

<sup>3</sup>Note, however, that this resistor model is a bit more complicate, than the one introduced above, since it takes into account the resistance of nonmagnetic layers.

This simplified picture of GMR found in ordinary magnetoresistive junctions shall serve us in the following as a fundament for the understanding for a more intricate physics leading to giant MRR ratios in atomic scale contacts, f.e. in chapter 3.

## Application of spin valves

To briefly outline the remaining history of GMR from its discovery to modern times, it has to be mentioned that the truly general interest in this effect was incited in the community by Parkin and coworkers [30] who in 1990 demonstrated the existence of GMR in multilayers (Fe/Cr, Co/Ru and Co/Cr) made by the simpler and faster technique of sputtering and explored a very broad junction/spacer thickness range finding oscillatory variation of the magnetoresistance which reflected the oscillations of the interlayer exchange coupling as a function of the spacer thickness. Perhaps even more importantly, Parkin *et al.* showed a technological way of producing magnetic sensors, which could soon be applied in magnetic hard disk drives increasing the areal recording density by almost an order of magnitude as compared to the previous generation of hard drives with anisotropic magnetoresistive (AMR) read heads (from  $\sim 5 \text{ Gb/inch}^2$  to about  $100 \text{ Gb/inch}^2$ ). [31]

Despite (or possibly because of) its tremendous technological significance, the technical limitations of the GMR junctions have quickly been reached. The spin-valves used in hard disk drive read heads typically have a GMR of no more than 15%-20% which limits the resistance sensitivity of the device. Another restriction is the field required to switch the junction from P to AP configuration. Thinner magnetic layers require higher magnetic switching field or spin torques, setting the limits for the minimal bit size and the distance needed to decouple two neighboring bits in a memory device. The need to overcome those limitations still drive both the industry and the basic research. One of the solutions lies in the use of atomic chains or atomic sized contacts as magnetoresistive junctions, whose quantum properties turn them into promising candidates for information storage applications.

### 1.1.2 Current through atomic chains and point contacts

One of the reasons atomic scale contacts are believed to be promising candidates for spintronics solutions is the extensive knowledge and know-how base in the field that has been amassed by the interest of other branches of solid state science and technology in nano-scale junctions. [32–34] Progress in experimental techniques has allowed for manipulation of individual nano-structures (down to single atoms) on surfaces and the measurement of their electron transmission or spin properties. To name just a few, novel effects of quantized spin-polarized conductance, magnetoresistance or magnetic anisotropy of atomic-sized objects opened new perspective on nano-scale spintronics (nano-spintronics). [5, 35, 36]

## Experimental techniques

Among the methods used for investigation of atomic structures two techniques are especially worth to be highlighted: scanning tunneling microscopy (STM) and mechanically controlled break junction method (MCBJ). Scanning tunneling microscope was invented by Binnig and Rohrer in 1982 [37] and is ubiquitously applied for investigation of surface morphology and electronic structure. STM technique is based on measuring a tunnel current between an investigated sample and the microscope tip, which is placed over the surface at a distance of several Ångström [Fig. 1.6(a)]. When the tip is scanned along the surface, the tunnel

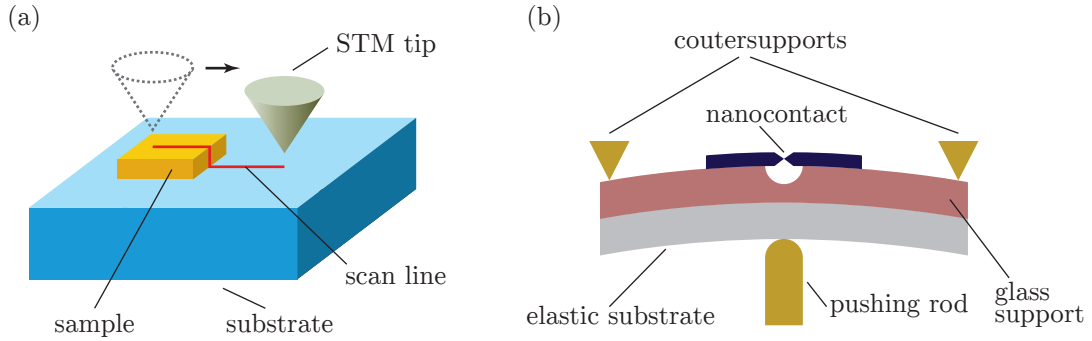


Figure 1.6: Schemes of (a) scanning tunneling microscopy and (b) mechanically controlled break junctions setups for investigation of atomic-sized structures.

current changes according to the distance between the surface and the tip and the electronic properties of the surface in the vicinity of the tip position. This way, tunneling current or differential conductance maps of the sample can be taken giving information about the apparent height or the density of states of the surface. The use of spin-polarized or superconducting tips further enables one to measure the surface properties with spin resolution, yielding information about the magnetic subsystem of the sample. [38] Since STM is not a principal part of the present thesis we shall not go into more details of the technique here, referring the reader to a number of comprehensive reviews available on the subject. [39, 40]

The second technique indispensable for the research on atomic-scale contacts is the mechanically controlled break junction technique (MCBJ). Nowadays widely used for fabrication of nano-junctions it was first proposed by Moreland and Ekin in 1985. [41] The scheme of the setup is presented in the Fig. 1.6(b). A prefabricated micro- or nano-contact is placed on a glass support, which is fixed on an elastic substrate. A three-point suspension mechanism consists of counter-supports holding the edges of the substrate and a rod, pushing up the center of the junction, thus bending the whole sample. Bending the substrate, one can meticulously control the gap formed between two tips of the nano-contact, placed above. If one continuously increases the distance between the tips in contact, one can expect a formation of an atomic wire between these tips. [34, 35] This technique allows one to measure the current or resistance (conductance) of an atomic-scale junction, but also to study transport properties in presence of magnetic fields or an electric bias created by a third (gate) electrode placed in the vicinity of the junction [42].

## Quantized conductance

A particularly interesting effect accompanying the formation of a contact with atomic dimensions is the emergence of the so-called quantized conductance with a conductance quantum of  $G_0 = 2e^2/h$ ,  $e$  being the electron charge and  $h$  – the Planck constant. The quantity  $G_0$  is a ballistic conductance of a single electron channel, [44] as shall be explained in more detailed in chapter 2. In 1995 Pascual and coworkers [43] observed quantized conductance of nano-wires created by a different technique – “drawn out” by a Pt-Ir or Au STM tip from an Au surface. Being elongated the wire showed step-like jumps in conductance, proportional to  $2e^2/h$  until the contact broke at a critical interatomic distance (Fig. 1.7). The plot of the conductance shows that right before the junction breaks its conductance equals nearly  $2e^2/h$ . Taking into account, that Au has only one  $s$  conduction band, the observation of a single-quantum conductance indicates the formation of a single-atomic gold wire spanning

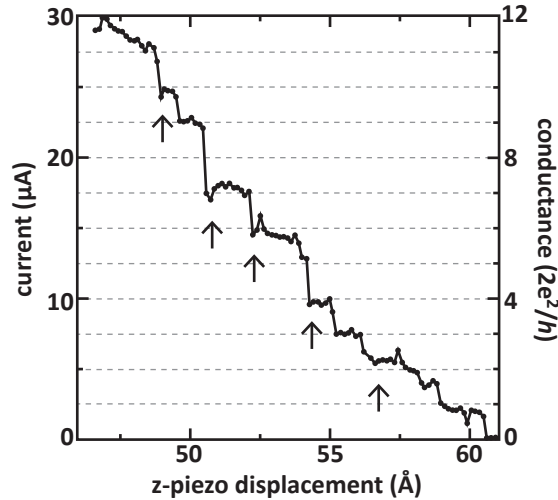


Figure 1.7: Current and conductance in a short wire ( $\sim 50$  Å) during elongation; this process exhibits room-temperature conductance quantization steps. Dashed lines denote  $2e^2/h$  intervals. Arrows indicate dips, associated with disordered elongation stages, which become somewhat less pronounced toward the breaking of the wire. Adapted from Ref. 43.

the junction. An unambiguous proof, that atomic chain contact can be reproducibly created with an STM came a few years later from Ohnishi *et al.*, [32] who managed to combine imaging of the contact geometry with conductance measurements for different thicknesses of the nano-contact fully corroborating the results and interpretation of Pascual *et al.* [43]

In another pioneering work Scheer and coworkers [34] succeeded in producing Al nano-contacts in a superconducting state using MCBJ technique. By comparing the highly non-linear current-voltage characteristics in the superconducting state with the predictions of the theory for a single channel superconducting contact the authors arrived at a surprising conclusion, that at least two channels contribute to the transport even for contacts with conductance lower than the conductance quantum  $G < G_0$ . The key to understanding this behavior was the assumption of non-ballistic character of conductance in atomic scale contacts. Then several conduction channels can exist in single atom contact, formed by different conduction states of the atom. In the case of transition non-magnetic metals, where atoms have open  $s$  and  $d$  shell, observed conductance of point contacts is often higher, than  $G_0$  and is not proportional to  $G_0$ . Here  $d$  states give non-ballistic (and non-integer) contribution to the conductance due to their strong localization and small interaction between them. [35] This finding became fundamental to the deeper understanding of the quantum nature of current through nano-scale contacts which shall also be of import for the understanding of systems and observations described in the later chapters of the present thesis.

### Spin-polarized quantized conductance

The next thing which is indispensable for the understanding of spin-polarized transmission and conductance properties of atomic-scale junctions is where the spin degree of freedom figures in the greater picture. In fact, if quantum system is considered in spin-polarized approximation, spin-up and spin-down electronic states are usually considered independent from each other. Consequently, conductance of the quantum system, according to Landauer-Büttiker formalism [44] (see chapter 2 for more details) will be represented as a sum of

conductances of spin-up and spin-down channels. Conductance quantum of one spin channel in this case equals  $G_0/2 = e^2/h$ .

It is then reasonable to assume, that it should be possible by measuring magnetic point contacts to obtain conductance of  $G_0/2$  due to the lifting of spin degeneracy. Indeed such observation have been reported in several works dealing with spin-polarized conductance of magnetic atomic contacts. [36, 45, 46] However, as has been mentioned earlier, half-integer conductance can also be caused by the non-ballistic behavior of electrons (f.e. tunneling). Magnetic transition metals, having  $s$  and  $d$  open shells can exhibit half-integer conductance but it is often not easy to obtain a clear answer as to the origin thereof. For example, low temperature Fe conductance histogram obtained with the MCBJ technique has peaks at  $2.2 G_0$ . [35, 47] Room temperature STM measurements of Ni point contact exhibit a conductance peak at about  $1.6 G_0$ . [35, 48]

Along with experimental investigations several theoretical studies of spin-dependent properties were commenced to clarify the observations, [49–55] yielding numerous interesting predictions. Standing waves, appearing in the atomic contact between electrodes were suggested to be able to cause oscillations in conductance. [49] In the same spirit, Stepanyuk and coworkers [50] discussed the relation between resonance states in the nano-wire and geometry properties thereof. Also, dependence of spin-polarized quantum conductance on geometry and chemical structure is extensively studied in the last years. It was shown, [55] that the conductance of a junction formed by a Ni STM tip approached to a Co adatom on a Co/Cu(111) island can exhibit values of  $G_0/2$  due to partially opened spin-up and spin-down channels rather than due to complete dominance of only one channel. At the same time Co adatom on a clean Cu surface revealed conductance of about  $G_0$ . These results explain experimental work of Neel [36], where the conductance  $G_0/2$  and  $G_0$  was measured in similar systems with magnetic and non-magnetic electrodes respectively.

Dal Corso *et al.* [50, 52] showed the importance of spin-orbit coupling (SOC) for quantum conductance in Pt nano-wires.<sup>4</sup> Further investigation of spin-orbit coupling and conductance in Pt atomic wires suspended between tip-shaped leads [54] revealed colossal magnetic anisotropy with an easy axis along the wire. It was found, that including SOC in calculations results in conductance values 15-20% lower than predicted by calculations neglecting the SOC. At the same time, calculations including SOC predicted for Pt wires a conduction value of ( $G \sim 2G_0$ ) which is in good agreement with experimental observations. [57–59]

## Spin-polarized conductance and magnetoresistance of nano-contacts

If it is possible to create nano-contacts with half-integer quantum conductance, or at least with different contribution to total conductance from spin-up and spin-down channels, a question arises naturally, whether such properties can be used for producing of spin-filters or spin-valves.

One of the first experimental works, showing high magnetoresistance in the atomic contacts, was performed with Ni atomic junctions by Garcia *et al.* [60] It was found, that Ni nano-contact at room temperature exhibit magnetoresistance ratios up to 280% with magnetic field of 100 Oe applied to them. Switching the magnetization alignment of Ni electrodes from antiparallel to parallel resulted in conductance changing from  $1G_0$  to  $3 \sim 4G_0$ . As in

---

<sup>4</sup>Despite Pt bulk metal having no magnetic moment, it is non-zero in wires. Pt atoms have a  $d$  shell residing close to the Fermi level. In the wire geometry reduced coordination pushes the  $d$  band closer to the Fermi level, thus causing a Stoner instability and an onset of magnetism. [56]

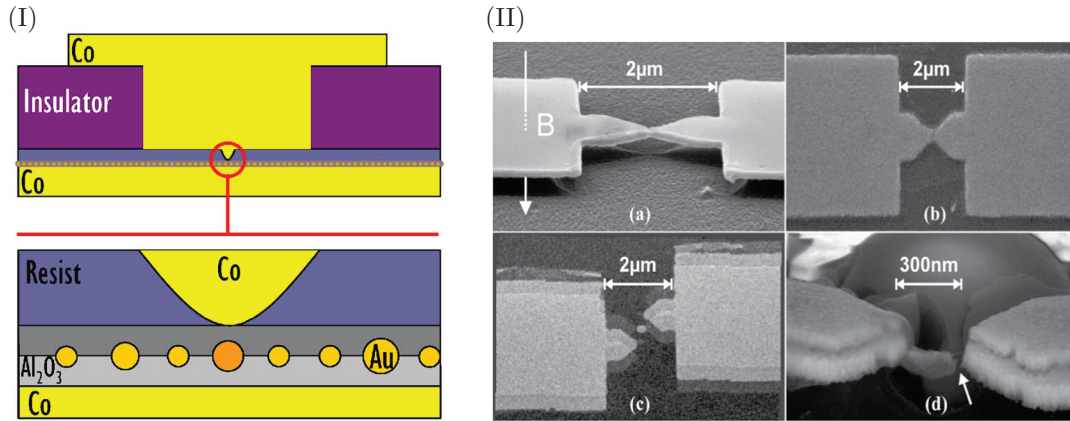


Figure 1.8: (I) Schematic cross section of the whole patterned structure showing the top/bottom Co electrodes and the 2D assembly of nanoparticles embedded in a thin alumina layer. The circle represents the zone zoomed in the bottom drawing. (From Ref. [4]). (II) Scanning electron micrographs of the different types of samples under study. (a) Inclined view of a suspended Co break junction with indication of the orientation of the magnetic field for recording the MR. (b) Top view of a nonsuspended Co bridge after measurement. The remaining break is clearly visible. (c) Top view of a Co-Au-Co sample fabricated by three-angle shadow evaporation. The Au areas appear in light gray (although partially covered by the Co layers), the Co areas are dark gray. (d) Inclined view of a Au-Co-Au sample fabricated by two-angle shadow evaporation after dismantling from the cryostat with the break visible at the right interface (arrow). Here the lower part of the metal film consists of Au, the upper parts, and the nanobridge of Co. (From Ref. [5]).

the case of planar systems studied by Fert and Grünberg, GMR in atomic Ni wire was explained by strong backscattering of electrons in the antiparallel configuration. Later, in the theoretical work Rocha *et al.* [53] have given a detailed explanation for the high magnetoresistance in Ni point contacts. Authors investigated pure and oxidized Ni atomic-wire contacts and showed that oxidation may lead to an increase in magnetoresistance from 40% in pure to 450% in oxidized Ni wires.

A class of atomic-scale contact systems bearing a closer resemblance to the original planar GMR junctions (FM/NM/FM) which should be mentioned here as it shall be the focus of chapter 3 are mixed Au-Co nano-contacts. [4, 5] Bernand-Mantel and coworkers [4] have found that transport through a paramagnetic gold cluster, embedded in an alumina layer and sandwiched between cobalt electrodes exhibits nonzero magnetoresistance, which is ascribed to the presence of spin injection from magnetic cobalt electrodes into the paramagnetic gold cluster and its subsequent spin transfer to the other electrode (Fig. 1.8(a)). Since gold has a mean spin diffusion length of about 100 nm, [61] it is not surprising that two ferromagnetic Co electrodes and an Au nano-particle should exhibit magnetoresistive behavior, especially in the tunneling geometry, which is the case in the latter experiment.

More interestingly, experiments by Egle and coworkers [5] have shown that the magnetoresistance values of a Co-Au-Co break junction (Fig. 1.8(b)) are excessively high (up to 100% in contact and 14000% in tunneling regimes respectively). This suggests that the spin injection from one cobalt electrode into the gold cluster and its coherent transfer to the detecting electrode are extremely efficient in that particular system.

It is the strive to understand the nature of this high magnetoresistance in Co-Au-Co nano-

contacts that motivated us to perform a theoretical investigation of this class of systems, which is the subject of chapter 3. We were able to relate this effect to the interfacial interaction of Co and Au electronic states, which leads to the spin-valve effect in the nano-contact.

## 1.2 Electric control of the transport properties of nano-contacts.

At present, almost any electronic device contains transistors – basic elements of current manipulation. A transistor consists of three electrodes, two of which are used as source and drain of the current while the third electrode is used to control and manipulation the latter. Transistors can be separated into two types: bipolar and field transistors. In a bipolar transistor the control of the current is performed by direct injection of current carriers into the *base* region of the device. In field transistors current from the source to the drain is controlled through potential manipulation achieved by applying a voltage/bias to the third electrode, which is called *gate*.

As nano-science progressed enough to make fabrication of nano-scale three-terminal devices feasible the idea of using the gate electrode for controlling nano-junctions became an attractive option for investigating electronic and transport properties on the atomic scale. [42, 62–69] There are several techniques for fabrication of three-terminal nanometer sized devices. [63] All of them have planar structure, where the gate is a part of a substrate, separated from the nano-contact by a dielectric decoupling layer. The first technique, which is called *electromigration* technique, is based on breaking a wire by a high density current. [64] As the tips of the wire are etched away a nano-gap or contact between two parts of the wire is formed. The second option of a technique based on depositing molecules or nano-particles into a preformed gap. The gate in the latter two approaches is represented by an Al plane with alumina insulating layer. The third technique is based on the mechanically controllable break junction method [1.6(b)] already introduced above. [42] Nano-contact is placed on a SiO<sub>2</sub> slab, grown on a Si wafer, which plays the role of a gate. This technique has an advantage of atomic wires being creation with tunable length or distance between electrodes. [42]

### 1.2.1 Single electron tunneling, Coulomb blockade

To better understand the elementary parts of the process of conduction in an atomic-scale junction and ways of controlling it with a *gate* electrode, one has to consider the basic aspects of nano-contact electronic structure and the interaction of single electrons with it. A good exemplifying subject for this is the effect of Coulomb blockade in quantum dots [63]. If the system can be viewed as quantum dot with a discrete electron spectrum connected to metallic electrodes with an infinite spectrum of an electron *band* (Fig. 1.9), the gate with an external bias applied serves to rigidly shift the quantum dot's energy levels, which can result in the quantum dot becoming charged. Since the gate has no direct contact to the dot, the degree of its influence on the dot can vary depending on the system. The relation between the energy level shift and the change of the gate voltage is called the *gate coupling parameter*  $\beta = \Delta E / \Delta V_G$ .

Energy  $E_{add}$ , required to add one electron to the system with  $N$  electrons by the definition

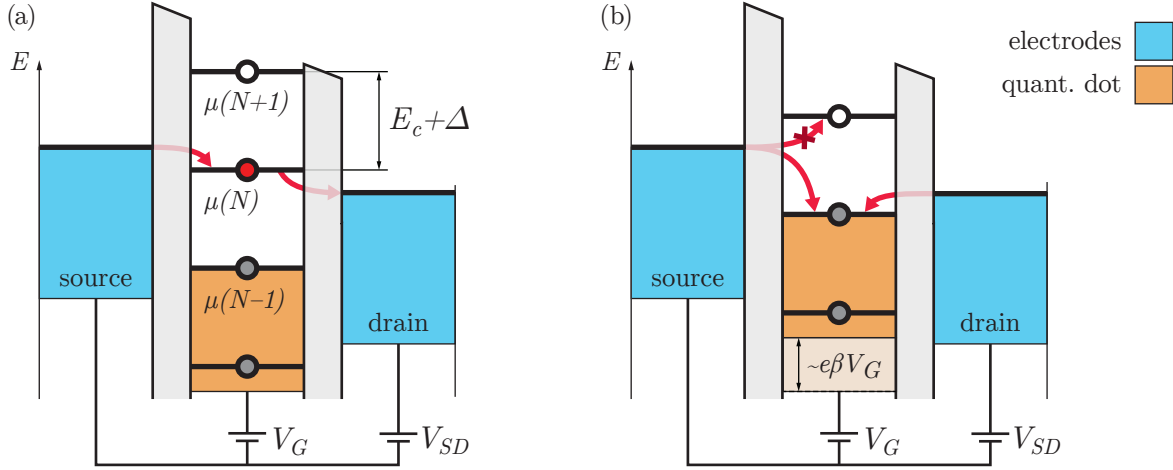


Figure 1.9: Schematic representation of the elastic transport in three electrode quantum system in (a) transmitting and (b) blocking modes. Voltage  $V_{SD}$ , applied to the source and drain causes electrons flow through the quantum dot. Current can flow only in the case, when chemical potential  $\mu(N)$  of the dot is between Fermi levels of the electrodes (a). Shift of the chemical potential is proportional to the gate voltage  $V_G$  with coefficient  $\beta$  – gate coupling parameter [63].

equals to the chemical potentials of the system with  $N + 1$  electrons. On the other hand  $E_{add} = \Delta + E_c$ , where  $\Delta$  is the distance between  $N$ th and  $(N+1)$ th energy levels  $\Delta$  of the dot,  $E_c = e^2/C$  is a charging energy,  $C$  being the full capacitance of the dot. [63, 70] If we neglect the dot's self-capacitance then the total  $C = C_S + C_D + C_G$  can be taken to be the sum of mutual capacitances  $C_S$ ,  $C_D$  and  $C_G$  of the dot with the source, drain and gate electrodes respectively. The gate coupling coefficient can be also derived through the mutual capacitances as  $\beta = C_G/(C_S + C_D + C_G)$ .

Hybridization of the quantum dot and the electrodes leads to a broadening of the dot's energy levels. If one assumes, that the dot is weakly coupled to the electrodes then the broadening is much smaller, than the distance between levels.<sup>5</sup> If the scattering of electrons in the contact can be considered elastic, the energy of the electron is conserved in the act of tunneling. In that case, at small source-drain voltage  $V_{SD}$ , tuning gate voltage  $V_G$  and measuring differential conductance  $dI/dV$ , one can obtain symmetrical narrow peaks (Coulomb oscillations), spaced by the voltage value  $E_{add}/\beta e$  [Fig. 1.10(b)], which correspond to the voltages, at which the chemical potential of the dot is aligned with the electrodes' Fermi levels (Fig. 1.9). In that regime the band diagram forms a cascade in which the current can flow through the single electronic state [single-electron tunneling, Fig. 1.9(a)]. In other cases, when chemical potential is not in between the electrodes' Fermi levels the current can not flow [Fig. 1.9]. Such effect is called Coulomb blockade, which was theoretically predicted by Averin and Likharev [71] and experimentally found by Fulton *et al.* [72]

Varying  $V_{SD}$  and  $V_G$  one can obtain so-called stability diagram [Fig. 1.10(a)], from which several important characteristics of the measured system can be deduced. Mentioned before peaks [Fig. 1.10(b)] turn into lines, separating regions with high current (gray) from the Coulomb blockade regions of zero current (black), which are called also Coulomb diamonds. Lines with positive and negative slopes correspond to chemical potential of the dot aligned

<sup>5</sup>Other possible coupling regimes are discussed in details in Ref. 63.



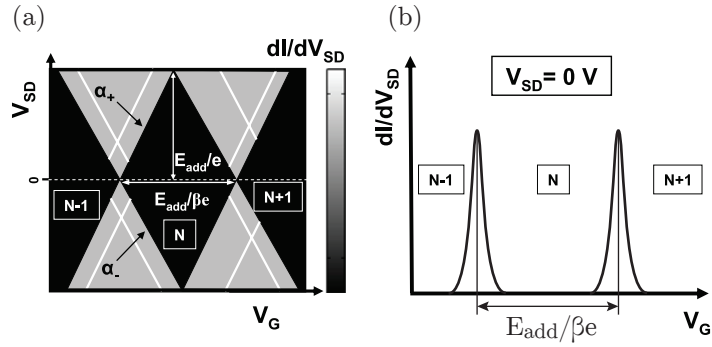


Figure 1.10: Electron transport through a weakly coupled quantum dot; the gate voltage probes three different charge states. (a) Conductance map of the differential conductance,  $dI/dV_{SD}$ , versus  $V_{SD}$  and  $V_G$  (stability diagram). The edges of the diamond-shaped regions (black) correspond to the onset of current (gray). Diagonal lines emanating from the diamonds (white) indicate the onset of transport through excited states. (b) Coulomb peaks in differential conductance,  $dI/dV_{SD}$ , versus gate voltage (small bias voltage). Adapted from Ref. 63.

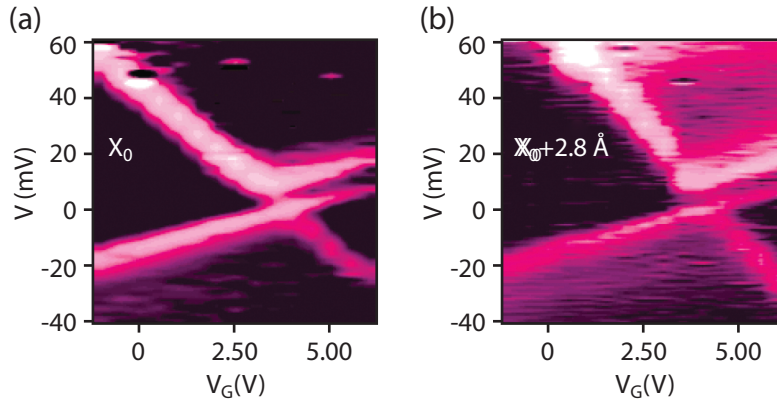


Figure 1.11: Stability diagram for C60 gated MCBJ device at 4.2 K at two positions (a and b) of source-drain displacement.  $x_0$  represents the initial displacement. From Ref. 42.

along the Fermi level of the source and drain respectively. From here positive and negative slopes can be determined as  $\alpha_+ = C_G/(C_G + C_D)$  and  $\alpha_- = -C_G/C_S$  respectively. Consequently, measuring experimentally these slopes one can determine gate coupling parameter  $\beta = \alpha_+\alpha_-/(\alpha_+ - \alpha_-)$ . In Fig. 1.10(a) one can see also white lines, which are parallel to the borders between regions of high and zero current. They represent transmission through excited states of the dot, when those appear between the Fermi levels of the electrodes. [63, 70]

## 1.2.2 Application and achievements

Discovery of single electron tunneling made it possible to create single-electron transistors (SET) [72] – devices, where tunneling current through a single state of a quantum dot is controlled by a gate bias voltage. SET found their application in various precise electronic analog devices: supersensitive electrometers, single-electron thermometers, infrared radiation detectors. [70] The use of SET in logic devices has also been extensively discussed. [70, 73, 74]

Coming back to the main subject of the present work – atomic-scale junctions – one

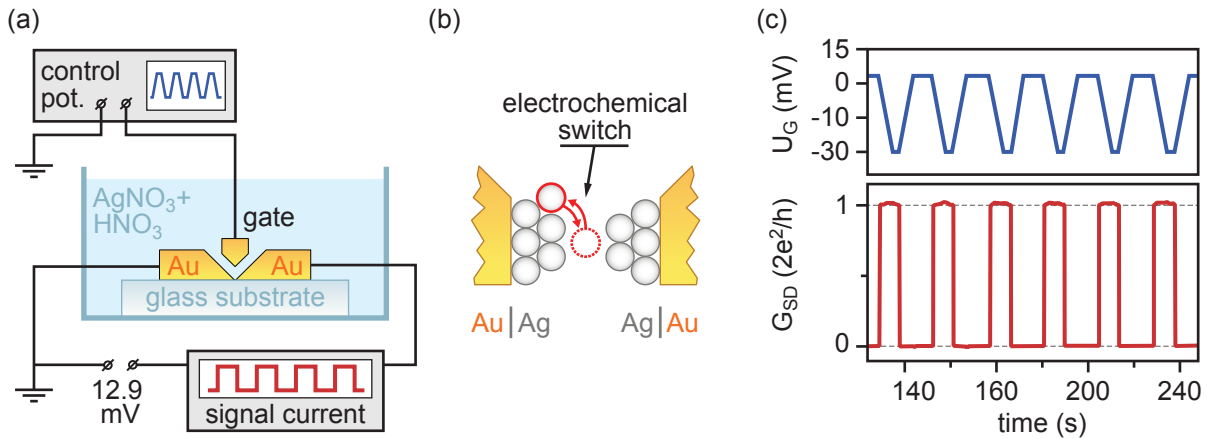


Figure 1.12: (a) Setup of a single-atom electrochemically switched transistor. Two gold electrodes brought close to each other are immersed in electrolyte and a point contact is electrochemically deposited in the gap between them. Electrodeposition is controlled by a gate bias applied to a gate electrode. (b) The deposition of the last atom bridging the contact can be reversibly controlled by the gate bias. The tunneling current is extremely sensitive to the creation or recombination of the point contact. (c) Experimentally measured tunneling current in dependence on the gate bias. Extremely fast switching times can be achieved. Adapted from Ref. 62.

experimental work is particularly worth mentioning. Champagne and coworkers [42] used the MCBJ technique to investigate transport through a  $C_{60}$  molecule enclosed between gold electrodes with a Si gate. Obtained stability diagram (Fig. 1.11) reveals Coulomb diamonds with one Coulomb oscillation peak. The gate coupling parameters determined from the slopes of the diagram lines showed that, f.e., by applying a gate voltage of  $\pm 12$  V one can obtain a shift of  $C_{60}$  molecular levels by 168 meV. It was also shown, that changing the distance between electrodes affects mutual capacitances and the energy levels of the molecule. Therefore, a single-molecule device can show interesting transistor-like properties which can be controlled not only by gate voltage, but also by varying the distance between electrodes. Such dependence of electronic and transport properties on the geometry of the system has set another accent for the work presented here.

Another type of single electron transistor was studied recently by Obermair and colleagues. [62] A silver point-contact is electrochemically deposited between two gold electrodes brought close together and immersed in electrolyte ( $AgNO_3 + HNO_3$ ). The electrodeposition is precisely controlled by a bias applied to a third gate electrode [see sketch of the experiment in Fig. 1.12(a)]. The deposition of the last Ag atom bridging the point contact creates a single-atom conduction channel [Fig. 1.12(b)]. If a voltage of 10 – 40 mV is applied across the nano-junction, the creation of the bridge can be traced by a jump in conductance from 0 to  $1 G_0 = 2e^2/h$ . The most exciting thing is that the creation of the bridge is a reversible process. By reversing the bias applied to the gate the atom bridging the junction can be removed thus decoupling the electrodes and closing the conduction channel [Fig. 1.12(b)]. Dependence of the current through such a junction of the bias applied to the gate measured by Obermair *et al.* is shown in Fig. 1.12(c). Application of an oscillating gate voltage results in a binary switching of the junction current almost instantaneously following the gate bias change. This finding presents a concept of a novel single-atom transistor which could find application in binary logic devices. The authors also note the potential of the device to reach

ultra-high switching frequencies of  $\sim 10^{12}$  Hz.

### 1.2.3 Gate controlled spin-polarized current

Since the feasibility of controlling single electron states in nano-contacts by means of electric gating is now established, one can also speculate that in magnetic system, where spin degeneracy is lifted, it might be possible to control single spin states. As the spintronics progressed, theoretical [66, 67, 69] and experimental [67, 68] investigations of gate influence on spin-polarized quantum dots in Coulomb blockade regime received more attention. For example, it was shown theoretically, [69] that tunneling magnetoresistance (TMR) in a ferromagnetic quantum dot can be significantly increased (by a factor of 2) in the Coulomb blockade regime due to high-order tunneling processes. Later, an increase of the TMR by 20% caused by the Coulomb blockade was observed experimentally in Co – Al – O granular films. [67] One should especially highlight a few of the studies, recently performed and devoted to gate-control of spin states in nano-contacts. [65, 75–77] Kim *et al.* [65] reported observing half-integer  $G_0/2$  conductance, caused by Coulomb blockade of a spin-split state in a quantum dot. In another work, Hauptmann and coworkers [75] report on the manipulation of an unpaired single spin. The spin state was read out using Kondo effect, which can be especially strong in a system with strong coupling between the quantum dot and the electrodes. Anomalous magnetoresistance effect was observed in SET constructed from Co electrodes and a carbon nano-tube as a quantum dot. [76, 78] Hysteretic dependence of conductance on external magnetic field strength did not show the usual behavior with two maxima corresponding to coercive fields, but had only one loop with two saturation levels of conductance. The authors argue that this characteristic of the junction could have useful technological applications. The origin of such untypical hysteresis is still under debate. Possible explanations could be the presence of a strong spin-orbit interaction in the nano-contact or exchange biasing of magnetic electrodes due to the formation of an antiferromagnetic oxide layer. [76, 78]

The abundance of possibilities of controlling electron transport through an atomic-scale junction was the main motivation for another part of the present thesis. In particular, in Chapter 4 the influence of gate electrostatic potential on the spin-polarized transport through transitional-metal-alloy atomic chains between metallic electrodes is studied. Strong dependence of both magnitude and sign of the spin polarization of conductance is found on the magnitude of the applied gate bias. The relation is established between such behavior and the spin-dependent charge screening, caused by the spin-polarization of the electronic structure of magnetic transitional metal atoms making up the junction. The choice of alloyed wires/chains as a test subject is not random. A careful investigation show that alloyed chains are much more sensitive to the gate field, than the pure chains, due to a stronger localization of electronic states.

## 1.3 Spin polarization in planar tunnel contacts

### 1.3.1 Amorphous barrier

Until now we have been discussing the possibilities to control spin-polarized electron transport in predominantly metallic atomic-scale junction. The main properties of the junction exploited there were the geometric factor and the matching of the electronic structures of the

constituent parts of the nano-contact. Another class of systems which cannot be ignored in a discussion of spin-polarized transport properties are layered ferromagnet/insulator junctions. The interest in them dates back to the late 1970-s, when the spin dependence of conductance in such systems was first discovered. [79, 80] Tedrow and Meservey [79] have shown in 1971 that polarization of Ni in a Al/Al<sub>2</sub>O<sub>3</sub>/Ni layered system affects the current through this system. Thereupon the authors have proposed a method for investigation of spin-dependent properties of materials [79]. Later, in 1975, Julliere [80] observed a difference of about 14% in resistances of Fe/Ge/Co junctions with parallel and antiparallel magnetization alignment of Fe and Co layers at T = 4.2 K.

After the discovery of GMR and its application in spin-valve-based devices, magnetic tunnel junctions (MTJ) started to draw attention as an alternative way to obtain high magnetoresistance values. Moodera *et al.* [81] have shown in 1995 that at room temperature CoFe/Al<sub>2</sub>O<sub>3</sub>/Co multilayers, featuring amorphous alumina (Al<sub>2</sub>O<sub>3</sub>) as an insulator, had a magnetoresistance value about 11.8%. Later studies reported reaching magnetoresistance values of 50 – 60% at room temperature in systems where CoFe electrodes were spaced by an amorphous alumina barrier. [82, 83] Another amorphous insulator layer, which was intensively studied as a candidate material for MTJ devices, is TiO<sub>x</sub>. [84–86] TMR values observed in junctions based thereon were as high as 150% at low and 15 – 20% at room temperatures. Particular MTJs used were based on La<sub>2/3</sub>Sr<sub>1/3</sub>MgO<sub>3</sub> (LSMO) electrodes with a TiO<sub>x</sub> insulator barrier in between. [84–86]

### 1.3.2 Jullier model

To describe TMR in systems with amorphous tunnel barriers Julliere proposed a model which is still ubiquitously used. [80] In systems where the insulating layer is thick enough to inhibit coherent electron transport the film can be treated as a simple energy barrier. If at the same time the system does not exhibit spin-flip scattering, the tunneling probability for the electrons is independent for the two spin channels and is proportional to the density of states (DOS) at the Fermi level in majority and minority channels of the ferromagnetic leads (Fig. 1.13). Accordingly, TMR can be expressed through the polarizations of the DOS at the Fermi level  $D(E_F)$  in the two electrodes  $P_L$  and  $P_R$  as

$$TMR = \frac{2P_L P_R}{1 - P_L P_R}, \quad (1.3.1)$$

$$P_{L,R} = \frac{D_{L,R}^{\uparrow}(E_F) - D_{L,R}^{\downarrow}(E_F)}{D_{L,R}^{\uparrow}(E_F) + D_{L,R}^{\downarrow}(E_F)}. \quad (1.3.2)$$

Using the Wentzel-Kramers-Brillouin (WKB) approximation, [87] one can also estimate the effective height of the potential barrier posed for the tunneling electrons by the isolating layer. Obtained energy barrier heights of MTJ with alumina film ranged between 0.7 and 1.0 eV. [85, 88] TiO films exhibit much lower effective barrier heights of about 0.1 eV, [85, 86] and consequently, smaller resistances, which made TiO based MTJ the main candidate for practical application in spintronic devices. For example, it allowed to reach areal data storage density of 100 – 130 Gbit/inch<sup>2</sup> in magnetic hard disk drives. [85, 89, 90]

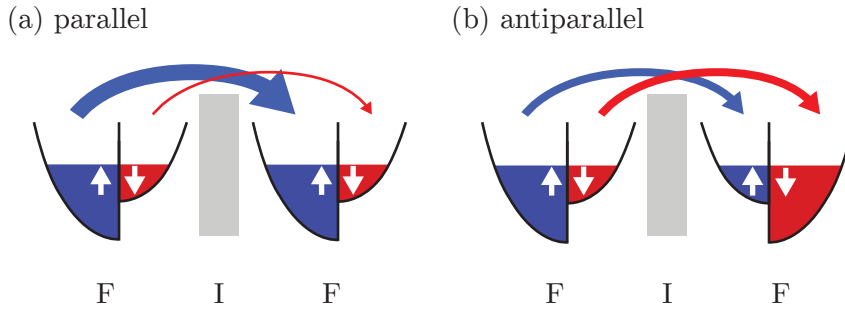


Figure 1.13: Schematic representation of ferromagnet-insulator-ferromagnet (F/I/F) MTJ in frames of Julliere model. (a) Parallel and (b) antiparallel alignment of electrodes magnetization

### 1.3.3 Symmetry filtering barrier

Despite the fact that amorphous-barrier based MTJs have found successful application, TMR of these junctions was in practice relatively low, of the order of 15 – 25%, [86, 91] which severely limited the minimum size and maximum switching speed of a single bit in a real devices.

The use of crystalline rather than amorphous barriers in MTJ junctions allowed to significantly enhance the TMR due to the symmetry-dependent scattering therein. Butler *et al.* predicted Fe/MgO/Fe junctions to have extremely high magnetoresistances, exceeding those observed in amorphous-barrier junctions by 2 to 3 orders of magnitude. [92] For physical reason for such impressive values of MRR was the fact that for parallel alignment of the lead magnetizations, conductance was provided mainly by majority  $\Delta_1$  symmetry states ( $s, p, d$ ) which have the lowest decay rate in MgO. Minority channels provide conductance through the resonance interfacial states, which are significant only for small thicknesses of the MgO layer. Antiparallel alignment of electrodes' magnetizations leads to a partial blocking of the conductance in both of spin channels due to band mismatch.  $\Delta_1$  symmetry band, existing in the spin-up channel of the first electrode, does not align with any of the bands in the spin-up channel of the second one. Note, that Julliere's model is not applicable here due to the crystal structure of the barrier and the different properties of bands with different symmetries. In general, one can say, that MgO barrier filters the current according to both the symmetry of the band and the direction of spin.

This prediction was corroborated experimentally in 2004 by Parkin *et al.* [93] MgO films grown by molecular beam epitaxy on a CoFe substrate showed TMR values up to 220% at room temperatures and up to 300% at 4K. In further investigations TMR values of up to 600% could be obtained with amorphous CoFeB electrodes and MgO tunnel barriers. [94–96] Experimentally measured dependence of the barrier resistance on the thickness of thereof gives quite low values of the effective barrier height (about 0.39 eV). [91, 96] Such low values of the barrier height promoted the use of such MTJ in real spintronic devices. In 2007 Yuasa suggested an effective technological method for commercial mass production of such MTJs which eventually led to the creation of hard disk drives with areal density exceeding 500 Gbit/inch<sup>2</sup>.

### 1.3.4 Spin-filtering materials

The main property, which leads to the high TMR values in  $\text{Al}_2\text{O}_3$  and MgO based MTJs is the active participation of the barrier itself in the process of spin-filtering of the current. In alumina-based MTJ spin polarization is provided only by the spin-polarized electronic structure of the leads, while in MgO-based MTJ both the electrodes and the barrier take part in creation of the spin-polarized current. If the efficiency of the spin-filtering by the barrier could be increased even further, f.e. by using as a barrier materials with a spin-split band gap, metallic electrodes could be even made to be non-magnetic. In this case the spin-filtering job would be performed by the tunnel barrier alone. The transport properties of such a junction are studied in Chapter. 5 by the example of a GdN tunneling barrier sandwiched between Cu leads.

Such MTJs could be used not solely in a magnetic storage device but also as a spin filter for producing spin-polarized current, which could then be used in another part of the device. For example, one of the standing problems of magnetic storage devices at present consist in finding more efficient ways of switching the magnetization direction of the leads MTJs used, e.g., in non-volatile magnetic random access memory (MRAM). Here one bit is represented by low or high resistance of an MTJ with parallel or antiparallel alignment of lead polarizations. [31, 91, 97] Currently, magnetization switching in MTJs is performed by a current-induced magnetic field, which requires large currents for practical application. A different path for switching magnetization direction in a material lies via the use of spin-transfer-torque (STT). [98–101] The latter hinges on the use spin-polarized currents. Injection of spin-polarized electrons into a ferromagnetic material causes a reorientation of the magnetization of the latter to match the spin polarization of the injected electrons (due to spin-dependent scattering).

Besides MRAM, STT found its application in the new variant of non-volatile memory – Racetrack Memory. [97–99, 102] In this case domain walls separating regions with opposite magnetization are created along a permalloy wire. Pulses of spin-polarized current created in a spin-filter are then used to move the domain walls along the wire.

We can therefore see that spin-filtering materials can play an extremely important role in a further development of novel spintronic applications.

#### Spin splitting of the band gap as a spin filter

To illustrate the concept of a spin-split band gap acting as a spin filter, one of the most successful class of spin-filtering materials studied at present can be taken as an example – semiconducting Eu chalcogenides. The first experimental work on such compounds was published by Esaki *et al.* in 1967, [103] in which the authors studied electron tunneling through EuS and EuSe layers. It was found that with temperature falling below the Curie point in both compounds the resistance of the junctions suddenly decreased. Moreover, applying magnetic field caused further decrease of the resistance at temperatures below the Curie point. Such behavior was explained by Moodera *et al.* [104, 105] In ferromagnetic (or ferrimagnetic) state below Curie temperature the band gap of the semiconductor has a spin splitting, which can be further increased by the application of a magnetic field. Because of that the tunneling probability for one of the spin channels becomes higher due to the reduction of the energy barrier. This leads to an increase in the tunneling current (Fig. 1.14). But even more important for us is the fact that along with the increase of the tunneling current the spin-polarization of the latter was also significantly increased, which was deduced

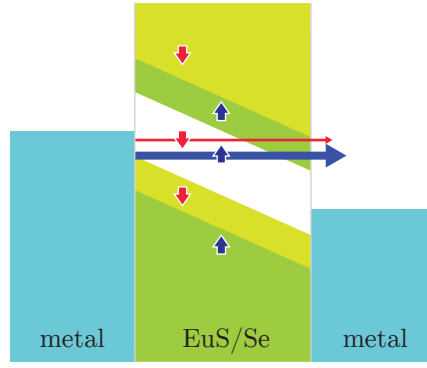


Figure 1.14: Schematic representation of Fowler–Nordheim spin-filtering mechanism of EuS or EuSe. The spin-splitting of the band structure and especially the spin-dependence of the band gap gives different transmission probabilities to electrons in different spin channels [91].

experimentally from the observation of increased TMR valued in the junction. [91] This effect received the name of Fowler–Nordheim tunneling. [106] In their theoretical treatise Moodera *et al.* estimated the spin polarization of the current in EuS and EuSe tunnel junction to be as high as 80 and 97%, respectively. [104, 105]

Note, that the influence of magnetic field is much more pronounced in EuSe than in EuS. At zero field and low temperature EuSe has an antiferromagnetic spin ordering structure which changes to ferrimagnetic or ferromagnetic in an external magnetic field. [107] This drastically changes the spin splitting of the band structure. EuS is ferromagnetic even in absence of a magnetic field and, consequently, the changes induced by the magnetic field are small.

Another Eu compound exhibiting high spin polarizations of the current is europium oxide (EuO). It was found that this compound has a larger exchange splitting than EuS and EuSe, [107, 108] although the measured current polarization was smaller in EuO than in EuS and EuSe (29%-41%). [107, 109] The authors speculate that this contradiction is due to defects appearing in the process of growth of EuO films and oxidation of EuO to  $\text{Eu}_2\text{O}_3$ , which is nonmagnetic. Recent theoretical works [110] showed excellent spin-filtering properties of ideal EuO between Cu electrodes, where spin polarization of the current reaches several hundred percent.

Understanding the concept of the gap induced spin-filtering shall help us to understand the physics of electron tunneling in GdN compounds discussed in Chapter. 5.

### Determining spin polarization of the tunneling current

According to Moodera [107], estimation of the spin polarization of the current through a tunneling barrier at low voltages can be obtained using the Simmons relation: [111]

$$J(\phi) = \left(\frac{e}{h}\right)^2 \frac{3\sqrt{2m\phi}}{2s} V \exp\left[\frac{4\pi s}{h} \sqrt{2m\phi}\right], \quad (1.3.3)$$

where  $e$  and  $h$  are electron charge and the Plank's constant,  $m$  – the mass of electron,  $s$  – the thickness of the tunnel barrier,  $\phi$  – the height of the tunnel barrier and  $V$  is the applied voltage. Applying this relation to the current above the Curie temperature, one can estimate the average effective barrier height  $\phi$ . Below the Curie point the total current is higher due to the lowering of the resistance in one of the spin channels, as was already discussed above.

The spin splitting can therefore be taken to be  $2\delta$  at low temperatures. Then taking current as a sum of spin-up  $J_\uparrow$  and spin-down  $J_\downarrow$  currents and knowing the average barrier height  $\phi$  one can apply the Simmons relation to  $J_\uparrow(\phi - \delta)$  and  $J_\downarrow(\phi + \delta)$ . The currents and spin polarization ( $SP$ ) can then be obtained from the standard relation

$$SP = \frac{J_\uparrow - J_\downarrow}{J_\uparrow + J_\downarrow}. \quad (1.3.4)$$

### 1.3.5 Gadolinium nitride – a spin-filter material candidate

As already briefly mentioned above, Chapter. 5 of the present thesis is devoted to spin-filtering properties of gadolinium nitride – another interesting compound that can be used as a tunneling barrier. It is ferromagnetically ordered with Gd showing a magnetic moment of  $7 \mu_B$  per unit cell and a half-metallic electronic structure. [6, 112–115] Minority spin channel has a gap at the Fermi level and behaves like a semiconductor, while majority channel has a semimetal electronic structure. Possible applications of the half-metallicity of GdN in a spin-filter device were already suggested by Duan and coworkers. [6] In recent works [116–118] transport properties of GdN films were investigated experimentally and Ludbrook and coworkers [116] were able to achieve a tunneling magnetoresistance ratio (TMR) of 35%. Later, Pal *et al.* and Senapati *et al.* [117, 118] reported observing a spin-polarization of conductance reaching 90% in a GdN film sandwiched between NbN electrodes.

Despite the fact that GdN was extensively studied in last years there is a definite lack of theoretical investigations of the transport and spin-filtering properties of the compound which would give a quantitative or qualitative description of the dependence of spin-filtering properties of GdN on different characteristics of the system, such as the lattice parameter or barrier thickness. In the present thesis (see chapter 5) a detailed explanation of GdN transport properties is given in dependence on the GdN layer thickness and the possibility to achieve spin-filtering efficiency of 100% is highlighted.



# Chapter 2

## Theoretical framework of the study

Let us now spend a few lines to establish the theoretical framework which shall be used throughout the remainder of the thesis. Since the main subject of the present work is spin-dependent transport of electrons from one electrode through an atomic-scale contact to another electrode, it is paramount that the theoretical treatment chosen can correctly describe three main things: the geometric shape of the system at the atomic level, its electronic structure and the transport of electrons under equilibrium and non-equilibrium conditions. Here density functional theory (DFT) shall be used to correctly capture the first two properties of the studied systems and the non-equilibrium Green's function (NEGF) method along with different model treatments shall be applied to describe the last one. This chapter starts with a very brief introduction to DFT followed by a more elaborate description of the electron scattering problem and the NEGF formalism. Finally some technical details of the implementation of the above formalisms are given.

### 2.1 Many-particle problem

The problem of correctly describing the electronic structure and as a consequence also the geometry of an atomic scale system is the problem of correctly capturing the many-electron physics with available means. The Hamiltonian of a many-particle system  $\hat{H}$ , consisting of electrons and ions, can be written as a sum of three components: electron-electron interaction  $\hat{H}_{ee}$ , ion-ion interaction  $\hat{H}_{ii}$ , and electron-ion interaction  $\hat{H}_{ei}$ <sup>1</sup>:

$$\hat{H} = \hat{H}_{ee} + \hat{H}_{ii} + \hat{H}_{ei}, \quad (2.1.1)$$

where

$$\hat{H}_{ee} = \sum_k^{N_e} \frac{-\hbar^2}{2m} \nabla_{\mathbf{r}_k}^2 + \frac{1}{2} \sum_{k \neq l}^{N_e} \frac{e^2}{|\mathbf{r}_k - \mathbf{r}_l|}, \quad (2.1.2)$$

$$\hat{H}_{ii} = \sum_K^{N_i} \frac{-\hbar^2}{2M_K} \nabla_{\mathbf{r}_K}^2 + \frac{1}{2} \sum_{K \neq L}^{N_i} \frac{Q_K Q_L}{|\mathbf{r}_K - \mathbf{r}_L|}, \quad (2.1.3)$$

$$\hat{H}_{ei} = \sum_k^{N_e} \sum_K^{N_i} \frac{e Q_K}{|\mathbf{r}_k - \mathbf{r}_K|}. \quad (2.1.4)$$

---

<sup>1</sup>Here and further we use Gaussian-CGS unit system

Here  $N_e$  and  $N_i$  are the numbers of electrons and ions in the system,  $R_K, M_K, Q_K$  are position, mass and charge of the  $K$ -th ion and  $r_k, m, e$  are position, mass and charge of the  $k$ -th electron respectively.  $\hbar$  is the Planck constant.

To obtain any observable value of the system it is “enough” to solve the many-particle Schrödinger equation, which for the case of total energies reads as

$$\hat{H}\Psi_{tot}(\mathbf{r}_{1..r_{N_e}}, \mathbf{r}_{1..r_{N_i}}) = E\Psi_{tot}(\mathbf{r}_{1..r_{N_e}}, \mathbf{r}_{1..r_{N_i}}), \quad (2.1.5)$$

The eigenvalues and eigenvectors of the Hamiltonian operator shall then give information about the states available to the system. However solving the equation exactly for all  $N_i$  ions and  $N_e$  electrons in a solid body of any significant size is unthinkable. The first approximation that is usually made to simplify the problem is the adiabatic Born-Oppenheimer approximation which hinges in the assumption that since ions have a much larger mass than electrons one can consider them “frozen” on the time scale relevant for the electronic subsystem. Under this assumption one can split the total wave-function onto ion and electron parts and solve only electron problem with ions coordinates as a parameters:

$$\hat{H}_e(\{\mathbf{r}\})\Psi_e(\mathbf{r}_{1..r_{N_e}}, \{\mathbf{r}\}) = E_e(\{\mathbf{r}\})\Psi_e(\mathbf{r}_{1..r_{N_e}}, \{\mathbf{r}\}), \quad (2.1.6)$$

where  $\Psi_e(\mathbf{r}_{1..r_{N_e}}, \{\mathbf{r}\})$ ,  $\hat{H}_e(\{\mathbf{r}\})$  and  $E_e(\{\mathbf{r}\})$  are the wave function, Hamiltonian and eigenenergy of the electron subsystem respectively and  $\{\mathbf{r}\}$  – the set of ions coordinates, taken as parameters. Then the electronic Hamiltonian can be represented a Hamiltonian of electrons moving in an external potential  $V_{ei}$  produced by the ions.

$$\hat{H}_e(\{\mathbf{r}\}) = \sum_k^{N_e} \frac{-\hbar^2}{2m} \nabla_{\mathbf{r}_k}^2 + \frac{1}{2} \sum_{k \neq l}^{N_e} \frac{e^2}{|\mathbf{r}_k - \mathbf{r}_l|} + V_{ei}(\{\mathbf{r}\}), \quad (2.1.7)$$

$$V_{ei}(\{\mathbf{r}\}) = \sum_k^{N_e} \sum_K^{N_i} \frac{eQ_K}{|\mathbf{r}_k - \mathbf{r}_K|}. \quad (2.1.8)$$

Having ions out of the picture one is still left with an equation congaing a vast number of variables. Solving Eq. 2.1.7 analytically is an impossible task and this is where the density functional theory shows its usefulness.

## 2.2 Density functional theory

Taking a careful look at Eq. 2.1.7 one can notice that the main problem in solving it lies in the term describing the electron-electron interaction. First attempts to approximate the problem resulted in the creation of the Thomas-Fermi and the Hartree models. [119, 120] The ideology of the approach is somewhat akin to the Born-Oppenheimer approximation in that the many-body Schrödinger equation is reduced to the equation describing the evolution of a single electron in an effective potential field created by all the other electrons via the electron-electron interaction. The Hohenberg-Kohn density functional theory (being an exactification of both the Thomas-Fermi and the Hartree theories) was developed by Kohn and Hohenberg around 1964 [121]. It recasts the problem of the solution of a many-electron Schrödinger equation in terms of the electronic density distribution  $E[n(\mathbf{r})]$  and a universal functional of the density  $E_{xc}[n(\mathbf{r})]$ . Thus it becomes possible to replace the necessarily approximate solution of a many-body Schrödinger equation by a problem of finding adequate approximations to the exchange functional and then solving a single-particle electronic equation.

### 2.2.1 Hohenberg-Kohn theorems and Kohn-Sham equations

The basis of the density functional theory are the two Hohenberg-Kohn theorems, which justify the use of electron density  $n(\mathbf{r})$  as a key object of the system instead of its many-body wave function. [121]

**Theorem 1** states that *the electron density  $n(\mathbf{r})$  of the system of  $N$  electrons moving in an external potential  $v(\mathbf{r})$  is a unique functional of the latter potential and vice versa.*

This theorem implies, that both Hamiltonian and total energy of the system are also unique functionals of the electron density:

$$E[n] = \langle \Psi | \hat{H}[n] | \Psi \rangle = \int v(\mathbf{r})n(\mathbf{r})d\mathbf{r} + F[n], \quad (2.2.1)$$

where  $F[n(\mathbf{r})]$  is an unknown, but otherwise universal functional of the electron density  $n(\mathbf{r})$  only.

**Theorem 2.** *For a given external potential  $v(\mathbf{r})$  and number of particles  $N$  there is a functional  $F[n]$  such, that  $E[n]$  in Eq. 2.2.1 gives the ground state energy for the correct ground state electron density  $n(\mathbf{r})$ .*

Functional  $F[n]$  can be written as

$$F[n] = \langle \Psi, (T + U)\Psi \rangle, \quad (2.2.2)$$

where  $T$  and  $U$  are the kinetic energy and the Coulomb interaction operators,  $\Psi$  is the ground state wave-function of the system. It is convenient to extract the *classical* Coulomb energy from  $U$ , so that the ground state energy can be written as

$$E[n] = \int v(\mathbf{r})n(\mathbf{r})d\mathbf{r} + \frac{e^2}{2} \int \frac{n(\mathbf{r})n(\mathbf{r}')}{|\mathbf{r} - \mathbf{r}'|} d\mathbf{r}d\mathbf{r}' + T[n] + E_{xc}[n]. \quad (2.2.3)$$

Here the second term is the *classical* Coulomb energy and the third term is the kinetic energy of noninteracting electrons. Fourth term is an *exchange-correlation* energy, which is the *non-classical* part of Coulomb interaction.

For practical use Kohn and Sham derived a set of equations similar to the single-particle Schrödinger equation. [122] Assuming a constant number of particles

$$\int n(\mathbf{r})d\mathbf{r} = N, \quad (2.2.4)$$

one needs to find  $n(\mathbf{r})$ , which minimizes  $E[n]$ :

$$\delta \{E[n] - \mu N\} = 0, \quad (2.2.5)$$

where  $\mu$  is a Lagrange multiplier (or physically the chemical potential). The last equation can be rewritten as

$$\int \delta n(\mathbf{r}) \left\{ \varphi_{\text{eff}}(\mathbf{r}, n[\mathbf{r}]) + \frac{\delta T[n]}{\delta n(\mathbf{r})} \right\} d\mathbf{r} = 0. \quad (2.2.6)$$

Here, effective potential  $\varphi_{\text{eff}}(\mathbf{r}, n[\mathbf{r}])$  comprises external, Coulomb and exchange-correlation potentials:

$$\varphi_{\text{eff}}(\mathbf{r}, n[\mathbf{r}]) = v(\mathbf{r}) + e^2 \int \frac{n(\mathbf{r}')}{|\mathbf{r} - \mathbf{r}'|} d\mathbf{r}' + \frac{\delta E_{xc}[n]}{\delta n(\mathbf{r})} - \mu. \quad (2.2.7)$$

Then, equation (2.2.6) is rewritten as

$$\frac{\delta T[n]}{\delta n(\mathbf{r})} + \varphi_{eff}(\mathbf{r}, n[\mathbf{r}]) = 0. \quad (2.2.8)$$

This equation can be seen as an equations of motion of noninteracting electrons in an effective potential  $\varphi_{eff}(\mathbf{r}, n[\mathbf{r}])$  with kinetic energy, represented by the first term. The solution of the equation can be provided by the Schrödinger equation

$$\left\{ \frac{-\hbar^2}{2m} \nabla^2 + \varphi_{eff}(\mathbf{r}, n[\mathbf{r}]) \right\} \psi_i(\mathbf{r}) = \epsilon_i \psi_i(\mathbf{r}), \quad (2.2.9)$$

where the electron density is

$$n(\mathbf{r}) = \sum_i^{N_e} |\psi_i(\mathbf{r})|^2. \quad (2.2.10)$$

These two equations are called Kohn-Sham equations and are meant to be solved self-consistently. The difficulty in this problem is that the exchange-correlation potential  $\mu_{xc} = \delta E_{xc}[n]/\delta n(\mathbf{r})$  while formally exact cannot realistically be evaluated in a simple. Thus, as already remarked at the end of the previous section, finding adequate simplification to  $E_{xc}[n(\mathbf{r})]$  is essential for DFT to be a useful tool.

## 2.2.2 LDA and LSDA approximations

Since it is impractically hard if not impossible to calculate exchange-correlation potential exactly, one usually resorts to certain approximations of that functional. One of the simplest ones is the so called the *local density approximation (LDA)*, proposed by Kohn and Sham [122] for systems with slowly-varying electron density. One can expand exact exchange-correlation energy of the system in powers of density gradient and taking first term, one can write:

$$E_{xc}[\mathbf{r}] = \int \epsilon_{xc}(n(\mathbf{r}))n(\mathbf{r})d\mathbf{r}. \quad (2.2.11)$$

This is equivalent to an assumption that the exchange-correlation energy of an electron at position  $\mathbf{r}$  is the same as the exchange-correlation energy of an electron in a uniform electron gas of density  $n(\mathbf{r})$ . Exchange-correlation potential is then calculated as:

$$v_{xc}(\mathbf{r}) = \frac{\delta \{ \epsilon_{xc}(n(\mathbf{r}))n(\mathbf{r}) \}}{\delta n(\mathbf{r})}. \quad (2.2.12)$$

Dependence of  $\epsilon_{xc}(n(\mathbf{r}))$  on  $n(\mathbf{r})$  can be formalized fitting exact calculations of exchange-correlation energy to the homogeneous electron gas model. Some of the methods and descriptions thereof can be found in Refs. 123 and 124. Surprisingly, such crude approximation gives quite good agreement with experiments for many systems. Most of them are metals, where the density of electrons indeed varies slowly in space.

In the case of spin-polarized systems, the energy depends on spin-up  $n_\uparrow$  and spin-down  $n_\downarrow$  electron densities as:

$$E[n_\uparrow, n_\downarrow] = T[n_\uparrow, n_\downarrow] + \int v_{ext}(\mathbf{r})n(\mathbf{r})d\mathbf{r} + \frac{e^2}{2} \int \int \frac{n(\mathbf{r})n(\mathbf{r}')}{|\mathbf{r} - \mathbf{r}'|} d\mathbf{r} d\mathbf{r}' + E_{xc}[n_\uparrow, n_\downarrow], \quad (2.2.13)$$

where the total density is  $n(\mathbf{r}) = n_{\uparrow}(\mathbf{r}) + n_{\downarrow}(\mathbf{r})$ . Exchange-correlation potential for majority or minority channel is calculated as a variational derivative with respect to majority or minority electron density respectively:

$$\mu_{xc}^{\uparrow(\downarrow)}(\mathbf{r}) = \frac{\delta E_{xc}[n_{\uparrow}(\mathbf{r}), n_{\downarrow}(\mathbf{r})]}{n_{\uparrow(\downarrow)}(\mathbf{r})}. \quad (2.2.14)$$

In LDA approximation for spin-polarized systems (LSDA) exchange-correlation potential for spin-up or spin-down channel depends locally on the majority or minority electron density. There are several realizations, based on LDA functionals. [125, 126]

### 2.2.3 GGA approximation

As the LDA approximation performs well in and was developed predominantly for systems with slow-varying electron density, in many real systems, such as atoms or molecules, where electron density experiences strong oscillations, LDA is not applicable. Then the second order of the exchange-correlation expansion, taking into account the variation of electron density through the gradient thereof, can be used. It is called *generalized gradient approximation* and has the form

$$E_{xc}^{GGA} = \int f(n_{\uparrow}, n_{\downarrow}, \nabla n_{\uparrow}, \nabla n_{\downarrow}) d\mathbf{r}. \quad (2.2.15)$$

This approximation allowed to obtain results, for example, for molecules, such as ground state energies or geometries, which are in good agreement with experiments. One of the most successful parametrizations of the GGA functional to date belongs to Perdew, Burke and Ernzerhof (PBE). [127]

### 2.2.4 Correlated systems, LDA+U

One of main problem of LDA consists in it failure to correctly describe strongly-correlated systems. For example, for  $d$  or  $f$  shells of many elements the mean-field character of LDA approximation does not capture the strong localization of the orbitals. The idea of correction to the LDA approximation, suggested in 1991 by Anisimov, Zaanen and Andersen, [128] is to add an orbital-dependent potential  $U$  to the LDA energy in Hubbard form, that describes Coulomb interaction of strongly-correlated shell

$$E_C = \frac{1}{2}U \sum_{i \neq j} n_i n_j, \quad (2.2.16)$$

where  $n_i(j)$  are the occupancies of the orbitals. Since if this form is used, the total energy of Coulomb interaction happens to be accounted for twice, it should be subtracted, for which a *double-counting correction* can be used in the following form:

$$E_{dc} = \frac{1}{2}UN(N - 1), \quad (2.2.17)$$

where  $N = \sum_i n_i$  is the total number of electrons in the considered system or subsystem. Resulting total energy of the system can be written as

$$E_{LDA+U} = E_{LDA} + \frac{1}{2}U \sum_{i \neq j} n_i n_j - \frac{1}{2}UN(N - 1). \quad (2.2.18)$$

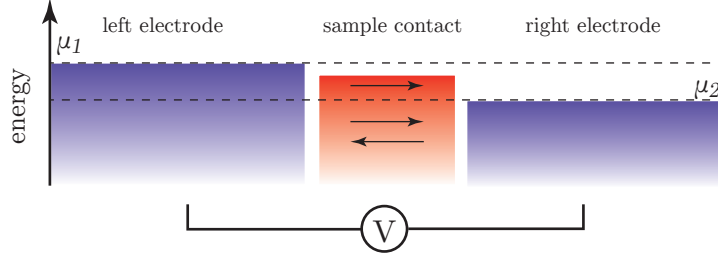


Figure 2.1: Schematic view of two-electrode system under the bias.

The energies of orbitals can be found as derivatives of  $E_{LDA+U}$  with orbital occupancies  $n_i$ :

$$\epsilon_i = \epsilon_{LDA} + U\left(\frac{1}{2} - n_i\right). \quad (2.2.19)$$

Orbital-dependent single-particle effective potential has a similar form:

$$v_i(\mathbf{r}) = v_{LDA}(\mathbf{r}) + U\left(\frac{1}{2} - n_i\right). \quad (2.2.20)$$

One can see that both energy and potential have discontinuities at integer numbers of particles. According to Refs. 129 and 130 this jumps reflect the behavior of exact DFT potential, while LDA potential has continuous dependence on the orbital occupations. Therefore, one can say that  $U$  correction allows to restore the exact behavior to the LDA potential.

Besides  $U$  the LDA+ $U$  formalism has another parameter  $J$  which is responsible for the exchange interaction in correlated shells. Exact treatment requires the considered Coulomb and exchange interactions to be considered to be orbital-dependent ( $U_{mm'}$  and  $J_{mm'}$ ). In that case the single-particle potential can be written as

$$\begin{aligned} V_{m\sigma}(\mathbf{r}) = & V_{LDA}(\mathbf{r}) + \sum_{m'} (U_{mm'} - U_{eff})n_{m-\sigma} + \\ & + \sum_{m \neq m'} (U_{mm'} - J_{mm'} - U_{eff})n_{m\sigma} + U_{eff} \left(\frac{1}{2} - n_{m\sigma}\right) - \frac{1}{4}J \end{aligned} \quad (2.2.21)$$

A more detailed descriptions of these methods can be found in Ref. 131. Correct choice of DFT treatment is indispensable for reliable description of the ground state electronic properties. In our case correctly capturing the electronic structure of the nano-scale junctions shall be the basis for the correct description of the electron transport therein.

## 2.3 Electron transport problem

### 2.3.1 Landauer-Büttiker approach

In our treatment of electron transport through atomic-scale junctions we shall rely on the transport formalism of Landauer and Büttiker [44], which is based on the idea that the conductance of a system consisting of a contact between two leads is determined by scattering properties (electrons transmission probability) of the contact. The current between electrodes (reservoirs) in this interpretation, in turn, can be caused by the difference between the chemical potentials of the latter. The basic concepts of Landauer-Büttiker formalism can be

illustrated by a simple example of a two-electrode system with chemical potentials  $\mu_1$  and  $\mu_2$ , which are shifted with respect to each other due to applied bias voltage  $V = (\mu_1 - \mu_2)/(-e)$  (Fig. 2.1), where  $e$  is the electron charge. We consider elastic scattering, so that the energy of electrons *passing* through the contact is conserved. Therefore the contribution to the current from electrons with energies of less than  $\mu_2$  being scattered from right to left and from left to right electrodes cancel each other out. In the energy range  $\mu_2 < E < \mu_1$  they are injected from the left electrode into the contact area and can then tunnel on to the right electrode. The resulting current is then: [131]

$$I_{inj} = \frac{2e^2V}{h}, \quad (2.3.1)$$

where  $h$  is the Planck's constant. If we assume that the transmission probability of the contact  $T$  is not dependent on the energy, then we can write, that the total current is  $I = TI_{inj}$ . From here we arrive at Landauer's formula for the conductance of a system as

$$C = \frac{I}{V} = \frac{2e^2T}{h}. \quad (2.3.2)$$

For a contact with one conduction channel, which has ballistic transport properties,  $T = 1$  (*ideal transmission*) and this equation gives a value of  $G_0 = 2e/h$  called "the conductance quantum". One can observe such conductance values in the periodic systems, such as chains, where each conduction band gives contribution  $G_0$  to the conductance in the case of spin-degenerate states or  $G_0/2 = e^2/h$  per spin.

A more general formula for current taking into account the energy dependence of transmission  $T(E)$  can be written as an integral over  $E$  from  $\mu_2$  to  $\mu_1$ . If further the occupation of electron states of the left(right) electrodes are determined by Fermi (or other temperature dependent) distribution functions  $f_{l(r)}(E, t)$  the integration limits  $[\mu_1, \mu_2]$  are replaced by  $(-\infty, \infty)$  and equation (2.3.1) takes the form [131]:

$$I = \frac{2e^2}{h} \int_{-\infty}^{\infty} T(E) (f_l(E - \mu_1) - f_r(E - \mu_2)) dE. \quad (2.3.3)$$

### 2.3.2 Scattering matrix

As we have seen, to determine conductance and current of a system, we need to calculate the system's transmission probability  $T$ . There are several ways to do that. First of all, we consider a one-dimensional toy model and a method, based on the scattering matrix approach, to show the connection between scattering properties and conductance.

Let  $\psi_{in}(x)$  be the state of a particle (free electron, e.g.) with a wave number  $k$ , approaching a rectangle potential barrier  $V(x)$  (Fig. 2.2). The state of the particle after scattering is  $\psi_{out}(x)$ . Then, in terms of plane waves we can write

$$\begin{cases} \psi_{in}(x) = A_1 e^{ikx} + B_1 e^{-ikx} \\ \psi_{out}(x) = A_2 e^{-ikx} + B_2 e^{ikx} \end{cases} \quad (2.3.4)$$

If we put  $B_1 = 0$ , then we have only incoming wave from left. Outgoing wave consists of transmitted and reflected waves with coefficients  $B_2$  and  $A_2$  respectively. We can define reflection and transmission amplitude as:

$$r_{11} = \left( \frac{A_2}{A_1} \right)_{B_1=0} \quad \text{and} \quad t_{21} = \left( \frac{B_2}{A_1} \right)_{B_1=0}, \quad (2.3.5)$$

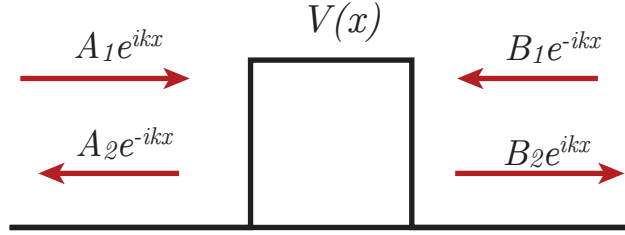


Figure 2.2: One dimensional scattering problem

respectively. If  $A_1 = 0$ , then we have incoming wave from right, so:

$$r_{22} = \left( \frac{B_2}{B_1} \right)_{A_1=0} \quad \text{and} \quad t_{12} = \left( \frac{A_2}{B_1} \right)_{A_1=0} \quad (2.3.6)$$

A matrix, composed from these coefficients gives us a connection between incoming and scattered states and is called  $S$  - *matrix* or scattering matrix:

$$\hat{S} = \begin{pmatrix} r_{11} & t_{12} \\ t_{21} & r_{22} \end{pmatrix}, \quad \begin{pmatrix} A_2 \\ B_2 \end{pmatrix} = \hat{S} \begin{pmatrix} A_1 \\ B_1 \end{pmatrix} \quad (2.3.7)$$

In this case we can define the conductance from left to right as  $C_{21} = \frac{e^2}{h} |t_{21}|^2$ , where  $e$  is the electron charge and  $h$  - the Planck's constant. In general, when the system has a complex structure and many available channels including spin channels, coefficients  $t$  and  $r$  can themselves be matrices, depending on energy. In that case, according to Landauer-Büttiker formalism, total transmission is defined as:

$$T(E) = \sum_{\sigma} \sum_i T_{i\sigma}(E) = \sum_{\sigma} Tr[\hat{t}_{\sigma}(E)\hat{t}_{\sigma}^{\dagger}(E)], \quad (2.3.8)$$

where  $\sigma$  denotes the spin channel and  $T_{i\sigma}$  is the transmission probability of  $i$ -th channel and  $\sigma$ -th spin direction. Then the zero-bias conductance can be defined as

$$C = \frac{e^2}{h} T(E_f) = \frac{G_0}{2} T(E_f). \quad (2.3.9)$$

Here  $G_0 = \frac{2e^2}{h}$  is again the unit of quantum conductance. The total conductance can be calculated using Eq. (2.3.3) and Eq. (2.3.2).

### 2.3.3 Non-equilibrium Keldysh-Green's functions formalism

In the first approximation, the states of the leads are often considered unchanged by the process of electron transmission (current flow). This assumption is especially valid for small biases, when the system is not brought far out of the equilibrium. For larger biases or for systems with an intricate electronic structure at the Fermi level (sensitive chemical potential) a more elaborate approach is necessary, taking into account the dynamics (in a sense, the time dependence) of conductance.

In quantum mechanics, the time dependence can be treated in Schrödinger, Heisenberg or interaction pictures. If we take the Hamiltonian of the non-equilibrium system to be  $\hat{H}(t) = \hat{H}_0 + \hat{V}(t)$ , where  $\hat{H}_0$  is the (known) Hamiltonian of the equilibrium system, which



does not depend on time, and  $\hat{V}(t)$  is the non-equilibrium part, carrying the time dependence. The transformation of wave functions and operators from the Schrödinger to the interaction pictures is then made by

$$\begin{aligned} |\psi_I(t)\rangle &= e^{i\hat{H}_0 t} |\psi_S(t)\rangle \\ \hat{A}_I(t) &= e^{i\hat{H}_0 t} \hat{A}_S(t) e^{-i\hat{H}_0 t} \end{aligned}$$

where  $|\psi_I(t)\rangle$  and  $|\psi_S(t)\rangle$  are the wave functions in the interaction and the Schrödinger pictures respectively. The Heisenberg and interaction pictures are connected via the perturbation  $\hat{V}(t)$ . The transformation rule can be expressed through the evolution operator  $\hat{S}(t, t')$ , which depends on the perturbation in the interaction picture  $\hat{V}_I(t)$ : [132]

$$\hat{S}(t, t') = \begin{cases} \sum_{n=0}^{\infty} (-i)^n \int_{t > \tau_n > \dots > \tau_1 > t'} d\tau_n \dots d\tau_1 \hat{V}_I(\tau_n) \dots \hat{V}_I(\tau_1) = \hat{T} \exp \left\{ -i \int_{t'}^t \hat{V}_I(\tau) d\tau \right\} & , t > t' \\ \sum_{n=0}^{\infty} i^n \int_{t < \tau_n < \dots < \tau_1 < t'} d\tau_n \dots d\tau_1 \hat{V}_I(\tau_n) \dots \hat{V}_I(\tau_1) = \hat{\hat{T}} \exp \left\{ i \int_t^{t'} \hat{V}_I(\tau) d\tau \right\} & , t < t' \end{cases} \quad (2.3.10)$$

where  $\hat{T}$  is time-ordering operator, which arranges the operators  $\hat{V}_I(\tau_n)$  according to time  $\tau_n$  in the integration, as we expand the exponent into the Taylor's series. Respectively, operator  $\hat{\hat{T}}$  orders the operators in reverse order. Note, that operator  $\hat{S}$  is unitary  $\hat{S}(t, t') = \hat{S}^{-1}(t', t)$  and has group properties  $\hat{S}(t, t') \hat{S}(t', t'') = \hat{S}(t, t'')$ . Such arrangement is needed due to the non-commutative properties of perturbation  $\hat{V}_I(t)$  at different time points. Therefore, relation between the Heisenberg and the interaction pictures for wave functions takes the form

$$|\psi_I(t)\rangle = \hat{S}(t, -\infty) |\psi_I(-\infty)\rangle \equiv \hat{S}(t, -\infty) |\psi_H\rangle, \quad (2.3.11)$$

where  $|\psi_H\rangle$  is a wave function in the Heisenberg pictures. We can declare the Heisenberg wave function as equal to the wave function in the interaction picture in the past at  $t = -\infty$ , before the perturbation  $\hat{V}(t)$  was *switched on*. Transformation rule for the operators can then be written as

$$\hat{A}_H(t) = \hat{S}(-\infty, t) \hat{A}_I(t) \hat{S}(t, -\infty). \quad (2.3.12)$$

Here we also imply, that  $\hat{A}_I(-\infty) = \hat{A}_H(-\infty)$ .

As we see, operator  $\hat{S}$  determines the evolution of the wave functions and operators in time from  $-\infty$  to  $t$ , which can be regarded as a transformation between Heisenberg and interaction pictures.

A many-body quantum system can be described in the framework of Green's functions formalism. The Green's function is expressed through field operators in the Heisenberg picture  $\hat{\psi}_H(r, t)$  as

$$G(r, t; r', t') = -i \text{Tr} \left\{ \rho_0 \hat{T} \left[ \hat{\psi}_H(r, t) \hat{\psi}_H^\dagger(r', t') \right] \right\}, \quad (2.3.13)$$

where  $\rho_0$  is the density matrix in the Heisenberg picture, taken by our convention at time  $t = -\infty$ , when the system is in equilibrium steady state (perturbation  $\hat{V}(-\infty) = 0$ ).

Let us consider the equilibrium and non-equilibrium Green's functions. If we switch the perturbation  $\hat{V}(t)$  on adiabatically starting from  $t = -\infty$  then the system always stays in an equilibrium steady state  $|\Phi(t)\rangle$  and the Green's function can be written as an average in this state instead of using the trace of the density matrix. In the interaction picture, using the  $\hat{\hat{S}}$  operator:

$$G(r, t; r', t') = \left\langle \Phi_I(\infty) \left| \hat{\hat{T}} \left[ \hat{\hat{S}}(\infty, -\infty) \hat{\psi}_I(r, t) \hat{\psi}_I^\dagger(r', t') \right] \right| \Phi_I(-\infty) \right\rangle. \quad (2.3.14)$$

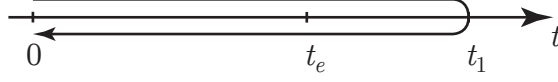


Figure 2.3: Closed integration contour  $C_0$

Here one can use a trick to replace the state  $\langle \Phi_I(\infty) |$  at time  $t = \infty$  by the state at time  $t = -\infty$  using the  $\hat{S}$  operator. [131, 132] It can be done due to the assumption, that system is always in equilibrium state and the states of the system differ only by a phase factor. Therefore:

$$G(r, t; r', t') = \frac{\langle \Phi_I(-\infty) | \hat{T} [\hat{S}(\infty, -\infty) \hat{\psi}_I(r, t) \hat{\psi}_I^\dagger(r', t')] | \Phi_I(-\infty) \rangle}{\langle \Phi_I(-\infty) | \hat{S}(\infty, -\infty) | \Phi_I(-\infty) \rangle}. \quad (2.3.15)$$

Such view of the Green's function simplifies calculations, since the quantum state of the system at time  $t = -\infty$  can be assumed known.

Nevertheless, the adiabatic limit is not always applicable. In the non-adiabatic case the system is not in equilibrium state and one can not apply the simplification to Eq. (2.3.14). Instead, the exact transformation

$$\langle \Phi_I(\infty) | = \langle \Phi_I(-\infty) | \hat{S}(-\infty, \infty) \quad (2.3.16)$$

has to be substituted into expression (2.3.14). Operator  $\hat{S}$  then has, according to (2.3.10), inverse time-ordering, since it propagates the state from  $\infty$  to  $-\infty$ . Being placed to the left and outside the direct time-ordering operator  $\hat{T}$  (see Eq. (2.3.17)) it cannot be brought into the square brackets, since it has reverse time ordering by the definition (2.3.10). Therefore, at first, we have direct time-ordered integration from  $-\infty$  to  $\infty$ , then the inverse one from  $\infty$  to  $-\infty$ . Such time-ordered integration can be considered as integration along a contour  $C$  (denoted as  $\hat{T}_c$ ), which is called Schwinger-Keldysh contour, [133, 134] with evolution matrix  $\hat{S}_c$ :

$$\begin{aligned} G(r, t; r', t') &= -i \langle \Phi_I(-\infty) | \hat{S}(-\infty, \infty) \hat{T} [\hat{S}(\infty, -\infty) \hat{\psi}_I(r, t) \hat{\psi}_I^\dagger(r', t')] | \Phi_I(-\infty) \rangle \\ &= -i \langle \Phi_I(-\infty) | \hat{T}_c [\hat{S}_c(-\infty, -\infty) \hat{\psi}_I(r, t) \hat{\psi}_I^\dagger(r', t')] | \Phi_I(-\infty) \rangle \\ &= -i \text{Tr} \left\{ \rho_0 \hat{T}_c [\hat{S}_c(-\infty, -\infty) \hat{\psi}_I(r, t) \hat{\psi}_I^\dagger(r', t')] \right\} \end{aligned} \quad (2.3.17)$$

where we replaced the average in state  $|\Phi_I(-\infty)\rangle$  by an average with trace of the density matrix in the past  $\rho_0 = \rho(-\infty)$  which are equivalent, since in the past the system has a well-defined equilibrium ground state. It is not necessary to know the density matrix  $\rho(-\infty)$ , if we know it at time  $t = 0$ , which is already earlier than  $t_e = \min(t, t')$ , we can perform the integration along a closed contour  $C_0$ , starting at  $t = 0$  and ending at  $t = 0$ . The latest time point of the integration can be chosen as  $t_l = \max(t, t')$  (Fig. 2.3).

As a result, we can write the Green's function with a closed contour time ordering

$$G(r, t; r', t') = -i \text{Tr} \left\{ \rho(0) \hat{T}_c [\hat{S}_c(0, 0) \hat{\psi}_I(r, t) \hat{\psi}_I^\dagger(r', t')] \right\}. \quad (2.3.18)$$

Let us denote the integration contour as  $C$  with forward  $C_+$  and backward  $C_-$  branches. On this contour our Green's function can be written as a set of real-time Green's functions

without contour ordering operations

$$G(r, t; r', t') = \begin{cases} G^T(r, t; r', t') = -i \left\langle \hat{T} \left[ \hat{\psi}_H(r, t) \hat{\psi}_H^\dagger(r', t') \right] \right\rangle & , t, t' \in C_+ \\ G^<(r, t; r', t') = i \left\langle \hat{\psi}_H^\dagger(r', t') \hat{\psi}_H(r, t) \right\rangle & , t \in C_-, t' \in C_+ \\ G^>(r, t; r', t') = -i \left\langle \hat{\psi}_H(r, t) \hat{\psi}_H^\dagger(r', t') \right\rangle & , t \in C_+, t' \in C_- \\ G^{\tilde{T}}(r, t; r', t') = -i \left\langle \hat{\tilde{T}} \left[ \hat{\psi}_H(r, t) \hat{\psi}_H^\dagger(r', t') \right] \right\rangle & , t, t' \in C_- \end{cases} \quad (2.3.19)$$

where  $\hat{T}$  and  $\hat{\tilde{T}}$  are forward and backward time-ordering operators respectively. One can introduce Green's functions obtained as linear combinations of the above functions which are called "Keldysh rotations": [134, 135]

$$\begin{aligned} G^R &= G^T - G^< = G^> - G^{\tilde{T}}, \\ G^A &= G^T - G^> = G^< - G^{\tilde{T}}, \\ G^K &= G^> + G^< = G^T + G^{\tilde{T}}, \end{aligned} \quad (2.3.20)$$

where  $G^R$  and  $G^A$  are retarded and advanced Green's functions,  $G^K$  is Keldysh-Green's function. In more detailed view they can be written as

$$\begin{aligned} G^R(r, t; r', t') &= -i\Theta(t - t') \left\langle \left\{ \hat{\psi}_H(r, t) \hat{\psi}_H^\dagger(r', t') \right\} \right\rangle, \\ G^A(r, t; r', t') &= i\Theta(t' - t) \left\langle \left\{ \hat{\psi}_H(r, t) \hat{\psi}_H^\dagger(r', t') \right\} \right\rangle, \\ G^K(r, t; r', t') &= \left\langle \left[ \hat{\psi}_H(r, t) \hat{\psi}_H^\dagger(r', t') \right] \right\rangle. \end{aligned} \quad (2.3.21)$$

If Green's function  $g$  of a non-perturbed system is known, then to obtain the Green's function of an interacting system  $G$  one need to solve the Dyson equation: [131, 136]

$$\begin{aligned} G &= g + g\Sigma G = g + G\Sigma g, \\ G &= (g^{-1} - \Sigma)^{-1}, \end{aligned} \quad (2.3.22)$$

where  $\Sigma$  is the self-energy, which includes the perturbation of the system. Regarding to mentioned above  $G^R$ ,  $G^A$  and  $G^K$ , using Langreth rules, [131, 137, 138] one can show, that

$$\begin{aligned} G^K &= G^R \Sigma^K G^A, \\ G^{\lessgtr} &= G^R \Sigma^{\lessgtr} G^A. \end{aligned} \quad (2.3.23)$$

This equation is a special case of the Keldysh quantum kinetic equation for the non-equilibrium Green's function, used in mesoscopic transport.

Usually, the transport problem is considered as a stationary one, so the Green's functions depends only on the time difference  $t - t'$ . Therefore, it is convenient to perform a Fourier transformation of the quantities and to work in energy (frequency) domain with a parameter  $E$  instead of  $t - t'$ . Retarded and advanced Green's functions due to their analytic properties in upper and lower half planes respectively have a simple form in the  $E$ -domain, which makes their calculation simpler. In operator view one can write

$$\begin{aligned} \hat{G}^R(E) &= \frac{1}{E - \hat{H}_0 - \hat{\Sigma}^R(E)} = \hat{G}^A(E)^\dagger, \\ \hat{G}^K(E) &= \hat{G}^R(E) \hat{\Sigma}^K(E) \hat{G}^A(E), \\ \hat{G}^{\lessgtr}(E) &= \hat{G}^R(E) \hat{\Sigma}^{\lessgtr}(E) \hat{G}^A(E). \end{aligned} \quad (2.3.24)$$

Note, that  $\Sigma^R$  and  $\Sigma^A$  have also analytic properties in upper and lower half planes respectively, while  $G^K$ ,  $G^{\lessgtr}$ ,  $\Sigma^K$  and  $\Sigma^{\lessgtr}$ , in general, could have non-analytic features in both half planes.

In the equilibrium case, when the system has a well-defined chemical potential  $\mu$ , one can show, that

$$\begin{aligned}\hat{G}^K(E) &= [1 - 2f(E - \mu)][\hat{G}^R(E) - \hat{G}^A(E)], \\ \hat{G}^<(E) &= -f(E - \mu)[\hat{G}^R(E) - \hat{G}^A(E)], \\ \hat{G}^>(E) &= [1 - f(E - \mu)][\hat{G}^R(E) - \hat{G}^A(E)],\end{aligned}\tag{2.3.25}$$

where  $f(E)$  is the Fermi distribution function.

### 2.3.4 Non-equilibrium Green's function method for transport calculations

In two preceding section we have briefly introduced a way to use the non-equilibrium Green's function (NEGF) method for calculation of the transmission probability of the system and the Landauer-Büttiker approach for calculation of current and conductance. Now we shall apply the NEGF method to the calculation of conductance of the same model system as discussed in Sec. 2.3.1 (two electrodes and a contact between them, as shown in Fig. 2.1). Here we give a general explanation of the approach [131], and the particularities of its realization in the transport code "Smeagol" shall be given later.

Model Hamiltonian of the system can be written as

$$\hat{H}(t) = \hat{H}_c + \sum_{i=L,R} [\hat{H}_i + \hat{V}_i(t)],\tag{2.3.26}$$

where  $\hat{H}_c$  is a Hamiltonian of the contact,  $\hat{H}_i$  are the Hamiltonians of the left and the right electrodes/reservoirs  $i = L, R$  and  $\hat{V}_i(t)$  are the interactions between the contact and the electrodes. These quantities can be written in the second quantization notation as

$$\begin{aligned}\hat{H}_c &= \sum_{q',q} \epsilon_{q'q} \hat{c}_{q'}^\dagger \hat{c}_q, \\ \hat{H}_i &= \sum_{k_i} \epsilon_{k_i} \hat{c}_{k_i}^\dagger \hat{c}_{k_i}, \\ \hat{V}_i &= \sum_{k_i,q} J_{k_i q}(t) \hat{c}_{k_i}^\dagger \hat{c}_q + \text{H.c.}\end{aligned}\tag{2.3.27}$$

Here electrodes are assumed to be in equilibrium state, so their Hamiltonians can be diagonalized and written in a second quantization form through the eigenvalues  $\epsilon_{k_i}$ .

Let  $g_{k_i}^R$  and  $g_{k_i}^K$  be the retarded and Keldysh Green's functions of the electrodes in diagonal representation with respect to eigenstates, numbered by  $k_i$

$$\begin{aligned}g_{k_i}^R(t - t') &= -i\Theta(t - t')e^{-i\epsilon_{k_i}(t-t')}, \\ g_{k_i}^K(t - t') &= -i[1 - 2f_i(\epsilon_{k_i})]e^{-i\epsilon_{k_i}(t-t')}.\end{aligned}\tag{2.3.28}$$

In absence of a direct interaction between electrodes the self-energies of the latter can be expressed as

$$\Sigma_{q'q,i}^{R/K}(t, t') = \sum_{k_i} J_{q'k_i}(t') g_{k_i}^{R/K}(t - t') J_{k_i q}(t).\tag{2.3.29}$$

If the interaction between the electrodes and the contact does not depend on time, one can make a Fourier transformation of the Green's functions, as has been done in the previous section. Using the relation between retarded, advanced and Keldysh Green's functions in equilibrium (2.3.25), the relation between the self-energies of the electrodes may be written as

$$\begin{aligned}\hat{\Sigma}_i^K(E) &= [1 - 2f(E - \mu)][\hat{\Sigma}_i^R(E) - \hat{\Sigma}_i^A(E)], \\ \hat{\Sigma}_i^<(E) &= -f(E - \mu)[\hat{\Sigma}_i^R(E) - \hat{\Sigma}_i^A(E)], \\ \hat{\Sigma}_i^>(E) &= [1 - f(E - \mu)][\hat{\Sigma}_i^R(E) - \hat{\Sigma}_i^A(E)].\end{aligned}\tag{2.3.30}$$

Thus, Keldysh lesser (<) and greater (>) self-energies can be obtained from the retarded or advanced ones, which can be calculated, in turn, as matrix products of the electrodes' Green's functions and the interaction part of the Hamiltonian, using relation (2.3.29). Often, the quantity  $\hat{\Gamma}_i(E) = i[\hat{\Sigma}_i^R(E) - \hat{\Sigma}_i^A(E)]$ , called the *broadening matrix* or *hybridization function*, is used in the notation, which can be treated as a quantity describing the hopping of electrons from the electrodes onto the contact. As the hybridization function is just a complex part of the self-energy it describes the effect the electrodes have on the central contact. In the simplest case, hybridization function shows the broadening of the levels of the contact.

Now one can write an expression for the lesser Green's function of the contact<sup>2</sup> from Eq. (2.3.24):

$$\hat{G}_C^<(E) = -i\hat{G}^R(E) \sum_{i=L,R} \hat{\Sigma}_i^<(E)\hat{G}^A(E).\tag{2.3.31}$$

From Eq. (2.3.29) we can see, that self-energies and, consequently, Green's function of the contact depend only on the basis states of the contact numbered by  $q$ . Since investigated sample contacts are usually small atomic-sized object, its basis-set has a limited number of basis functions. Therefore, Green's function matrix  $G_{q'q}$  (retarded, Keldysh, lesser,... etc.) has a relatively small size, which allows to use this method in numeric computations.

Finally we should determine the physical quantities which have importance in the analysis of the electronic properties of quantum systems. Time dependent occupation of the system's states is given by

$$n_q(t) = \langle \hat{c}_q^\dagger(t)\hat{c}_q(t) \rangle = -i G_{qq}^<(t, t') |_{t=t'}.\tag{2.3.32}$$

In the stationary case one can calculate the density of states projected onto the basis state  $q$  through the retarded Green's function after Fourier transformation to the energy domain

$$D_q(E) = -\frac{1}{\pi} \Im[G_q^R(E)].\tag{2.3.33}$$

The current can be found using Eq. (2.3.3), where the transmission is determined by the formula of Fisher and Lee: [139]

$$T(E) = \text{Tr} \left[ \hat{\Gamma}_L \hat{G}_C^A \hat{\Gamma}_R \hat{G}_C^R \right].\tag{2.3.34}$$

---

<sup>2</sup>Keldysh and greater Green's functions look the same

## 2.4 Calculation methods

### 2.4.1 SIESTA

For the calculation of electronic structure in the present work the code SIESTA was used. [140, 141] The code is based on the density functional theory (DFT) and uses localized atomic orbitals (LCAO) as a basis-set, which is constructed using Troullier-Martins pseudopotentials [142] and Kleinman-Bylander projectors. [143] To achieve good completeness of the basis each atomic orbital can be represented as a sum of several numeric radial functions (called  $\zeta$ -s). [141, 144, 145] SIESTA, as is usual for DFT codes, uses a self-consistent loop where the initial guess of charge distribution is used for calculation of the energy spectrum and the new wave functions, which are then utilized for calculation of the charge distribution, which is used as the new input to the cycle.

Let us mention a few important aspects of the SIESTA method. In many cases one can split electrons in atoms into two parts: valence electrons, which occupy the *outer* orbitals and take part in chemical interactions and bonding, and core electrons, occupying lower orbitals and resisting external influences. To exclude from the computation these core electrons and reduce computational cost SIESTA uses pseudopotentials, which represent the nuclear potential ( $\sim 1/r$ ) screened by the core electrons. In this case pseudopotential  $V_l$  depends on the angular momentum of the orbital, and has a non-local form (one can say, that the potential becomes an operator). Usually core electrons have small radii of their orbitals, and therefore, the pseudopotential differs from the real all-electron potential one only inside some small radius  $r_{core}$ . Using as an input the semi-local Troullier-Martins pseudopotential [142] the form of the potential can be transformed into a fully nonlocal one by the method of Kleinman-Bylander. The operator of the semilocal pseudopotential can be transformed to

$$\hat{V}_{PS} = V_{local}(r) + \hat{V}^{KB}, \quad (2.4.1)$$

where

$$\hat{V}^{KB} = \sum_{l=0}^{l_{max}^{KB}} \sum_{m=-l}^l \sum_{N=1}^{N_l^{KB}} |\chi_{lmn}^{KB}\rangle v_{ln}^{KB} \langle \chi_{lmn}^{KB}|, \quad (2.4.2)$$

where  $|\chi_{lmn}^{KB}\rangle$  is the projector of Kleinman-Bylander and

$$\begin{aligned} v_{ln}^{KB} &= \langle \phi_{ln} | \delta V_l(r) | \phi_{ln} \rangle, \\ \delta V_l(r) &= V_l(r) - V_{local}(r), \\ \chi_{lmn}^{KB}(r) &= \delta V_l(r) \phi_{ln}(r) Y_{lm}(\hat{r}). \end{aligned} \quad (2.4.3)$$

Here  $Y_{lm}(\hat{r})$  is spherical harmonic,  $\phi_{ln}(r)$  are transformed eigenstates of the atom with semilocal pseudopotential (see Ref. 143). Potential  $V_{local}$  is chosen to be equal  $V_l$  for  $r > r_{core}$ . Consequently,  $\delta V_l(r) = 0$  for  $r > r_{core}$  and the Kleinman-Bylander projectors are zero for these distances. Therefore one needs to care only about long range  $V_{local}$ , while the projectors have very localized form and can be easily calculated.

Another important thing, that we should consider are the basis functions. Since in the atomic systems electron states can change their form due to interactions, it could be not enough to have atomic orbitals as a basis-set. For polarized orbitals, one can include additional orbital with higher angular momentum into the basis-set. This can be done by including Kleinman-Bylander projector with angular momentum  $l + 1$ , where  $l$  is an

angular momentum of the considered polarized orbital. Second way to account polarization of the orbitals is chosen to solve atomic Schrödinger equation with an electric field. Found eigenstate with momentum  $l + 1$  is added to the basis.

To have more flexibility in radial dependence of the basis functions SIESTA uses the so-called “split-valence” scheme, initially developed in quantum chemistry. [146] The idea is to include in the basis additional radial function (multiple  $\zeta$ -basis). This function by construction reproduces the tail of the atomic orbital for  $r > r_s$ , where  $r_s$  is a “split-radius”, and has smooth behavior for  $r < r_s$ . Let  $\phi_l^{1\zeta}(r)$  be the main atomic orbital, then  $\phi_l^{2\zeta}(r)$  component in SIESTA is parameterized as: [141, 144, 145]

$$\phi_l^{2\zeta}(r) = \begin{cases} r^l(a_l - b_l r^2), & r < r_s \\ \phi_l^{1\zeta}(r), & r \geq r_s \end{cases} \quad (2.4.4)$$

Taking into account the previous considerations, within the frameworks of SIESTA Schrödinger’s equation with DFT Hamiltonian  $\hat{H}$  of the quantum system can be written as

$$\hat{H} \sum_i \psi_i(r) = \hat{S} \sum_i \psi_i(r), \quad (2.4.5)$$

where  $\hat{S}$  is an overlapping matrix, since the LCAO basis used is not necessarily orthogonal. The Hamiltonian itself has the form of

$$\hat{H} = \hat{T} + \sum_i \hat{V}_i^{KB} + \sum_i V_i^{local}(r) + V_H(r) + V_{xc}(r), \quad (2.4.6)$$

where nuclear and core electron potentials are represented by the local  $V_i^{local}(r)$  and non-local  $\hat{V}_i^{KB}$  pseudopotentials described above.  $\hat{T} = -\frac{\hbar^2}{2m} \nabla^2$  is the kinetic energy operator.  $V_H(r)$  and  $V_{xc}(r)$  are the Hartree and exchange-correlation potentials of the electron system. Summation is done over the atom index  $i$ .

Matrix elements of operators  $\hat{T}$ ,  $\hat{V}$  and  $\hat{S}$  can be partially calculated in reciprocal space and stored in memory for further use, which significantly reduces the time of calculation. Matrix elements of the other Hamiltonian terms  $\sum_i V_i^{local}(r)$ ,  $V_H(r)$ ,  $V_{xc}(r)$  are calculated on a real-space grid. Moreover, potential  $V_i^{local}(r)$  is transformed by adding to it a potential created by valence electrons of the atom  $V_i^{atom}(r)$ . Therefore, resulting potential

$$V_i^{NA} = V_i^{local}(r) + V_i^{atom}(r) \quad (2.4.7)$$

is a potential of a neutral atom and it equals zero outside the sphere with radius  $r_{c,i^{max}}$  – the maximal cutoff radius of the basis functions of atom  $i$ . The same potential is subtracted from the Hartree potential

$$\delta V(r) = V_H(r) - \sum_i V_i^{atom}(r). \quad (2.4.8)$$

Potential  $V_i^{NA}(r)$  is short-range by construction, so it is stored as a function on an  $r$  grid. The last two terms  $\delta V(r)$  and  $V_{xc}(r)$  require total density  $\rho(r)$  for the calculation, which is calculated from the density matrix  $\rho_{\mu\nu}$  as

$$\rho(r) = \sum_{\mu\nu} \rho_{\mu\nu} \phi_\nu^*(r) \phi_{\mu\nu}(r), \quad (2.4.9)$$

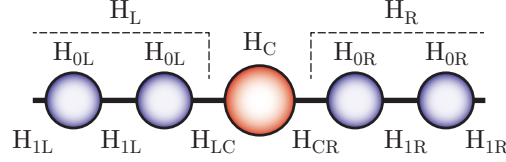


Figure 2.4: Schematic representation of system. Red circle - scattering part, blue circles - electrodes principal layers.

where the indices  $\mu$  and  $\nu$  are the common indexes for basis functions  $\phi_\nu(r)$  and  $\phi_\mu(r)$ . Here the density matrix is calculated as

$$\rho_{\mu\nu} = \sum_k c_{\mu k} n_k c_{\nu k}^*, \quad (2.4.10)$$

where  $n_k$  is the occupation of  $k$ -th eigenstate of the Hamiltonian,  $c_{\mu k}$  and  $c_{\nu k}$  are coefficients of expanded eigenstate  $\psi_k(r)$  in a basis,

$$\psi_k(r) = \sum_\mu \phi_\mu(r) c_{\mu k}. \quad (2.4.11)$$

Usually density matrix is a sparse matrix, since atoms orbitals overlap only with nearest neighbors. This sparsity makes the total density calculation for an  $N$ -atom system an  $O(N)$  process and thus very efficient.

## 2.4.2 Smeagol

The code Smeagol was developed on the basis of SIESTA for the calculation of transport properties using non-equilibrium Keldysh-Green's function formalism. [147, 148] Smeagol uses DFT, LCAO bases and pseudopotentials. NEGF part of the code is based on the scheme described in Sec. 2.3.4.

Let us briefly consider the NEGF implementation in Smeagol. The first step done in the calculation is the division of the system into “principal layers”, which interact only with their respective neighbors (Fig. 2.4). This reduces the number of non-zero matrix elements in both the Hamiltonian and the Green's functions. Electrodes are assumed to have a periodic structure, which allows to calculate their Green's functions recursively.

The total system then consists of three principal parts: the two electrodes and the contact scattering region. The Hamiltonian matrix may then be written in a schematic way as:

$$\hat{H}_{tot} = \begin{pmatrix} H_L & H_{LC} & 0 \\ H_{CL} & H_C & H_{CR} \\ 0 & H_{RC} & H_R \end{pmatrix} = \begin{pmatrix} \cdot & \cdot & \cdot & \cdot & \cdot & \cdot & \cdot \\ \cdot & H_{0L} & H_{1L} & 0 & 0 & 0 & \cdot \\ \cdot & H_{1L}^\dagger & H_{0L} & H_{LC} & 0 & 0 & \cdot \\ \cdot & 0 & H_{CL} & H_C & H_{CR} & 0 & \cdot \\ \cdot & 0 & 0 & H_{RC} & H_{0R} & H_{1R} & \cdot \\ \cdot & 0 & 0 & 0 & H_{1R}^\dagger & H_{0R} & \cdot \\ \cdot & \cdot & \cdot & \cdot & \cdot & \cdot & \cdot \end{pmatrix} \quad (2.4.12)$$

Here  $H_{0L}$ ,  $H_{0R}$  are the Hamiltonians of left and right electrodes' principal layers,  $H_C$  – the central contact Hamiltonian,  $H_{1L}$ ,  $H_{1R}$  – interactions between the principal layers of the



electrodes,  $H_{LC}$ ,  $H_{RC}$  – interactions between the contact and the closest electrodes' principal layer and  $H_L$ ,  $H_R$  – the full Hamiltonians of the electrodes. The retarded Green's function  $\hat{G}^R(E)$  of the full system can be written as

$$[(E + i\delta)\hat{S} - \hat{H}_{tot}]\hat{G}^R(E) = \hat{I}, \quad (2.4.13)$$

where  $I$  is the identity matrix,  $\delta \rightarrow 0^+$ ,  $\hat{S}$  is the overlapping matrix,  $E$  is the energy. In a more detailed matrix form, separating the scattering part and the electrodes:

$$\begin{pmatrix} (E + i\delta)\hat{S}_L - \hat{H}_L & (E + i\delta)\hat{S}_{LC} - \hat{H}_{LC} & 0 \\ (E - i\delta)\hat{S}_{CL} - \hat{H}_{CL} & (E + i\delta)\hat{S}_C - \hat{H}_C & (E + i\delta)\hat{S}_{CR} - \hat{H}_{CR} \\ 0 & (E - i\delta)\hat{S}_{RC} - \hat{H}_{RC} & (E + i\delta)\hat{S}_R - \hat{H}_R \end{pmatrix} \begin{pmatrix} \hat{G}_L & \hat{G}_{LC} & \hat{G}_{LR} \\ \hat{G}_{CL} & \hat{G}_C & \hat{G}_{CR} \\ \hat{G}_{RL} & \hat{G}_{RC} & \hat{G}_R \end{pmatrix} = \begin{pmatrix} \hat{I} & 0 & 0 \\ 0 & \hat{I} & 0 \\ 0 & 0 & \hat{I} \end{pmatrix}, \quad (2.4.14)$$

where  $\hat{G}_L$ ,  $\hat{G}_R$  and  $\hat{G}_C$  are the Greens functions of left and right electrodes and the contact respectively.  $\hat{G}_{LC}, \dots$  are the corresponding mixed Green's functions. We are interested in obtaining the Green's function of the central contact  $\hat{G}_C$ . As it was already shown in Sec. 2.3.4, due to the absence of a direct interaction between the electrodes, Green's function of the contact can be simply expressed through the self-energies as

$$\hat{G}_C^R(E) = [(E + i\delta)\hat{S}_C - \hat{H}_C - \hat{\Sigma}_L^R(E) - \hat{\Sigma}_R^R(E)]^{-1} \quad (2.4.15)$$

Here  $\hat{\Sigma}_L^R(E)$  and  $\hat{\Sigma}_R^R(E)$  are the retarded self energies of left and right electrodes:

$$\begin{aligned} \hat{\Sigma}_L^R(E) &= ((E + i\delta)\hat{S}_{CL} - \hat{H}_{CL})\hat{G}_L^R((E + i\delta)\hat{S}_{LC} - \hat{H}_{LC}), \\ \hat{\Sigma}_R^R(E) &= ((E + i\delta)\hat{S}_{CR} - \hat{H}_{CR})\hat{G}_R^R((E + i\delta)\hat{S}_{RC} - \hat{H}_{RC}), \end{aligned} \quad (2.4.16)$$

where  $\hat{G}_L^R$ ,  $\hat{G}_R^R$  are the Green's functions of left and right electrodes respectively. The Green's functions of the electrodes are calculated separately and stored to be reused in other calculations with the same electrodes but different central contacts. Self-energies however have to be recalculated in each separate case since they depend on the interaction between the contact and the electrodes. Once the self-energies of the system have been calculated, the transmission probability can be determined from Eq. (2.3.34).

Since Smeagol is a DFT-based method, physical quantities depending on electron density should be determined self-consistently in a loop. In SIESTA the density is calculated from the density matrix, which is derived from the wave-functions. In Smeagol the density matrix of the contact is calculated from the lesser Green's function of the contact as

$$\hat{\rho}_C = -\frac{i}{2\pi} \int dE \hat{G}_C^<(E), \quad (2.4.17)$$

and substituted into the SIESTA part for further calculations in the loop. In the equilibrium case lesser Green's function can be expressed through retarded Green's function according to Eq (2.3.25) as (note that  $\hat{G}_C^R(E) = \hat{G}_C^{A\dagger}(E)$ ):

$$\hat{G}_C^<(E) = -2i\mathcal{I}\mathfrak{m}[\hat{G}_C^R(E)]. \quad (2.4.18)$$

Due to analytic properties of the retarded Green's function, its integration can be performed along the contour in the upper complex plane, which should include all occupied states of the system, corresponding to the poles of  $\hat{G}_C^R(E)$ .

If the bias voltage  $V$  is non-zero, Hamiltonian of the system can be written as follows:

$$\hat{H} = \begin{pmatrix} \hat{H}_L + \hat{S}_L eV/2 & \hat{H}_{LC} & 0 \\ \hat{H}_{CL} & \hat{H}_C & \hat{H}_{CR} \\ 0 & \hat{H}_{RC} & \hat{H}_R - \hat{S}_R eV/2 \end{pmatrix}. \quad (2.4.19)$$

In Smeagol a bias voltage  $V$  applied between the leads is considered to result in a shift of the electronic structure of the electrodes by  $\pm V/2$ . Interaction Hamiltonians  $\hat{H}_{LC}$ ,  $\hat{H}_{RC}$ , ..., however, remain the same. This approximation allows to calculate self-energies only for zero-bias and then reuse them for different biases:

$$\hat{\Sigma}_{L,R}(E, V) = \hat{\Sigma}_{L,R}(E \mp eV/2, 0). \quad (2.4.20)$$

The density matrix of the biased system is no more an equilibrium one. Therefore, one needs to integrate the non-equilibrium Green's function in its general form (see, for example, Eq. (2.3.31)). To simplify integration in Eq. (2.4.17) one can split the integral in two parts. Writing the expression (2.3.31) as

$$\hat{G}_C^< = i[\hat{G}_C^R(\hat{\Gamma}_L + \hat{\Gamma}_R)\hat{G}_C^{R\dagger}f(E - \mu_L) + \hat{G}_C^R\hat{\Gamma}_R\hat{G}_C^{R\dagger}(f(E - \mu_R) - f(E - \mu_L))], \quad (2.4.21)$$

where the term  $\hat{G}_C^R\hat{\Gamma}_R\hat{G}_C^{R\dagger}(f(E - \mu_L) - f(E - \mu_R))$  is subtracted and added to the equation (we omit the dependence on  $E$  for simplicity). Taking into account, that  $\hat{\Gamma}_L + \hat{\Gamma}_R = i[(\hat{G}_C^R)^\dagger]^{-1} - (\hat{G}_C^R)^{-1}$  the expression (2.4.22) can be rewritten as

$$\hat{G}_C^< = -2i\mathfrak{Im}[\hat{G}_C^R]f(E - \mu_L) + i\hat{G}_C^R\hat{\Gamma}_R\hat{G}_C^{R\dagger}(f(E - \mu_R) - f(E - \mu_L)). \quad (2.4.22)$$

We see, that the first term is just an equilibrium lesser Green's function with chemical potential  $\mu_L$  (see Eq. (2.4.18)). Now we can write the expression for non-equilibrium density matrix as a sum of the equilibrium part  $\hat{\rho}_C^{eq}$  and a non-equilibrium correction  $\hat{\rho}_C^{ne}$ :

$$\hat{\rho}_C = \hat{\rho}_C^{eq} + \hat{\rho}_C^{ne}, \quad (2.4.23)$$

where

$$\hat{\rho}_C^{eq} = -\frac{1}{\pi} \int dE \mathfrak{Im}[\hat{G}_C^R(E)]f(E - \mu_L), \quad (2.4.24)$$

$$\hat{\rho}_C^{ne} = \frac{1}{2\pi} \int dE \hat{G}_C^R(E)\hat{\Gamma}_R(E)\hat{G}_C^{R\dagger}(E)(f(E - \mu_R) - f(E - \mu_L)). \quad (2.4.25)$$

Integration in  $\hat{\rho}_C^{ne}$  can be performed in narrow range of energies along the real axis, which for example at zero temperature equals  $V = \mu_L - \mu_R$ . If we assume, that in equilibrium the system had a Fermi energy of  $E_F$ , then after applying a bias according to Eq. (2.4.19)  $\mu_L = E_F + V/2$  and  $\mu_R = E_F - V/2$ . Therefore, for calculation non-equilibrium correction  $\hat{\rho}_C^{ne}$  integration can be performed from  $E_F - V/2$  to  $E_F + V/2$ . Calculation of  $\hat{\rho}_C^{eq}$  is performed in the same way as in Eq. (2.4.17).

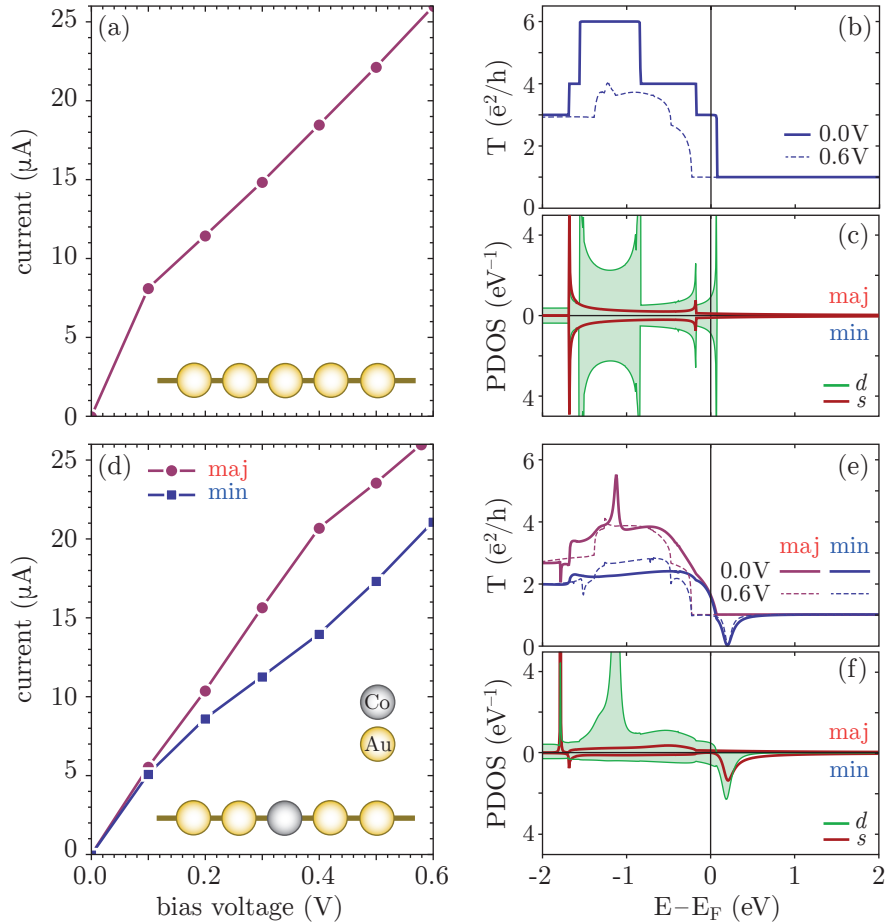


Figure 2.5: Results of transport calculations of (a-c) pure Au and (d-f) mixed Au-Co chains. (a,d)  $I(V)$  characteristic, (c,e) transmission probabilities for bias voltages 0.0 and 0.6 V, PDOS of (c) Au and (f) Co atoms in pure Au and Au-Co chains, respectively.

## 2.5 Typical calculation workflow

To illustrate how the formalism described above works in practice let us consider a simple system and see what is necessary to calculate its electronic and magnetic properties and the electron conduction through it. A traditional prototypical system used for benchmarking transport calculations are gold atomic chains and nano-contacts, for they allow a good comparison to analytical calculations and basic physical considerations [148, 149].

As a first example we choose a pure infinite monatomic linear gold chain with an equilibrium interatomic distance of 2.4 Å. In Fig. 2.5(a-c) transport and electronic structure calculations are presented. The chain has a non-magnetic electronic configuration which leads to non-spin-polarized quantum conductance of the chain. Let us consider the zero-bias transmission plotted with solid lines in Fig. 2.5(b). As was mentioned in Sec. 2.3.1, according to Landauer-Büttiker approach, each electron band can form a transport channel with conductance  $G_0/2$  per spin. This statement is excellently illustrated in Figs. 2.5(b) and 2.5(c) where the energy-resolved transmission shows a perfect match with  $s$  and  $d$  projected densities of states. The band edges in 2.5(c) defined by Van Hove singularities exactly correspond to the step-like onsets in transmission. Within the energy range of each band transmission has a ballistic character and thus exhibits constant behavior.

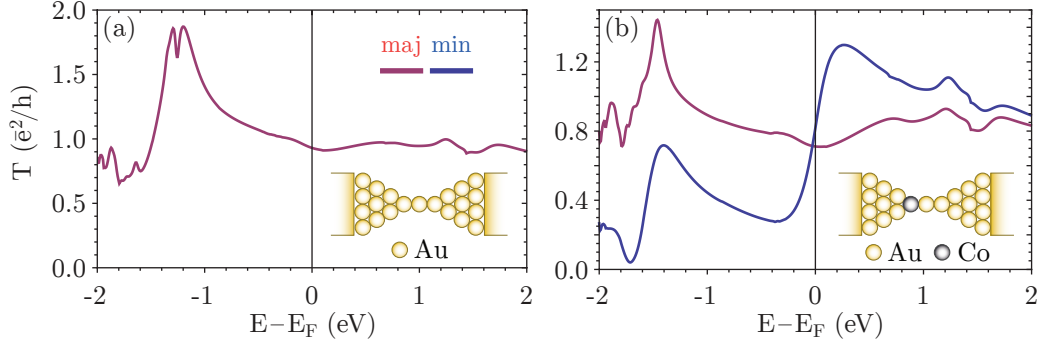


Figure 2.6: Transmission probabilities of (a) pure Au and (b) Au-Co nano-contacts. Calculation geometries are sketched in the insets of corresponding sub-figures.

However, if we apply a bias voltage  $U$  to a stretch of the chain comprising 5 gold atoms, the narrow  $d$  band of the left and right parts shall shift with respect to each other by  $e \cdot U$  eV disturbing the ballistic nature of the transmission. The resulting transmission curve is shown in Fig. 2.5(b) with a dashed line. Due to the smearing of transmission band edges the transmission peaks loose their exact  $G_0/2$  quantization. This band behavior affects the  $I(V)$  characteristic, causing a change of the  $I(V)$  curve slope at  $U = 0.1$  V.

Since the main subject of the present thesis is spin-polarized transport, it is only reasonable to include a magnetic component in our test system. To do so, let us replace one of the gold atoms of the chain discussed above with a single Co impurity (Fig. 2.5(d-f)). In this case translation symmetry is broken, so the nature of the zero-bias conductance differs from the pure ballistic one. The energy-resolved transmission probability (Fig. 2.5(e)) becomes spin-dependent and not strictly quantized in units of  $G_0/2$ . The differences in transmission are caused by the spin-split  $d$  states of Co (Fig. 2.5(f)). The anti-resonance character of transmission in the minority channel [150] at 0.25 eV is caused by scattering of electrons at localized minority  $s - d$  hybridized states of Co. We can also observe large resonance and small anti-resonance features in the majority channel at energies of  $-1.2$  and  $-1.75$  eV respectively, which are also a consequence of electron scattering by Co  $d$  states. If we consider the  $I(V)$  characteristic, we can see that with increasing bias voltage the spin splitting of the current increases which is caused by the influence of the anti-resonance in the minority channel.

To see whether our theoretical and numerical formalisms perform equally well with more realistic systems we present here the calculations of a gold nano-contact consisting of a 3-atomic gold chain suspended between pyramidal gold electrodes (see inset in Fig. 2.6(a)), a geometry mimicking the gold break-junctions used obtained in experiments [5]. The transmission of such a junction (shown in Fig. 2.6(a)) has a uniform structure around the Fermi-level with a magnitude of roughly  $G_0/2$ , which is an evidence of the ballistic nature of conductance therein, caused by the strong coupling between the  $s$  shells of Au atoms in the chain forming a conduction channel. The peak at  $-1.2$  eV is caused by resonant tunneling through the  $d$  states which are located lower than in the infinite chain due to the interaction of chain atoms with the electrodes.

Replacing one of the chain atoms with a Co (Fig. 2.6(b)) significantly changes the transmission characteristics. As was the case for an infinite chain, we can observe in the minority channel peaks and depletion regions which have resonance and anti-resonance natures. Both majority and minority channels have a peak at  $-1.2$  eV caused by resonant tunneling through

the  $d$  states of Au atoms and Co majority  $d$  states, located approximately at the same energy. Significant quantitative differences with respect to an infinite chain are also caused by the strong interaction with electrodes.

We can thus see that theoretical and numerical methods used in the present work give reasonable results agreeing well with basic physical consideration for simple model systems and are also able to capture the complex intricacies of the electronic and transport properties of larger and more realistic setups, allowing one to analyze their transport and electronic properties.



# Chapter 3

## Spin-injection in mixed Au-Co chains between Co electrodes

Having established the historical motivation and the theoretical framework let us move on to the main subject of the present thesis – spin dependent transport in atomic-scale contacts.

The first original chapter of the present thesis shall be devoted to the emergence of high spin polarization of conductance in Co-Au nano-contacts. As was already briefly mentioned in the introduction the interest in this particular system is motivated by the recent works of Bernard-Mantel and coworkers [4] who have studied electron transport through a paramagnetic gold cluster sandwiched between cobalt electrodes and have found it to exhibit nonzero magnetoresistance, which was ascribed to the presence of spin injection from magnetic cobalt electrodes into the paramagnetic gold cluster and the subsequent spin transfer to the other electrode. With its band structure dominated by *s*-electrons at the Fermi level and the *d* bands lying deeper down the energy scale, gold has a relatively low rate of inelastic electron scattering, and especially with electron-electron and electron-phonon interaction frozen out and low impurity density the spin-relaxation times are relatively long. [151] Thus, with gold having a mean spin diffusion length of about 100 nm, [61] it is not surprising that two ferromagnetic Co electrodes and an Au nano-particle should exhibit magnetoresistive behavior, especially in the tunneling geometry, which is the case in the latter experiment. However, followup experiments by Egle and coworkers [5] have shown that magnetoresistance ratios of a Co-Au-Co break junctions are excessively high (up to 100% in contact regime and 14000% in tunneling geometry). This suggests that apart from efficient spin diffusion in Au, the spin injection from cobalt into gold should be extremely efficient in that particular system.

A set of very similar systems (Cu, Al and Si chains between Co electrodes) has been investigated theoretically in the past [152]. In that study, however, no system was found to exhibit a magnetoresistance ratio exceeding 50%, which might be partially due to unrealistic unrelaxed geometries used due to the limitations of the employed method.

This discrepancy of experiment and existing theory was a further motivation for choosing Au-Co nano contacts as one of the subjects of this thesis. As shall be shown presently, the uniqueness of the above-mentioned system (gold chain connecting cobalt electrodes) lies in the efficient hybridization-driven spin injection into the gold contact from cobalt electrodes. A theoretical explanation of such behavior shall be given in the present chapter relating it to the strong interaction between cobalt and gold *s* – *d* states in the junction region. Furthermore, the evolution of conductance with the stretching of the contact shall be traced.

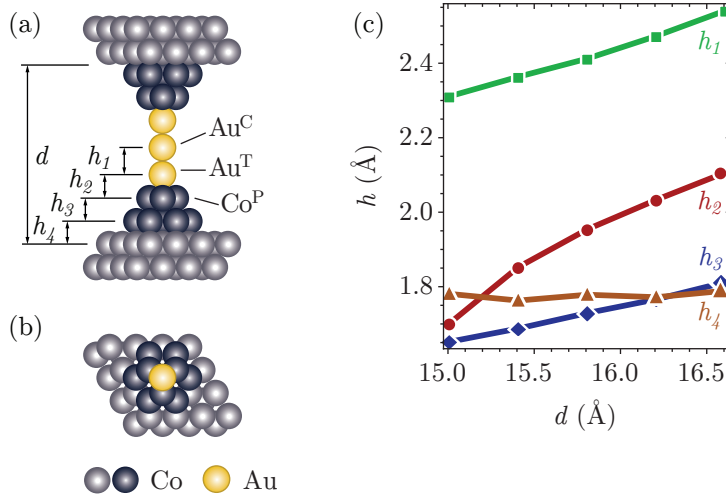


Figure 3.1: (a) Geometry of the nano-contact: a pure 3-atomic Au wire between Co electrodes, side view. (b) Unit cell geometry of the electrode - top view. (c) Dependence of relaxed interlayer/interatomic distances ( $h_1, h_2, \dots$ ) in the contact on the distance between electrodes  $d$ .

## 3.1 Calculation details

Transport calculations for this system were performed within the framework of the formalisms described in Chapter. 2 and according to the workflow in Sec. 2.5.

As an exchange-correlation functional we used the Perdew-Zunger's scheme of local density approximation LDA, [124] which is known to be a good choice for the description of structural and electronic properties of  $5d$  systems. For temperature smearing the Methfessel-Paxton method with 600K was chosen. As the LCAO basis set we chose a double- $\zeta$  basis including  $s$  and  $d$  shells for both Co and Au with additional polarized orbital for  $s$  shells. Scalar-relativistic pseudo-potentials with  $3d$ ,  $4s$  and  $5d$ ,  $6s$  valence orbitals were chosen for cobalt and gold respectively. For transport calculations, upon checking the convergence, a  $5 \times 5$   $k$ -point grid in the plane perpendicular to the transport direction ( $z$ -axis) was chosen. Relaxation of electrodes was performed with SIESTA code with  $4 \times 4 \times 1$  and  $4 \times 4 \times 3$   $k$ -points meshes for electrode and contact relaxations respectively.

## 3.2 Pure gold chain between cobalt electrodes

We shall start the discussion with the simplest case of the system – a pure 3-atomic gold chain suspended between pyramid-shaped cobalt electrodes.

### 3.2.1 Geometry of the system

The geometry used in calculations is shown in Fig. 3.1(a). The nano contact was modeled by a 3-atom gold chain suspended between *hcp* Co(001) tips. The tips were represented by Co pyramids containing 10 atoms in two *hcp* layers. The pyramids themselves were adsorbed on *hcp* Co(001) slabs. [153, 154] To accommodate electronic relaxations at the surface and mitigate the effect of the super-cell interaction the slabs were taken to be 8 layers thick and  $4 \times 4$  atoms in cross-section perpendicular to the transport direction, which is sufficient to



decouple the super-cell images of nanocontacts from each other. With respect to the axis of the nano-contact (passing through the gold atoms) the system had a  $C_{3v}$  symmetry. In the following we shall denote outer (tip) and central atoms of the gold chain as  $\text{Au}^{\text{T}}$  and  $\text{Au}^{\text{C}}$  respectively. The underlying pyramid cobalt atoms shall be denoted as  $\text{Co}^{\text{P}}$ . The distance between electrodes defining the stretching of the chain shall be referred to as  $d$ . In the following, we shall denote the systems by the distance between electrodes. In all calculations the geometries of the electrodes and the gold chain were relaxed until the residual forces were no larger than  $0.01 \text{ eV/\AA}$ .

To investigate the dependence of transport characteristics on the stretching of the contact, calculations were performed for different fixed distances  $d$  between the electrodes (see Fig. 3.1(a)), ranging from  $15.00 \text{ \AA}$  to  $16.6 \text{ \AA}$ . The geometry of the chain was kept linear during stretching. The dependence of relaxed interatomic distances in the contact on the distance between electrodes has a quite linear character (Fig. 3.1(c)). The “softer” bonds between Au atoms, as well as the  $\text{Au}^{\text{T}} - \text{Co}^{\text{P}}$  bond closely follow the changes of  $d$ . The interlayer bonds in the pyramid are already much stiffer and the lower layer of the pyramid is almost unaffected by contact’s length change. This shows that the nature of interatomic bonds is not altered in the process of stretching and the orbital overlap can be expected to change likewise, *i.e.* smoothly. The restriction of the linearity of the chain is assumed solely for the sake of a clearer qualitative picture of the nano-contact’s physics. It shall be shown that fully unconstrained relaxation of the contact (allowing the chain to buckle and assume a zig-zag configuration) does not significantly change the results and conclusions obtained.

### 3.2.2 Magnetic moments of the junction

Supporting the assumption of a smooth change in electronic properties of the chain with stretching, magnetic moments in the system are found to only weakly depend on the stretching of the contact. The bottom layer of the Co pyramids has a spin moment of  $2.0 \mu_{\text{B}}$  (for reference, *hcp* Co bulk value is  $1.71 \mu_{\text{B}}$ ) which shows no dependence on  $d$ . The moments of  $\text{Co}^{\text{P}}$  atoms increase from  $2.11 \mu_{\text{B}}$  to  $2.19 \mu_{\text{B}}$  as the contact is stretched from  $15.0$  to  $16.6 \text{ \AA}$ , reflecting the bond stretching and reduction of coordination. At the same time, the induced moment of  $\text{Au}^{\text{T}}$  atoms reduces from  $0.11 \mu_{\text{B}}$  to  $0.05 \mu_{\text{B}}$ . Central gold atom  $\text{Au}^{\text{C}}$  is practically unpolarized at all stretching distances  $d$ .

### 3.2.3 Spin-polarized conductance

It is known, that Co bulk with an *hcp* structure has a ferromagnetic ordering of spins, [153, 154] so in our calculations atomic spins within each electrode are ferromagnetically aligned. To study the electronic properties of the junction and the conductance thereof we have performed transport calculations for the case of parallel spins alignment of both electrodes.

Calculated energy-resolved zero-bias transmission of the system described above (for a sketch see Fig. 3.1(a)) is shown in Fig. 3.2(a) for different inter-electrode distances  $d$ . It can be seen, that stretching of the contact has a pronounced influence on the energy position of the minority transmission peak, while majority conductance remains flat and almost unchanged. If we calculate the conductance polarization at the Fermi level as

$$P = \frac{T^{\uparrow}(E_F) - T^{\downarrow}(E_F)}{T^{\uparrow}(E_F) + T^{\downarrow}(E_F)}, \quad (3.2.1)$$

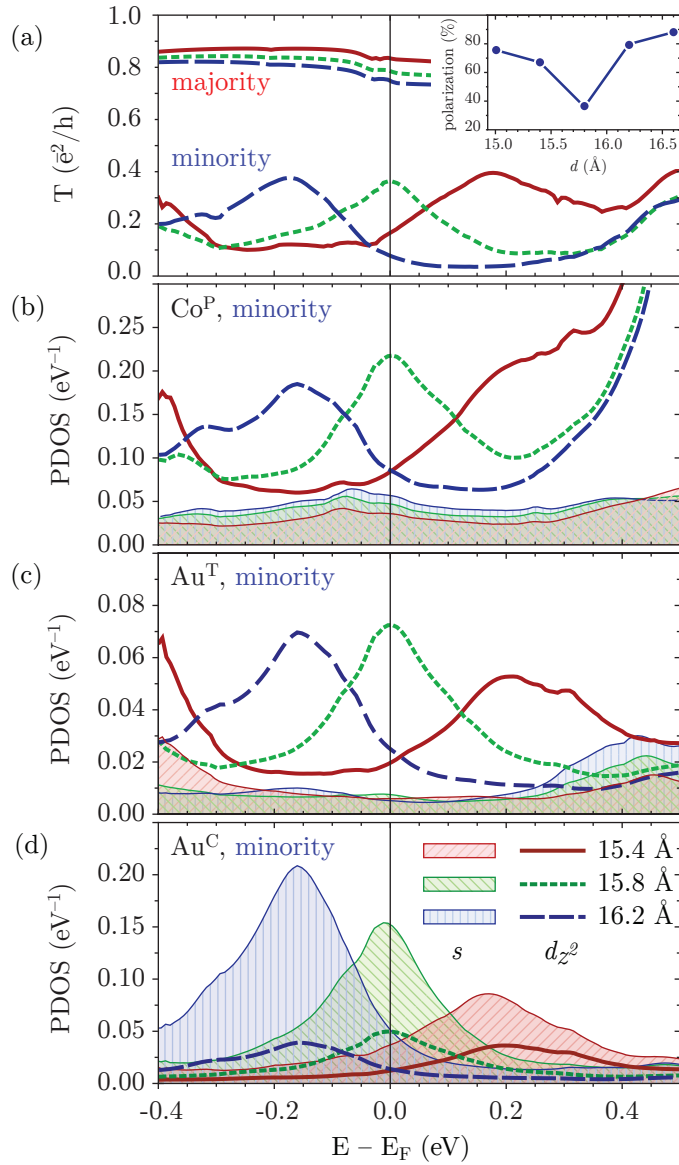


Figure 3.2: (a) Transmission probability of the nano-contact for different inter-electrode distances. The inset shows the spin polarization of conductance at the Fermi level. (b,c,d) Minority  $s$  and  $d$  projected densities of states for Co, tip Au and central Au atoms for different distances between electrodes. Filled areas –  $s$ -states, thick curves –  $d_{z^2}$ -states.  $s$ -states curves for different distances are color- and hatching-coded (see the legend for details).

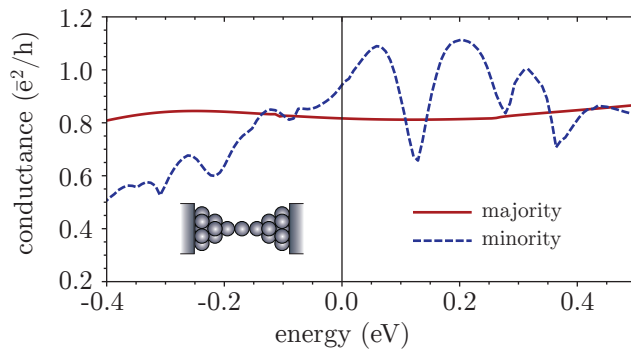


Figure 3.3: Transmission probability of the pure linear Co nano-contact.

where  $T^\uparrow$  and  $T^\downarrow$  are the Fermi level transmission coefficients of majority and minority spin channels respectively, we shall find (inset of Fig. 3.2(a)) that it is rather high, reaching 80% and furthermore changes significantly as the contact is stretched. Large spin polarization of conductance is caused by the low amplitude of minority spin channel transmission around the Fermi level (see Fig. 3.2(a)) and therefore is a consequence of strong scattering of minority electrons. This result is quite interesting, since the DOS of Co is dominated by the half-filled minority  $d$ -band at the Fermi level and one could expect minority  $d$ -electrons to strongly contribute to Fermi level transmission through direct orbital overlap, as it is observed in pure Co infinite chain. [51, 155] It turns out, that the conduction of a Au chain between Co electrodes, conduction of a pure Co nano-contact and the conduction of Co chain between planar electrodes are distinctly different and governed by different physical aspects of the electronic structure and bonding. Authors in the Ref. [152] present the conductance of a pure linear Co chain attached to planar Co electrodes which exhibits practically no polarization. Our calculation of such a pure Co nano contact with a more realistic pyramid-like lead geometry is presented in Fig. 3.3. Here the geometry is very similar to the case for the Co/Au/Co nano-contact in Fig. 3.1 with an inter-electrode distance  $d = 15.0\text{\AA}$ . We see, that the junction has weak opposite polarization to the one found in Co/Au/Co system. This is a clear indication that geometry, rather than just chemistry plays a determining role in the shaping of the spin-polarization of conductance. How exactly that works shall be shown in the next sections.

Another effect which should be noted from the outset is the strong change of the spin-polarization of conductance in a Co/Au/Co nanocontact with increasing inter-lead distance  $d$  (inset in Fig. 3.2(a)). It falls from almost 80% to 30% as the inter-electrode distance is increased from 15.4 to 15.8  $\text{\AA}$  and is subsequently restored to almost 90% as the stretching continues towards 16.2  $\text{\AA}$ . From the energy resolved transmission curves (Fig. 3.2(a)) it can be deduced that this jump in polarization is caused by a pronounced peak in the transmission crossing the Fermi level in the minority channel as the contact is stretched. At the same time, majority transmission is comparable with  $G_0$  and only slightly changes during stretching. Such closeness of the transmission coefficient to  $G_0$  can be ascribed to the presence of ballistic transport in the majority channel.

### 3.2.4 Projected density of states analysis

To understand this behavior of the transport properties, let us consider the projected density of states (PDOS) of the contact's gold atoms ( $\text{Au}^{\text{C}}$  and  $\text{Au}^{\text{T}}$ ) and the neighboring cobalt atoms of the electrodes  $\text{Co}^{\text{P}}$  (Fig. 3.2(b-d)). Majority states of the contact atoms, similarly to the majority transmission, are flat and featureless around the Fermi energy (shown in Fig. 3.4(a)). They are mostly of  $s$ -character and are not affected by the stretching of the contact. Their extended wave functions can provide transport almost without scattering due to the strong overlap (and robust band formation). Thus, to explain the conductance polarization we shall concentrate on minority PDOS.

Comparing transmission and PDOS in Fig. 3.2 one immediately notices that the minority transmission peak can be correlated with the peaks in  $d_{z^2}$ -states of  $\text{Co}^{\text{P}}$  and  $\text{Au}^{\text{T}}$  atoms as well as with  $s$ -states of the  $\text{Au}^{\text{C}}$  atom. Other symmetries also show traces of hybridization, but to a significantly smaller degree and thus we do not show them here, so as not to overload the figures. Note, that the amplitude of the  $d_{z^2}$ -states peak at the  $\text{Co}^{\text{P}}$  atom is several times larger, than that of the same state at  $\text{Au}^{\text{T}}$  and  $\text{Au}^{\text{C}}$  atoms. The amplitude of the peak in

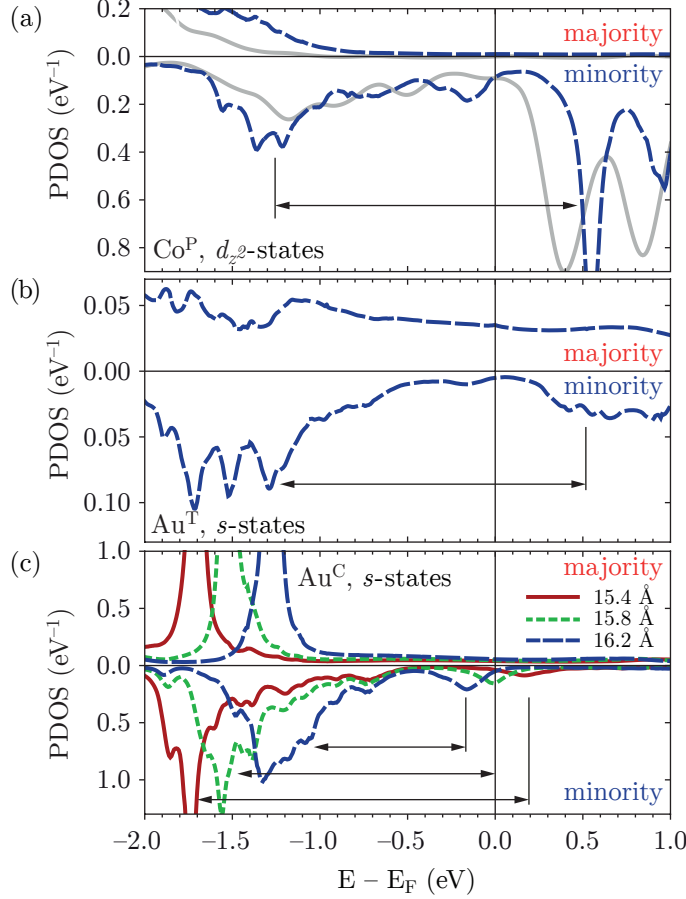


Figure 3.4: (a) Projected density of  $d_{z^2}$ -states of Co atoms in contact with the Au wire (dashed line) and  $d_{z^2}$ -state of the same atoms in absence of the Au chain (solid line). (b)  $s$  states of tip Au atom and (c)  $s$  states of central Au atom for different distances between electrodes. Positions of peaks around the fermi level are highlighted by vertical black lines. The splitting of the band/levels is shown by horizontal arrows.

$s$ -states of the  $\text{Au}^{\text{C}}$  atom, on the contrary, has the same order as the  $d_{z^2}$ -states peak of  $\text{Co}^{\text{P}}$ . Appearance of the peaks in all contact atoms can be related to a hybridization of the  $\text{Au}^{\text{C}}$  atom's  $s$ -states and the  $d_{z^2}$ -states of  $\text{Au}^{\text{T}}$  and  $\text{Co}^{\text{P}}$  atoms. Large difference in amplitudes of the peaks in PDOS on  $\text{Co}^{\text{P}}$  and  $\text{Au}^{\text{T}}$  atoms can be ascribed to two facts. Firstly, gold atoms have practically no  $d$ -states at the Fermi energy. Hybridization of  $\text{Au}^{\text{C}}$  and  $\text{Au}^{\text{T}}$  atoms is weak and therefore we observe the small amplitude of  $d_{z^2}$  peaks in  $\text{Au}^{\text{T}}$  atoms. And secondly,  $\text{Au}^{\text{C}}$  atom's  $s$ -states have long “tails” and can hybridize with cobalt  $d$  minority states directly.

To understand the origin of the peaks that we observe in Fig. 3.2 we shall take a look at the PDOS on a larger energy scale (Fig. 3.4(c)). Analyzing the stretching-induced dynamics of the position of the peaks around  $-1.5$  eV and at the Fermi level we see that the former shift to higher energies as the inter-electrode distance is increased, while the latter shift downward. This behavior is consistent with the picture, where both sets of peaks belong to the same state split by the interatomic interaction (horizontal arrows). Thus, as the contact is stretched, the interatomic distance increases, reducing the orbital overlap and the states gradually coalesce into single atomic-like levels. So, the origin of these peaks that we

observe in Fig. 3.2 can be the splitting of the  $sd_{z^2}$  hybridized state of the  $\text{Au}^{\text{C}}$  atom due to the interaction of the latter with its neighbors.

Though the physics described above gives a feasible explanation to the movement of the peak, it has to be mentioned, that other possible explanations to the origin and movement of the peak close to the Fermi level could exist. For example, the  $s$ -states of the gold chain could be subject to confinement between the two cobalt electrodes. As was shown in recent works, [49, 50, 156] standing waves could exist in a chain nano-contact between electrodes and have a quantized spectrum. Therefore, conductance may exhibit peaks at energies, corresponding to the energies of these confined states. However, the motion of the lower peak in Fig. 3.4(c) to higher energies (around  $-1.5$  eV) would still have to be explained by the decrease of interaction between the central and the neighboring atoms.

A careful look at Figs. 3.4(a) and 3.4(b) will reveal that the minority states of the  $\text{Au}^{\text{T}}$  atom are dominated by the interaction with  $\text{Co}^{\text{P}}$   $d_{z^2}$  states (dashed line). Comparing this density of states (Fig. 3.4(a), dashed line) with the  $d_{z^2}$ -states of the same atom in absence of a chain (Fig. 3.4(a), solid line), we can see, that the structure of the DOS is similar. The only minor difference is in the position of the peaks above the Fermi level. For the single electrode these peaks are located closer to the Fermi level, than in the contact system. Primarily, the difference in positions of the peaks is explained by hybridization between cobalt and gold states. As the contact is stretched, the distances between the  $\text{Au}^{\text{T}}$  atom and underlying cobalt atoms change from  $2.3$  Å to  $2.5$  Å, which corresponds to the presence of a tight chemical  $s-d$  bond. Removing the gold tip atom obviously breaks that bond, leading to a shift of the  $d$ -states of cobalt to lower energies.

In a recent theoretical work [157] it was shown, that pure Co atomic-sized contacts show small spin-polarization of conductance at the Fermi level in contact regime. Nevertheless, in tunnel regime the spin-polarization reaches 100%. This effect comes from different decay lengths of majority (mostly of  $s$ -character) and minority ( $d$ -character) states of the contact. In the present case minority  $d$ -states of Co play a key role in shaping the conductance through the nano-contact. From Fig. 3.4(a) it can also be noted that  $d_{z^2}$ -states of cobalt are partially-filled and split into bonding and anti-bonding states. The hollow between them falls on the Fermi level, leaving it mostly depleted. The interaction between  $\text{Au}^{\text{T}}$  and  $\text{Co}^{\text{P}}$  atoms mostly manifests itself in the mixing of  $s$  and  $d_{z^2}$  states of these atoms. The  $s$  states of the  $\text{Au}^{\text{T}}$  atom are localized by the  $s-d$  hybridization, which “draws” them away from the Fermi energy, leaving the latter devoid of minority  $s$  electrons (Fig. 3.4(b)).

Putting together the puzzle we can conclude that the Fermi level transmission of the contact is mostly determined by the  $s$  band in the majority channel. The  $d$  minority states are strongly localized and thus the conduction in the majority channel is dominant at the Fermi energy, resulting in a high positive polarization. One could say that  $s-d$  interaction at the Au-Co interface acts like as a “blocking” mechanism for conductance in the minority channel. A similar effect has been reported in a theoretical study of Cu chains between planar Co leads. [152] Cu  $s$ -states were shown to be the main channel of conductance at the Fermi level. However, due to the more localized nature of Cu  $s$ -states as compared to gold, and likely due to the absence of a pyramid, in their study the hybridization at the interface was much weaker, and consequently a much weaker magnetoresistance ratio was obtained [15% versus 73% in our case (see Sec. 3.2.5)].

Taking one step back we can summarize that the transport through a gold chain suspended between two Co electrodes is defined by the interaction between the Co and the tip Au atoms. High spin-polarization of the conductance is caused by strongly suppressed mi-

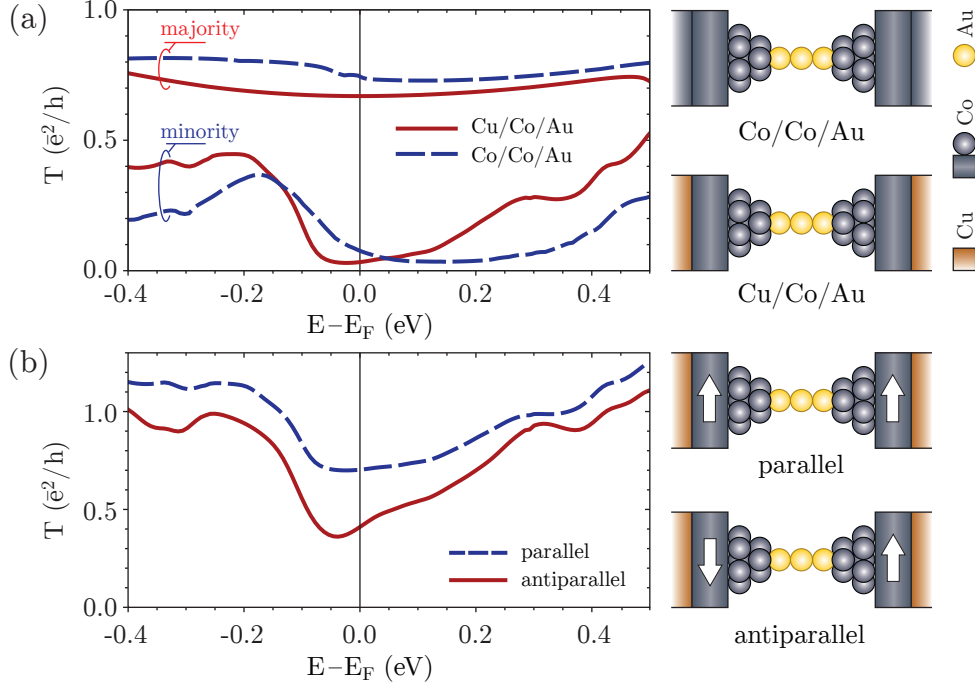


Figure 3.5: (a) Comparison of the spin-polarized conductance of a system with semi infinite Co electrodes (dashed blue line) and our model system for MR calculations – Co slabs supported on Cu (solid red line). (b) Total conductance for parallel and antiparallel spin orientations of cobalt electrodes.

nority and practically unaffected majority  $s$ -states of the tip Au atom. Another significant contribution to conductance is made by the peaks in  $d_{22}$ -states of tip gold and neighboring Co atoms along with the  $s$ -states peak of the central atom. All of them appear due to interatomic orbital hybridization and form additional conductance channels in the contact. With the stretching of the contact, due to the weakening of the bonding between the atoms, the conductance peaks move in energy, altering the current polarization as they pass through the Fermi energy.

### 3.2.5 Magnetoresistance

Having understood the electronic mechanisms determining the nano-contact's conductance we now turn to a quantity which is relevant for actual applications – the magnetoresistance. To estimate magnetoresistance ratio (MRR) we need to calculate conductance through the systems for the cases of parallel and antiparallel mutual alignments of the electrodes' magnetizations (see the sketch in Fig. 3.5(b)). Due to technical intricacies of the method, calculations for systems with differently aligned electrode magnetizations are rather unreliable (in the super-cell part of the calculation a sharp domain wall occurs between one lead and the super-cell image of the other one). Thus to estimate the MRR we replace semi-infinite Co electrodes with a Co slab deposited on a paramagnetic substrate (see sketch in Fig. 3.5(a)). As a nonmagnetic material for the substrate we chose Cu, since the lattice of a Cu(111) surface is close to the  $hcp$ -stacked Co of our magnetic nano-contact. The same localized basis (with added  $p$ -shells) was used for Cu as for Co and the whole system was allowed to relax with the same residual force restrictions as were applied for the Co electrodes (see

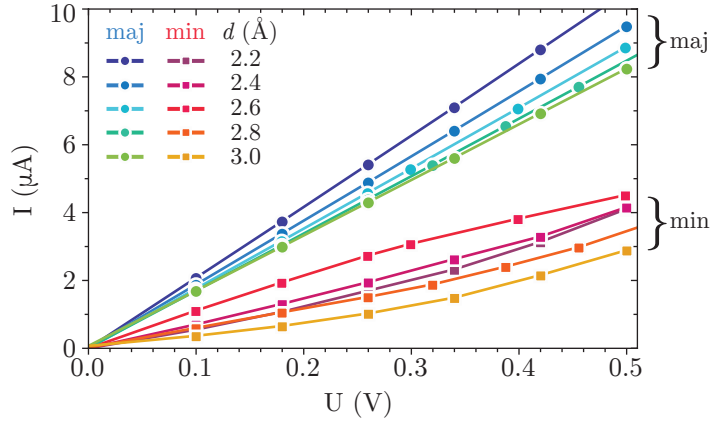


Figure 3.6: Current-voltage characteristics for Co/AAA/Co system for different distance  $d$  between electrodes.

Sec. 3.2.1). The geometry of the contact pyramid and the Au chain were found to be not (or only negligibly) affected by the substitution of a part of Co with Cu.

To see whether Co/Au nano-contacts can be well approximated by the hybrid Cu/Co/Au system, we compare the conductance through both systems with parallel alignment of electrode magnetizations (Fig. 3.5(a)). The energy resolved conductance curves for both systems behave qualitatively the same. They have flat majority parts and strong depletions in the minority channels at the Fermi level. Thus, for all means and purposes, the hybrid Cu/Co/Au system seems to behave very similar to a system with bulk Co electrodes, which not only justifies the use of Cu/Co/Au systems for calculations but could also have important implications for the choice of the system geometry in the experiments. Additionally, the similarity in conductance between Co and Co/Cu leads further supports our statement about the defining role of the Co–Au interface in the formation of spin-polarized conductance.

Turning finally to the MRR, we calculate the energy resolved zero bias transmission for parallel and antiparallel lead-magnetization orientations for the nano-contact with  $d = 15.4$  Å (dashed red and solid blue curves in Fig. 3.5(b), respectively). The Fermi level transmission for the parallel configuration is found to be almost twice as high for the antiparallel one. In antiparallel configuration Co-Au interaction between  $d$  and  $s$ -states at the interface causes a decrease (or “blocking”) of the conductance in both of channels. The MRR can be estimated from spin-resolved transmission coefficients as [53]

$$\text{MRR} = \frac{T_{\uparrow\uparrow}(E_f) - T_{\downarrow\uparrow}(E_f)}{T_{\downarrow\uparrow}(E_f)},$$

where  $T_{\uparrow\uparrow}(E_f)$  and  $T_{\downarrow\uparrow}$  are the zero-bias transmissions at the Fermi level for parallel and antiparallel configurations of electrode magnetization alignments, respectively. In our case we arrive at a value of 73%, which is close to the experimentally observed one [5].

### 3.2.6 I(V) characteristics

While zero bias or *equilibrium* transport is an illustrative quantity to link electronic and magnetic properties of the nano-contact to its conductance, in real experiments a finite bias is usually applied between the leads of a junction. It is thus important to understand how the transport properties change in the *non-equilibrium* case. In Fig. 3.6 current-voltage

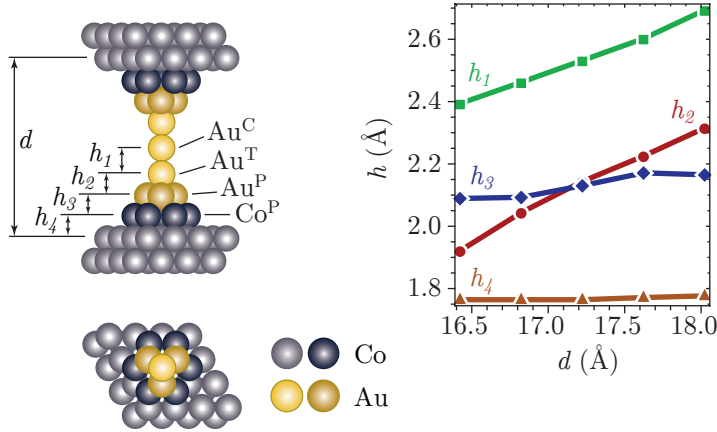


Figure 3.7: (a) Geometry of the system CA/AAA/AC: a pure 3-atomic Au wire between Co-Au electrodes, side view. (b) Unit cell geometry of the electrode - top view. (c) Dependence of relaxed interlayer/interatomic distances ( $h_1, h_2, \dots$ ) in the contact on the distance between electrodes  $d$ .

characteristics of the Co/Au nano-contact are presented for different lead separations  $d$  ranging from 2.2 to 3.0 Å. One can see, that majority electron  $I(V)$  dependence is quite linear, since majority conductance is almost flat around the Fermi level. Minority  $I(V)$  dependence exhibits a slight nonlinearity, which is due to the presence of the localized peak in minority DOS. Otherwise, also the minority  $I(V)$  curve is nearly linear, which allows us to conclude that the conductance and magnetoresistance properties of such a junction described above (see Fig. 3.2(a)) are robust and persist over a wide range of applied biases.

### 3.3 Modified Co-Au junctions

Another simplification which we have introduced in the beginning of the chapter and which we now have to get rid of, is the assumption of the linearity of the chain and the homogeneity of its chemical composition. To make sure, that such spin-filtering behavior as has been discussed above and ascribed to the interaction of Co and Au at the interface of the contact can exist in other geometries and stoichiometries of the contact, we performed calculations allowing an unconstrained relaxation to all the atoms of the contact and varying the chemical composition of the latter.

#### 3.3.1 System with mixed Co-Au electrode

To start introducing variations slowly, the first system addressed was constructed in the same way, as the one we have been discussion up to now, but with mixed Au-Co contact pyramids where the Co<sup>P</sup> layer of atoms was replaced with gold (see sketch in Fig. 3.7). For the rest of the chapter we shall use a short-hand notation for the systems according to their layer-wise chemical composition (“A” standing for Au and “C” – for Co), so that the new system shall be denoted as CA/AAA/AC, while the original one would have been called CC/AAA/CC. Calculations were performed, as above, for different inter-electrode distances  $d$ . The range of  $d$ -s was chosen to keep the junction in contact regime and ranged from 16.5 to 18 Å. The interlayer distances of the equilibrium structure are presented in Fig. 3.7. Note



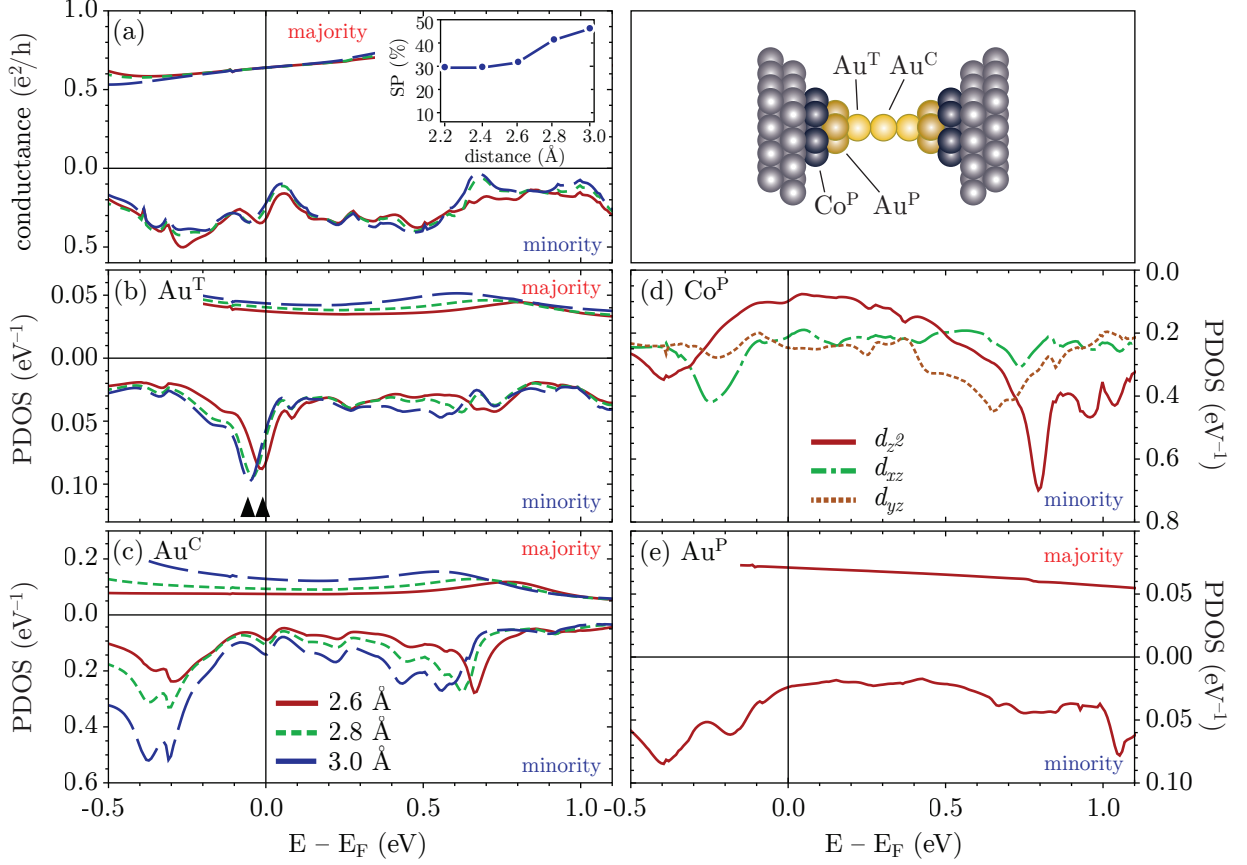


Figure 3.8: (a) Transmission of the system CA/AAA/AC for different inter-electrode distances. The inset shows the spin polarization of conductance at the Fermi level. (c,d)  $s$ -PDOS of  $Au^T$  and  $Au^C$  atoms for different inter-electrode distances. Partial  $d_{z^2}$ ,  $d_{xz}$ ,  $d_{yz}$ -PDOS for the  $Co^P$  (d) and  $s$ -DOS for  $Au^P$  (e) atoms of the contact.

that, in contrast to the previous system, the distance between Co and Au pyramid layers  $h_3$  changes weaker.

Spin-polarization of conductance of the CA/AAA/AC junction (see Fig. 3.8(a)) was found to be less (with values of  $\sim 50\%$ ) than in the case of CC/AAA/CC (90%). However, the physics of the process is exactly the same as in the previous case. Minority  $d$ -states of cobalt atoms neighboring to gold in this system are similar to  $Co^P$   $d$ -states in the system with full cobalt electrodes, discussed in details above (Fig. 3.8(b)). Partially-filled minority Co  $d_{z^2}$ -states hybridize with  $s$ -states of gold atoms, which leads to polarizations of these states at the Fermi level (Fig. 3.8(d)). In contrast to CC/AAA/CC, here the gold atoms have a lower symmetry. So here not only  $dz^2$ , but also  $d_{xz}$ ,  $d_{yz}$ -symmetry states of cobalt significantly contribute to the hybridization with gold and, consequently, to the conductance. So, we can see a rise of transmission around  $-0.2$  eV and corresponding peaks in  $d_{xz}$ ,  $d_{yz}$ -states of  $Co^P$  atom and  $s$ -states of  $Au^P$  atom.

Moreover, one can see, that transmission in the CA/AAA/AC system is much less sensitive to the stretching of the contact than in Co/AAA/Co. One can relate this observation to a change of bonding between Co and Au layers of the pyramids. As already mentioned, conductance in minority channel is determined by Co-Au interaction. Since the distance between Au and Co layers ( $h_3$  for CA/AAA/AC) changes less, than the  $h_2$  distance in

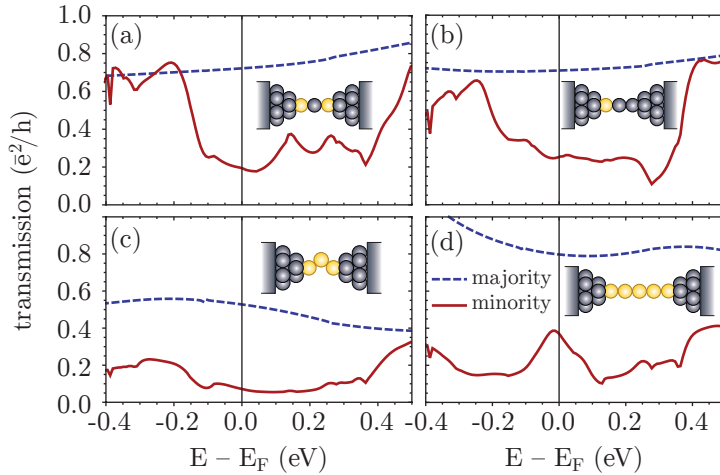


Figure 3.9: Transmission of systems with varying geometry and chemical composition/stoichiometry. Sketches of considered configurations are shown in the top part of the figure (atom colors the same as in Fig. 3.1). Corresponding conductance curves can be found in the graph in the bottom part.

CC/AAA/CC (distance between tip Au and pyramid Co atom), interaction between Co and Au remains almost unaffected by the stretching, which explains the robust behavior of the transmission.

### 3.3.2 Other modifications of Au-Co junction

Other modifications of the Co-Au junction which we shall consider (see Fig. 3.9) include the possibility for a Co atom to be incorporated into the Au chain (CC/ACA/CC and CC/ACC/CC), the possibility for the chain to buckle assuming a zigzag configuration (CC/AAA/CC) and the case of a longer 5-atom gold chain to be formed (CC/AAAAA/CC).

#### Mixed chains

The system with a mixed cobalt-gold wire between cobalt electrodes also shows high spin polarization. We find that the presence of cobalt atoms in the wire (Fig. 3.9(a)) and on the tip of one of the electrodes does not significantly affect the interaction of the pyramid cobalt and gold atoms and does not give significant contribution to the conductance. We can see quite high spin-polarization of conductance in mixed Au-Co chains (Fig. 3.9(a,b)), about 50 – 60%, which is a result of a depletion in  $s$ -states at the tip gold atoms, caused by  $s - d$  hybridization in minority channel between cobalt and gold.

#### Zigzag chain

If we allow the chain to deviate from the linear geometry and relax into a zigzag configuration (Fig. 3.9(c)) we find that the spin-polarization of conductance reaches 90% and the energy-dependent transmission coefficient behavior is practically identical to the one in the case of the linear gold contact. This is consistent with an idea that the  $s$ -shell participating in conductance is spherically symmetric and not strongly susceptible to deviations from the linear geometry. The inter-site electron hopping in that case depends only on the distance

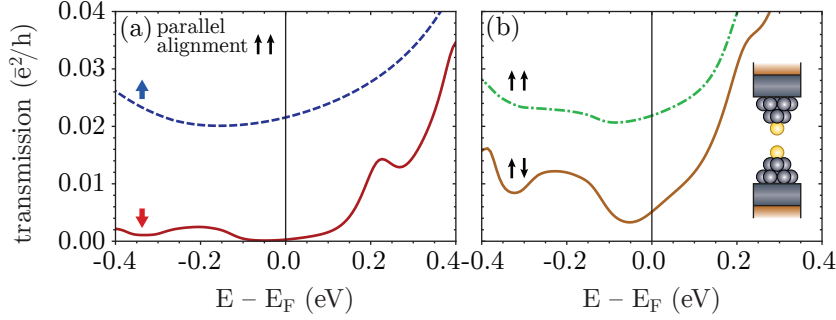


Figure 3.10: (a) Spin resolved transmission of a CC/A-A/CC junction in tunneling geometry with parallel alignment of leads' magnetization. (b) Total transmission in the same junction for parallel and antiparallel alignment of leads' magnetic moments. The inset shows the sketch of the system's geometry.

between the sites. An overall decreasing of the conductance with respect to previous considered systems is caused by the fact, that in zigzag configuration  $d_{z^2}$  orbitals of Au atoms decrease their overlap along with the fraction of conductance for which they were responsible.

### 5-atomic Au chains

It is also worth mentioning that Au is known as a material of choice to construct longer monatomic chains (up to 7-9 atoms). [32] Our calculations yield high conductance polarization for a 5-atomic linear Au chain between Co electrodes (Fig. 3.9(d)). A peak, observed at the Fermi level, has the same origin as the moving peak, discussed in Sec. 3.2. Note, that in the 5-atomic gold chain standing waves can have more modes, than in a 3-atomic chain. Therefore, one can observe more moving peaks in the energy-resolved transmission during the stretching of the chain.

### 3.3.3 Tunnel Au-Co junction

Another interesting system to consider, is a Co-Au tunnel junction – a junction where the largest interatomic gap is too big for the atomic orbitals to overlap and thus disallows the direct hopping of electrons. Transmission in this case has a tunneling character. We calculate the spin-polarized conductance and tunnel magnetoresistance(TMR) for a system shown in the inset of Fig. 3.10(b) using the same technique, as in Sec. 3.2.5. The distance between tip gold atoms was chosen to be 4.8 Å. Calculations were performed for parallel and antiparallel alignment of the electrodes' magnetization.

In Fig. 3.10(a) energy-resolved transmission for majority and minority channel is presented. Estimated zero-bias spin-polarization of conductance in this case reaches 98%. In Fig. 3.10(b) total transmission for parallel and antiparallel magnetization alignments of electrodes is shown. Zero-bias TMR, calculated by the same formula, as in section 3.2.5 reaches 400% in the tunnel regime. Our analysis shows that if the distance between electrodes is further increased, the TMR remains practically at the same level, while conductance itself follows the expected exponential decay rule.



# Chapter 4

## Gate control of 5d-3d metal nano-contacts

While it is extremely important to be able to “program” magnetic properties into atomic-scale junctions at construction stage (which can be done, *e.g.* by tuning the chemical composition and geometry of the junction, as has been discussed in the previous chapter), it is even more important and challenging to devise a way of dynamically and reversibly tuning those properties after the junction has been completed or incorporated into a device. Electronic properties of electronic transistor units are ubiquitously controlled by applying an external bias to the system by means of an additional *gate* electrode. As has been mentioned in the introductory chapter, modern fabrication technologies allow one to create atomic scale contacts with a third electrode placed in proximity for electronic or electrochemical gating. In this chapter we address the question of affecting the spin-polarized transport in nano-junctions by a gate bias.

As a test system we choose alloyed  $3d - 4d$  and  $3d - 5d$  metallic chains suspended between metallic pyramid-shaped leads, no unlike the geometry used in the previous chapter for Co/Au nano-contacts. In particular we start with Fe-Pt chains between Pt leads and after a detailed discussion thereof show briefly that Fe-Pd and Fe-Rh mixed chains behave in a similar fashion.

The choice of Fe/ $4d, 5d$  alloys is motivated by their robust magnetic properties which have been extensively studied both experimentally [35, 57] and theoretically [54, 158]. Contrary to the case of Co/Au studied in the previous chapter, where the spin-polarization of conductance was determined almost exclusively by the Co/Au interface here we aim at having a system in which the leads are non-magnetic and the spin-dependent properties stem from the local magnetism of the chain atoms, which we shall attempt to control by an external gate bias.

### 4.1 Settings of the calculations

All transport calculations and relaxations were performed in the same manner as discussed in Chapter 3. As an LCAO basis set we have chosen double- $\zeta$   $3d$  shell and double- $\zeta$   $4s$  polarized shell for Fe atom and double- $\zeta$   $5d$  shell and double- $\zeta$   $6s$  polarized shell for Pt atom. For Pd and Rh we have chosen double- $\zeta$   $4d$  shell and double- $\zeta$   $5s$  polarized shell. Relaxations of electrodes and nano-contacts were performed with  $5 \times 5 \times 1$  and  $5 \times 5 \times 3$   $k$ -point grids respectively, with a restriction on residual forces of  $0.01 \text{ eV/\AA}$ .

For investigation of electronic effects, related to the influence of a gate bias, we used

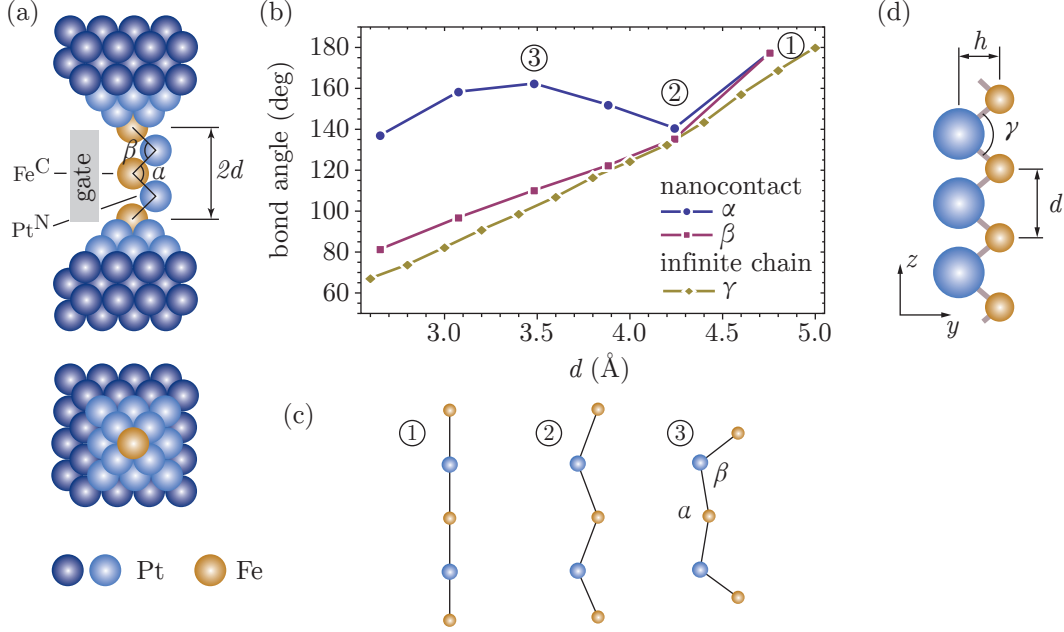


Figure 4.1: Schematic view of the nano-contact used in calculations: (a) nano-contact with a gate area, parameterized by distance  $2d$  between the electrodes and the bond angles  $\alpha$  and  $\beta$ . (b) Dependence of bond angles of the nano-contact and an infinite Fe-Pt chain on stretching. (c) Different types of nano-contact chain geometry, appearing during the stretching of the contact. (d) infinite chain, parameterized by distances  $d$ ,  $h$  and bond angle  $\gamma$ .

state-of-the-art functionality available in SMEAGOL code [148]. The gate is represented by a finite volume in space next to the nano contact with added constant background charge. In the calculation an electrostatic potential, created by the charged gate area is added to the Hartree potential which is then used in the DFT-NEGF scheme, as described in the Sec. 2.4.2. To keep the whole system neutral, a charge opposite to the gate charge is added to the nano-contact. In the following discussion, the gate charge is measured in units of proton charge  $\mathbf{p} = -q_e$ , where  $q_e$  is, of course, the electron charge.

## 4.2 Fe-Pt atomic contact

### 4.2.1 Geometry

The geometry of the system was chosen as 5-atom Fe-Pt mixed chain placed between Pt electrodes constructed from an  $fcc(001)$  slab and a 14-atom tip above (Fig. 4.1(a)). Lattice constant for the slab construction was taken to be  $3.90 \text{ \AA}$ , which is the equilibrium bulk lattice constant calculated with SIESTA. The tip had 3 layers with 9, 4 and 1 atoms in each layer respectively. To imitate the electrode surface, we have taken a unit cell of the slab part of the electrode with a thickness of 8 atomic layers and  $4 \times 4$  atoms in cross-section perpendicular to the transport direction ( $z$ ). Before the final construction of the nano-contact the electrode was fully relaxed.

The Fe-Pt chain consisted of 3 Fe and 2 Pt atoms and was suspended between two electrodes in such a way that edge Fe replaced the apex Pt atoms in the tips of the electrodes (Fig. 4.1(a)). We shall denote the central Fe atom as  $\text{Fe}^C$  and the neighboring Pt atom as

Pt<sup>N</sup>. The chain and the 4 tip-pyramid atoms in contact with it were then allowed to relax without constraints. The dependence of the chain's geometry (parametrized by bond angles as shown in Fig. 4.1(a)) on the inter electrode distance ( $2d$ ) is presented in Fig. 4.1(b). The distortion of the chain was compared to the one an infinite chain would exhibit (Fig. 4.1(c)) if it had the same projected inter-Fe distance  $d$  (projection of the Fe-Fe distance onto the axis of the chain, that is). Note, however, that the gate bias can affect the geometry of the contact in which case the actual  $d$  might deviate from the one obtained in the original relaxation. In our study  $d$  ranged from 2.6Å to 4.75 Å.

## Relaxation of the system

In Fig. 4.1(b) the dependence of the chain's relaxed geometry parameters on  $d$  is shown. Angles  $\alpha$  and  $\beta$  determine nano-contact's bond angles Fe-Pt-Pt and Fe-Fe-Pt respectively, as shown in Fig. 4.1(b). The ideal chain used for comparison is characterized by the zig-zag angle  $\gamma$  (Fig. 4.1(c)).

Relaxation results in Fig. 4.1(b) show that the dependence of the bond angle  $\beta$  (Fe-Fe-Pt) in the nano-contact is close to the dependence of the bond angle  $\gamma$  in the infinite chain, while dependence of the bond angle  $\alpha$  (Fe-Pt-Pt) significantly differs from the case of the infinite chain. In the Fig. 4.1(b) we can distinguish 3 regions (marked by numbers 1 – 3), where the chain of the nano-contact has three types of structure. At large inter-electrode distances the chain stays linear (1) with equidistantly placed atoms, a geometry which persists down to  $d$  values of 4.75Å. As the chain is further compressed the Pt atoms are pushed out from the line of the contact (2). This configuration is still largely similar to the compressed infinite chain and persists in the range of distances from 4.75Å to about 4.25Å. Further compression destroys the linearity of the contact altogether, shifting also the Fe<sup>C</sup> atom away from the axis of the contact (3) and making the angles  $\alpha$  and  $\beta$  deviate from each other. This type of the structure is observed for  $d < 3.9$ Å.

One interesting tendency that can be pointed out is that rather than keeping angles  $\alpha$  and  $\beta$  close and gradually reducing them both, the contact, upon being squeezed, prefers to buckle out and keep both angles large. As our analysis has shown, such difference is caused by energetic properties of the chain: infinite chain has unstable configuration at  $d = 3.4$ Å  $\sim$  3.6Å and, consequently, in the case of unconstrained relaxation nanocontact tends to avoid this configuration. Another reason for it is the attraction between the Pt atoms of the chain and the electrode pyramids. As soon as the Pt<sup>N</sup> atoms are forced by compression out of their place on the axis of the contact they start feeling the pull of the electrodes and are compelled to increase both angles  $\alpha$  and  $\beta$ . Apart from the increased bonding angles, the Pt<sup>N</sup> – Fe<sup>C</sup> distance is increased accordingly which is of importance for the transport properties of such a junction.

## Gate geometry

To simulate the presence of a gate electrode acting on the contact, a rectangular volume with homogeneous charge spread over it is placed close to the chain. In our calculation the box had dimensions of  $4.0 \times 1.5 \times 4.6$  Å and resided some 2.8 Å away from the axis of the contact as shown in Fig. 4.1(a).

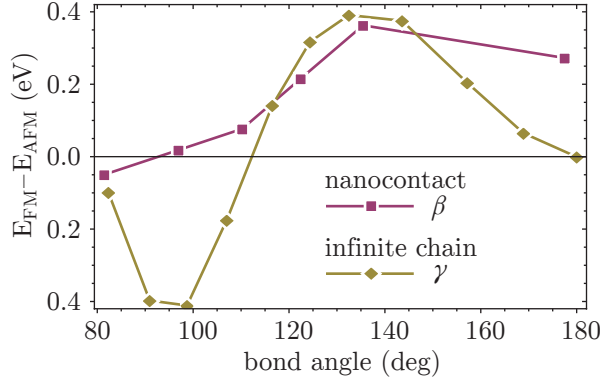


Figure 4.2: Exchange energy of infinite chain dependent on bond angle  $\gamma$  and nano-contact chain dependent on bond angle  $\beta$ .

### 4.2.2 Magnetic configuration

Another crucial aspect of the system is its magnetic behavior. The Fe-Pt mixed systems are known for their rich variety of magnetic properties [159–162]. One property which shall be of special interest to us is the ferro-antiferromagnetic (FM-AFM) transition which can occur as the system’s geometry is changed. In Fig. 4.2) the exchange coupling strength (energy difference between FM and AFM configurations per two magnetic Fe atoms) of the neighboring Fe atoms in an infinite Fe-Pt chain and in contact geometry is shown as a function of the bond angles. In a linear Fe-Pt chains the spins of Fe atoms are very weakly super-exchange-coupled through the Pt atomic orbitals. If the chain is compressed and starts to buckle the antiferromagnetic exchange dominates at bond angles  $\gamma > \sim 110^\circ$  anti-aligning the neighboring Fe spins. For more compact chains the direct interaction of Fe atoms coming closer to each other prevails and the exchange turns ferromagnetic. The behavior of Fe-Fe coupling in the nano contact is rather similar to the one exhibited by an infinite chain. At  $\beta$  angles exceeding  $\sim 100^\circ$  the spins of neighboring Fe atoms are aligned antiparallel with each other while at smaller angles the ferromagnetic coupling prevails. Note, that the Fe-Fe-Pt angles  $\beta$  and  $\gamma$  were chosen as a parameters of the exchange interaction dependence, since the resulting spin alignment can be considered as competition of direct and super-exchanges, the latter of which can be parametrized by the Fe-Fe-Pt bond angle. In the following we shall discuss the effect of the gate bias on magnetic properties of both FM and AFM configurations of the chain to better understand the physical origins of the effects, but we shall keep in mind that for a larger part of the  $d$  value range the ground state of the contact’s chain is antiferromagnetic, although for the compressed junction the ferromagnetic Fe spin alignment is more favorable.

### 4.2.3 Gate influence

Now let us see whether the magnetic properties of the nanocontact chain are susceptible to the influence of an external bias induced by the gate electrode. The dependence of magnetic moments of  $\text{Fe}^{\text{C}}$  and  $\text{Pt}^{\text{N}}$  atoms on the inter-electrode distance measure  $d$  is shown in Fig. 4.3 for ferro- (FM) and antiferromagnetic (AFM) alignment of Fe spins in the contact and for different applied gate biases (actually gate charges  $q_g$ ). Applied gate bias causes very weak change of the exchange energy of the nanocontact, so we will not pay attention to it, but the magnetic moments of the atoms  $\text{Fe}^{\text{C}}$  and  $\text{Pt}^{\text{N}}$  are quite significantly affected by the gate.



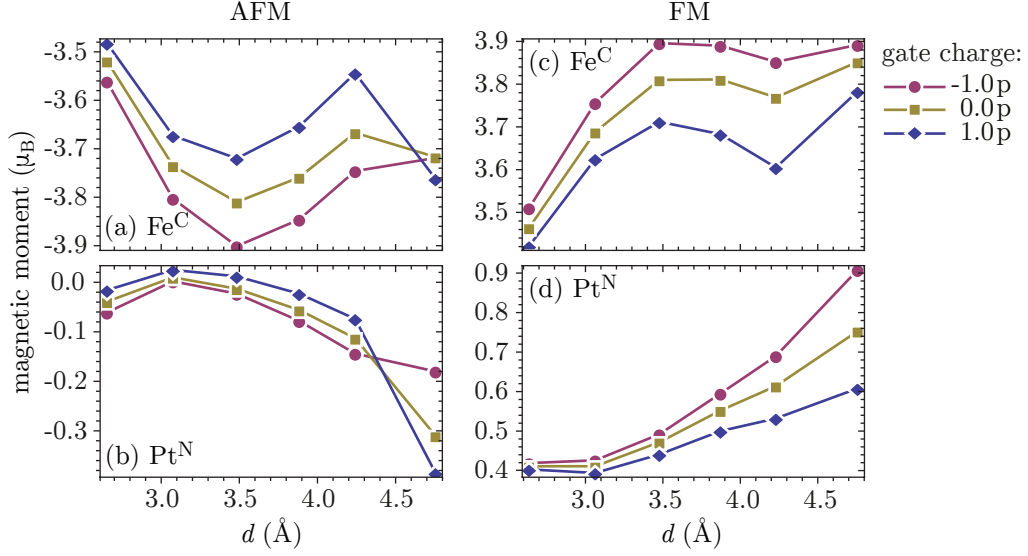


Figure 4.3: Magnetic moments of  $\text{Fe}^{\text{C}}$  (a,c) and  $\text{Pt}^{\text{N}}$  (b,d) atoms in a ferromagnetic (a,b) and antiferromagnetic (c,d) nano-contact as a function of  $d$  for different gate charges.

The strongest change caused by the gate is observed for the  $\text{Fe}^{\text{C}}$  atom (Figs. 4.3(a,c)), where the difference in magnetic moments between neutral and gated contacts reaches  $0.1\mu_{\text{B}}$ . The influence of the stretching of the contact on its magnetic moments is not monotonous. As was discussed in the previous section, for shorter chain distances, the distance between  $\text{Fe}^{\text{C}}$  and  $\text{Pt}^{\text{N}}$  is expanded due to attraction of the  $\text{Pt}^{\text{N}}$  atoms by pyramids, which leads to the isolation of  $\text{Fe}^{\text{C}}$  and an increase of the absolute value of the magnetic moment. For  $d = 3.5\text{\AA} - 4.25\text{\AA}$ , until the chain becomes linear, the distance between  $\text{Fe}^{\text{C}}$  and  $\text{Pt}^{\text{N}}$  gradually decreases, which leads to a decrease in the moment of the  $\text{Fe}^{\text{C}}$  atom.

Pt atoms have no magnetic moment in a bulk, but their magnetic configuration is unstable due to a relatively high density of  $d$  states near the Fermi level. In low-dimensional systems, such as chains, or in the presence of magnetic atoms nearby, Pt can thus easily acquire a significant non-zero magnetic moment. In our case two magnetic Fe atoms are located near each  $\text{Pt}^{\text{N}}$  atom. In the AFM configuration the two anti-aligned magnetic moments of neighboring Fe atoms compete for the right to induce magnetization of  $\text{Pt}^{\text{N}}$ . Since edge Fe atoms have a larger coordination numbers than  $\text{Fe}^{\text{C}}$ , their magnetic moments are smaller than that of  $\text{Fe}^{\text{C}}$ . Thus the induced magnetic moment on  $\text{Pt}^{\text{N}}$  shall be co-aligned with the moment of  $\text{Fe}^{\text{C}}$ . However, since for shorter distances  $\text{Pt}^{\text{N}}$  is shifted closer to the electrode, as discussed above, the influence of the edge Fe atom in compressed contacts shall be comparable with that of the central  $\text{Fe}^{\text{C}}$  atom and the total induced magnetization of  $\text{Pt}^{\text{N}}$  could be close to zero or even co-aligned with the edge Fe atoms. The increase of magnetization of  $\text{Pt}^{\text{N}}$  in an FM contact with increasing  $d$  might also seem contra-intuitive at first, but it can be explained by the increasing degree of isolation of  $\text{Pt}^{\text{N}}$  as the contact is stretched. With increasing  $d$  the magnetization induced on  $\text{Pt}^{\text{N}}$  by neighboring Fe atoms is reduced, but the reduced coordination of  $\text{Pt}^{\text{N}}$  brings Pt closer to the verge of Stoner instability increasing its magnetic moment to  $0.6\mu_{\text{B}} - 0.9\mu_{\text{B}}$ .

It is also apparent the the last point ( $d = 4.75\text{\AA}$ ) of the AFM (and in case of  $\text{Fe}^{\text{C}}$  also the FM) configuration deviates from the common tendency of magnetic moment behavior. For this distance one can observe a reversal of magnetic moment behavior with applied gate bias in AFM configuration and a definite change of the trend in FM configuration. Moreover,

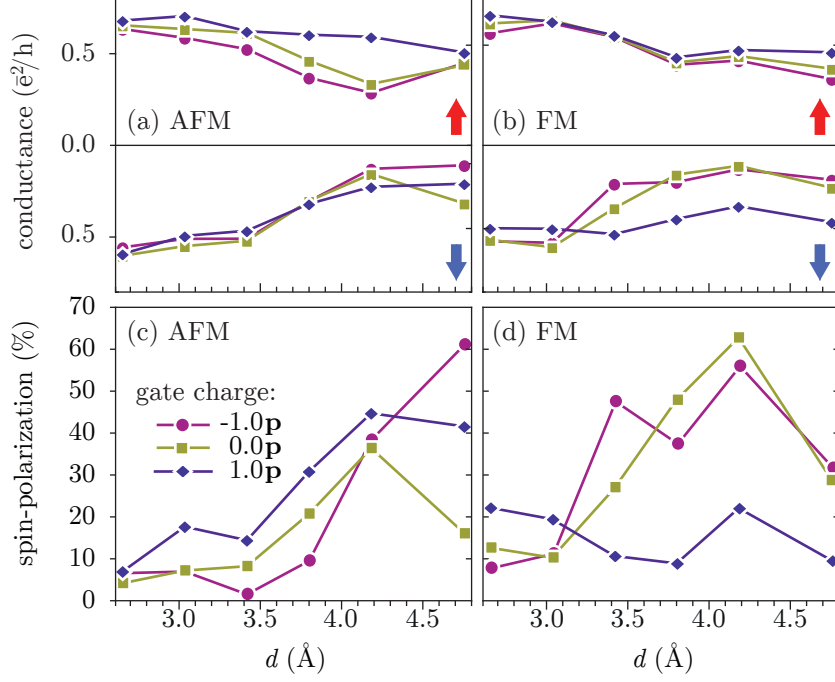


Figure 4.4: Zero-bias conductance for (a) AFM, (b) FM configurations and Spin-polarization of the conductance for (c) AFM, (d) FM configurations of the Fe-Pt nano-contact for different gate charges. Arrows denote spin orientations.

reaction of the Pt atom is more pronounced, than the reaction of central Fe atom. Such behavior will be explained further on in detail. Here we shall only mention, that this is due to a qualitative change in the electronic structure of the contact taking place as the chain switches from zigzag to linear configuration.

One general statement that can be made for all configurations and distances is that the gate bias has a pronounced influence on the magnetic moment of the atoms of the chain. With the possible exception of  $d = 4.75\text{\AA}$  mentioned above, a positive bias tends to reduce the magnetization of both Fe and Pt atoms, while a negative one enhances it. The physics of this effect lies in the phenomenon of field screening, but before we elaborate on that subject let us first take a look at a second effect of the external bias – the change of the junction’s transport properties under the influence of the gate. The subsequent discussion of the field screening in the chain shall then shed light on the common origin of both effects.

#### 4.2.4 Spin-polarized electron transport under bias

Let us start by considering the of gating on the equilibrium (zero bias) transport properties of a Fe-Pt junction. In Figs. 4.4(a,b) spin-resolved zero-bias conductances of FM and AFM configurations of the nano-contact are given as a function of  $d$  for different gate charge values.

The trend with increasing of the distance  $d$  for both configuration is a slight reduction of the conductance, which can be ascribed to the gradual decrease of the direct overlap between the next-nearest neighbors in the chain. Important fact is that the minority conductance decays faster, which leads to a change in conductance spin-polarization (Fig. 4.4(c,d) for AFM and FM configurations respectively), defined as

$$P = \frac{C^\uparrow - C^\downarrow}{C^\uparrow + C^\downarrow}, \quad (4.2.1)$$

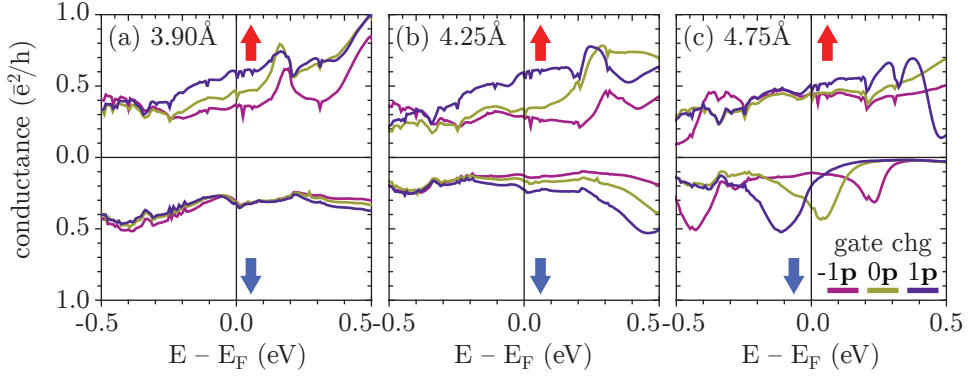


Figure 4.5: Transmission probability of the PtFe nano-contact for different distances (a-c) between electrodes. Arrows denote spin orientations.

where  $C^\uparrow$  and  $C^\downarrow$  are conductances of the spin-up and spin-down channels respectively. Upon stretching, the conductance polarization grows from nearly zero to about 50 – 70%. This can be ascribed to the fact, that in a compressed contact  $\text{Pt}^N$  atoms form a direct almost non-spin-polarized bridge between the electrodes opening an additional conductance channel and at the same time decreasing the conductance polarization. At larger distances electron tunneling path inevitably goes through strongly magnetic Fe atoms, thus the conductance in different spin channels shall be more different.

Coming back to the external bias we note that the effect of gating is very different at different distances. In general, we can see, that in both FM and AFM configurations compressed contacts ( $d < 3.5\text{\AA}$ ) are much less susceptible to external gating than the contacts with distances in the  $3.9\text{\AA} - 4.75\text{\AA}$  range. For example, in the AFM configuration, which is the ground state in most of the  $d$ -range (Fig. 4.4(a)), conductance in both spin channels of a short chain is barely changed by 5% by a gate charge of  $\pm 1\mathbf{p}$ . At  $d = 4.2\text{\AA}$ , however, applying a gate charge of  $1\mathbf{p}$  increases majority conductance by a factor of two while the minority channel is almost unaffected. This alone is already a clear indication that gating is a valid option for tuning the spin-polarization of conductance in Fe-Pt junctions.

Here again the behavior of a liner chain under gating is different from the rest of the  $d$  range. For instance in the AFM configuration, as has just been mentioned, the minority conductance is generally less susceptible to gating than the majority one. At  $d = 4.75\text{\AA}$ , on the contrary, majority conductance practically does not change under external gate bias, while in the minority channel we see a jump from  $0.1 e^2/h$  to  $0.3 e^2/h$  and then a drop to  $0.2 e^2/h$  (variation of 200%) as the gate charge is changed from  $-1\mathbf{p}$  to  $0\mathbf{p}$  to  $1\mathbf{p}$ .

In contrast to AFM configuration, conductance of the FM one shows strong changes in the minority channel (up to 2.5 times) for the distances in the  $3.5\text{\AA} - 4.75\text{\AA}$  range, while the majority channel is significantly affected only for at  $d = 4.75\text{\AA}$  (Fig. 4.4(b)).

To look more carefully into the origin of the gate-induced changes in conductance characteristics of the system we plot in Fig. 4.5 the energy-resolved transmission probability of an AFM contact for  $d = 3.9\text{\AA}$ ,  $4.25\text{\AA}$  and  $4.75\text{\AA}$  at different gate charges ( $-1\mathbf{p}$ ,  $0\mathbf{p}$  and  $1\mathbf{p}$ ). At smaller  $d$  the physics was found to be the same.

First of all let us remark, that at above distances the exchange coupling between Fe atoms in the system is as high as  $0.2\text{eV} - 0.4\text{eV}$ , which means that AFM configuration is stable and cannot be changed by a any reasonable external field.

Comparing Figs. 4.5(a) and 4.5(b) we find that at both  $d = 3.9\text{\AA}$  and  $4.25\text{\AA}$  the trans-

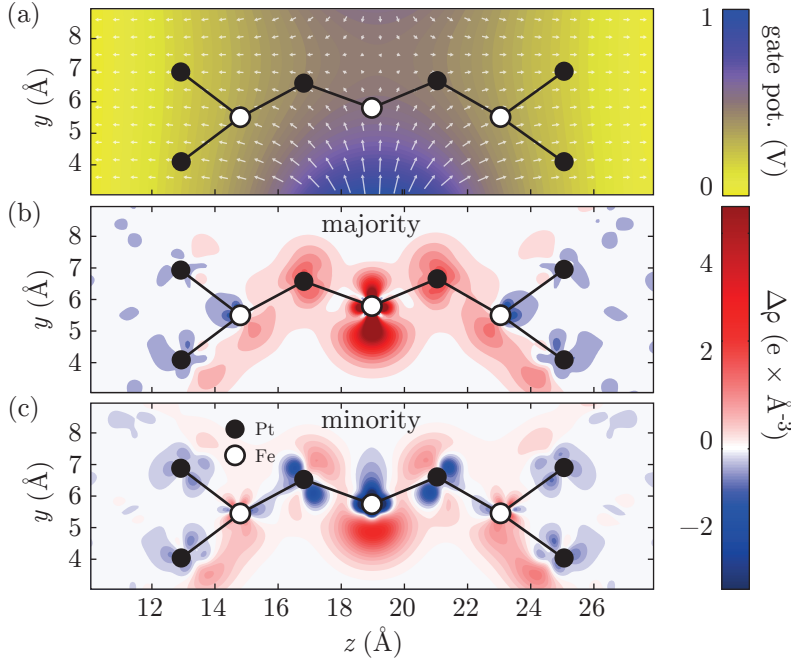


Figure 4.6: (a) Electrostatic potential  $V$  distribution in a plane containing the axis of the contact and passing through the center of the gate electrode (color-coded) and electric field (arrows, defined as  $E = -\nabla V$ ). Majority (b) and minority (c) screening charge density (in units of electron charge  $\bar{e}$ ) in the same plane as the potential plot is made for. Red and blue areas denote excess and lack of electronic charge density of the gate affected system with respect to the neutral system.

mission curves are alike and are changed smoothly by a gate bias, especially at and around the Fermi level. Majority channel transmission is found to be uniformly increased and the minority channel is only weakly affected. The picture of transmission for  $d = 4.75\text{Å}$  (Fig. 4.5)(c) is quite different, however. The majority transmission in this case remains almost unchanged, while in the minority channel we can see a peak, moving through the Fermi level as the gate charge is changed. This causes the jump in minority conductance and conductance spin-polarization mentioned above (Fig. 4.4(a)). To understand where the smooth increase/decrease of conductance in the first two cases and the strong change in the third case come from we first have to determine what part of the nano-contact and in which way is affected by the bias created by the gate electrode.

## 4.2.5 Spin-dependent screening of the gate

Let us start by taking a look at the shape of the electrostatic potential created by the gate and at the charge redistribution in the system that this added potential creates. Electrostatic potential distribution in a plane containing the axis of the contact and passing through the center of the gate electrode is plotted in Fig. 4.6(a). Here the system is characterized by  $d = 4.25\text{Å}$  and a gate charge of  $1\mathbf{p}$ . The color in the figure encodes the magnitude of the potential added by the presence of the gate and the arrows visualize the gradient thereof, *i.e.* the inverse electric field (the length of the arrows is proportional to the field strength). As we can see, the central Fe atom is located in the region with the highest induced potential shift ( $0.4\text{V} - 0.7\text{V}$ ). Neighboring Pt atoms already feel a much smaller imposed potential

(0.2V – 0.4V). The tip Fe and the contact pyramid atoms feel the gate bias in a much lesser extent than Fe<sup>C</sup> and Pt<sup>N</sup> atoms and thus play a much lesser role on the gate-induced transmission and magnetism changes. We shall thus concentrate in the following on the gate-induced changes in occupation and DOS of the latter two atoms.

The electrons of the nano-contact respond to the presence of the added potential by redistributing and trying to screen the field of the latter. In magnetic nano-structures, redistributions of majority and minority electrons can be different, which always has a strong impact on the magnetism of the system [159, 163, 164]. Figs. 4.6(b) and 4.6(c) show the redistribution of the majority ( $\rho^\uparrow$ ) and minority ( $\rho^\downarrow$ ) valence electron densities in response to the field caused by a gate charge of  $1\mathbf{p}$  ( $\Delta\rho^{\uparrow(\downarrow)} = \rho_{1\mathbf{p}}^{\uparrow(\downarrow)} - \rho_{0\mathbf{p}}^{\uparrow(\downarrow)}$ ). For both channels a general trend can be established. The positive charge of the gate draws electrons from the lead bath into the contact region. The redistribution seems to involve orbitals of different symmetries: strongly localized screening charge in the vicinity of the atoms ( $\sim 1\text{\AA}$ ) and the radial non-uniformity thereof hints that the orbitals being populated there are mostly of  $d$  and partially  $p$  character. At larger distances from the atom cores the screening charge is more spatially uniform and can be attributed to  $s$  orbitals being populated. This conclusion is also confirmed by our orbital population analysis which shall be presented shortly. While the chain gain electrons through screening, the tip atoms in the contact pyramid show a mild depletion of electron charge.

From the first glance at Figs. 4.6(b) and 4.6(c) it also becomes apparent that the screening of the gate bias is strongly spin-dependent. In the majority electron channel the electron density is unanimously higher at both Fe and Pt atoms of the chain. Minority electrons, on the contrary, show a mixed behavior at Fe atoms, where the more localized orbitals show a depletion while the screening charge reaches further away from the atoms into the vacuum. An even stronger depletion can be observed for Pt atoms of the chain.

Table 4.1: Change of orbital occupations due to applying a gate with charge  $1.0\mathbf{p}$  to the systems with  $d = 4.25\text{\AA}$  and  $d = 4.75\text{\AA}$ . Arrows denote spin channel.

$d$	4.25 $\text{\AA}$				4.75 $\text{\AA}$			
	$s$	$p$	$d$	$\Sigma$	$s$	$p$	$d$	$\Sigma$
Fe <sup>C<math>\uparrow</math></sup>	0.131	0.022	0.040	0.193	0.076	0.033	-0.004	0.105
Fe <sup>C<math>\downarrow</math></sup>	0.056	0.033	-0.027	0.062	0.121	0.029	-0.005	0.145
Pt <sup>N<math>\uparrow</math></sup>	0.012	0.002	0.033	0.047	0.004	0.003	-0.020	-0.013
Pt <sup>N<math>\downarrow</math></sup>	0.009	0.004	0.001	0.014	0.075	0.012	0.031	0.118

Thus, while in total both spin channels gain electrons due to the screening, the relative occupation of the orbitals in the minority channel is obviously changed, which is likely to change both static and transport magnetic properties of the contact. To put a quantitative hand on the gate-induced orbital population change we resort to the Mulliken analysis of the system [165]. Orbital occupations of Fe<sup>C</sup> and Pt<sup>N</sup> atoms presented in Tab. 4.1 for two stretching distances  $d = 4.25\text{\AA}$  and  $4.75\text{\AA}$ . We see that our visual analysis of the charge redistribution diagram was correct: the total number of electrons is increased by a positive gate bias at both Fe<sup>C</sup> and Pt<sup>N</sup>. The main changes can be attributed to the  $s$  electrons, which are generally more mobile, and partially  $p$  electrons. The behavior of  $d$  orbitals is, however

of much greater interest to us, for here we see a pronounced difference between different spin channels and also between different contact stretching distances  $d$ . We can see that, for example, at the central  $\text{Fe}^{\text{C}}$  atom in a contact with  $d = 4.25\text{\AA}$  the number of majority  $d$  electrons is increased, while the minority  $d$  orbital is even slightly depleted. Such relative change of the momentum carrying  $d$  orbitals easily explains the change in both the magnetic moment discussed and the conductance as discussed in the previous two sections (the latter is determined by the relative change in the orbitals of all symmetries, not just  $d$ ).

Another important insight that we get from the Mulliken analysis is that at  $d = 4.75\text{\AA}$ , linear chain configuration that has consistently refused to follow the general gate-dependence trend, the screening is predominantly done by minority electrons, while in all the other cases majority electron redistribution prevails. The physical reason for that as shall be discussed presently by considering the energy resolved density of states of the contact.

## 4.2.6 Analysis of the density of states

To understand the behavior of the magnetism and the conductance displayed above, we turn our attention to the electronic structure of the nano-contact with and without the gate bias applied. Since  $p$  electrons seem to play a lesser role than  $s$  states in the process of screening (as can be deduced from Tab. 4.1), we shall concentrate in our analysis on  $s$  and  $d$  states alone. Nevertheless, our calculations show that the conclusions attained for  $s$  electrons hold as well for the  $p$  electron states in the system.

In Fig. 4.7 the density of  $s$  and  $d$  states are plotted for  $\text{Fe}^{\text{C}}$  and  $\text{Pt}^{\text{N}}$  atoms of the system with  $d = 4.25\text{\AA}$ . Let us concentrate on the symmetry projected DOS (PDOS) behavior in the vicinity of the Fermi level, since both elastic conductance and magnetism are most susceptible to the changes happening there.

In the PDOS of the Fe we see that the gate bias causes a strong shift of the unoccupied majority  $s$  states peak residing close to the Fermi level (from 0.6 eV to 0.2 eV as the gate bias changes from  $-1 \mathbf{p}$  to  $1 \mathbf{p}$ ). This is accompanied by an increase of PDOS around the Fermi level. Exactly the same trend is observed for majority  $d_{z^2}$  orbital, since the two orbitals are strongly hybridized in the chain geometry (having the same rotational symmetry with respect to the  $z$  axis, maximized for the ideally linear case). Other symmetries of the  $d$  shell are much less susceptible to external gating which can be seen in the plot of the total  $d$  PDOS in Fig. 4.7(c): strong peak around 0.4 eV and smaller one around 0.8 eV move to 0.2 eV and 0.6 eV respectively. At the same time for Pt we only see significant changes in the PDOS of the  $s - d$  hybridized band below 0.5 eV and no significant changes around the Fermi level (Fig. 4.7(d-f)), which barely has any effect on conductance. Minority channel orbitals of both  $\text{Fe}^{\text{C}}$  and  $\text{Pt}^{\text{N}}$  are fairly featureless and thus do not respond to the gate bias.

The fact that the transmission properties of the junction are governed by the PDOS of the  $\text{Fe}^{\text{C}}$  atom is supported by the similarity of the conductance curves in Fig. 4.5 with the  $s - d$  hybridized PDOS in Fig. 4.7(a,b). Thus we see that the gate-bias-controlled increase in majority conductance of the system is due to the gate field induced shift of the  $s - d$  state at the Fermi level. This also directly explains the change in magnetic moment of the  $\text{Fe}^{\text{C}}$  atom under the influence of the gate shown in Fig. 4.3.

A similar analysis can be done for the nano-contact with a linear chain configuration at  $d = 4.75\text{\AA}$ , PDOS of which is shown in Fig. 4.8. Remembering its distinctly different conductance behavior it is not surprising to find that the PDOS of both  $\text{Fe}^{\text{C}}$  and  $\text{Pt}^{\text{N}}$  of a linear contact are quite different from what we had for a zig-zag configuration at  $d = 4.25\text{\AA}$ .

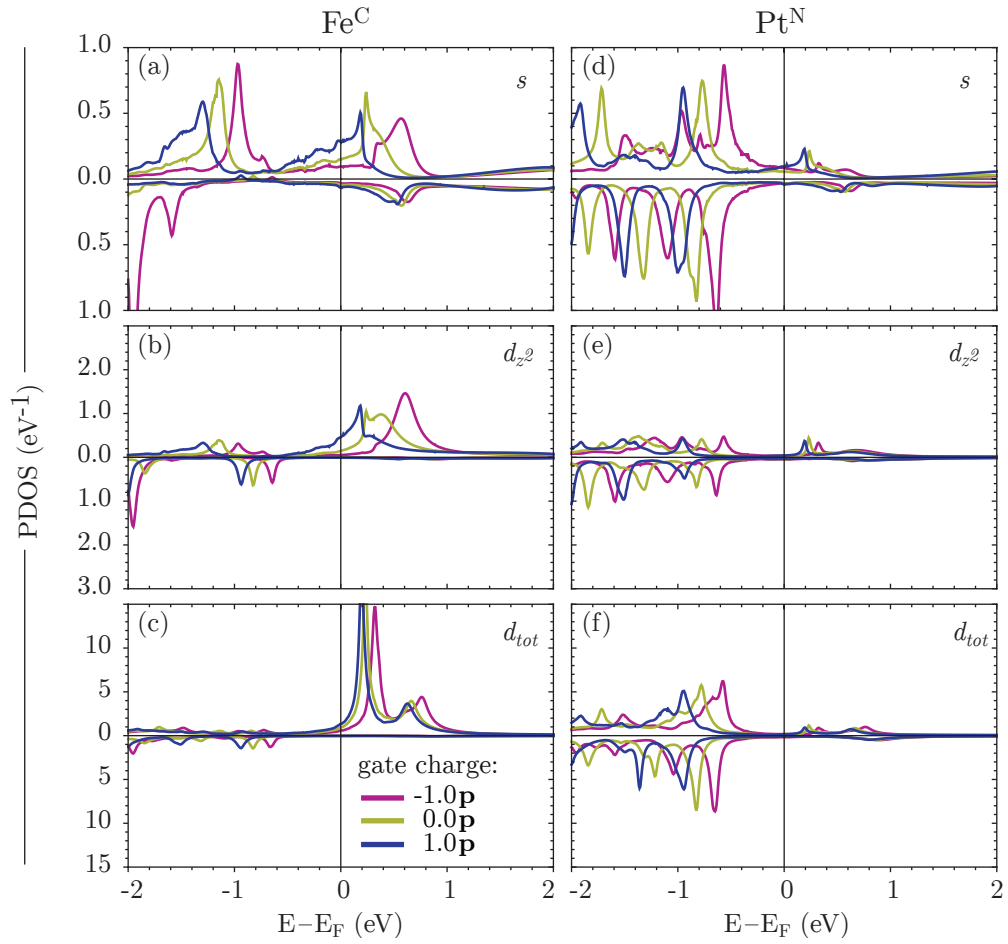


Figure 4.7: Projected density of  $s$ ,  $d_{z^2}$  and  $d_{tot}$  states on (a-c)  $\text{Fe}^{\text{C}}$  and (d-f)  $\text{Pt}^{\text{N}}$  atoms for the system with  $d = 4.25\text{\AA}$ .

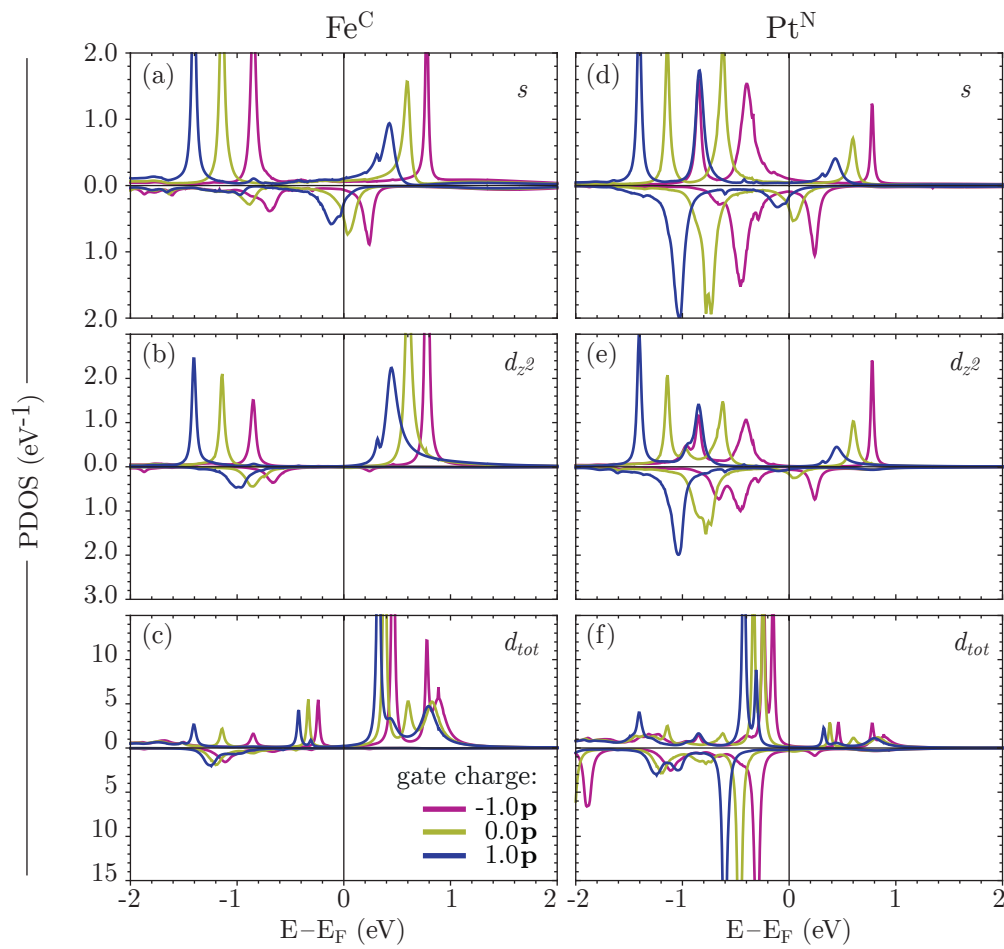


Figure 4.8: Projected density of  $s$ ,  $d_{z^2}$ ,  $d_{tot}$  states on (a-c)  $\text{Fe}^{\text{C}}$  and (d-f)  $\text{Pt}^{\text{N}}$  atoms for the system with  $d = 4.75\text{\AA}$ .



Although majority electrons here behave fairly similar to the case of a zig-zag chain, the Fermi level of  $\text{Fe}^{\text{C}}$  is dominated by a pronounced minority  $s$  peak, which also shifts under gate bias. Since it exceeds in amplitude both majority  $s$  and  $d$  PDOS it also is responsible for the bias-dependent changes in conductance of the junction. Moreover, the PDOS of  $\text{Pt}^{\text{N}}$  is much richer on features in the case of a linear chain (Fig. 4.7(d-f)). Here as well the Fermi level PDOS is dominated by minority  $s$  electrons which are hybridized by bonding with the  $s$ -states of  $\text{Fe}^{\text{C}}$  and shift together with the latter under applied gate bias.

The nature of these peaks discussed above is easily explained by the example of the system with  $d = 4.75\text{\AA}$ . As it was already discussed in Refs. 49, 50, standing waves caused by confinement between two electrodes can appear in the nano-contact and affect its conductance. If we compare positions of the peaks on Fe and neighboring Pt atoms, we notice that these confined states appear as a split version of the hybridized  $s - d_{z^2}$  states in the 3-atomic part (Fe-Pt-Pt) of the whole chain, enclosed between two tips. The reason why we only see the interaction of the 3 atoms and not all 5 of them is that these 3 central atoms have the lowest coordination number while tip Fe atoms are multiply bonded to the next layer of the electrode pyramids and are strongly affected by that bonding.

We thus see that the electrostatic potential introduced by the gate electrode can strongly influence electronic states in the nano-contact and by that change the magnetism and spin-dependent conductance properties of the latter.

Before we move on there are still two remarks to make which should increase the generality of above conclusions. Firstly, a careful observer might remark that the junction in our calculations could easily be influenced by the potential from of the gate in the neighboring unit cell. The latter would be an artifact of calculation and thus not physical. However, our convergence check with respect to the lateral size of the super-cell shows that the results discussed above are already representative and do not qualitatively change with the size of the cell. Another potential ambiguity is the choice of the gate electrode position. To test the robustness of our results we carried out similar calculations as presented above for systems where the gate electrode was located closer to the chain or out of the plane of deformation of the contact wire. The result of conductance calculation were almost the same as shown above. This is also an important hint that the observed effects are really due to the gate potential affecting the confined states in the junction and not due to the local bond polarization which would be rather geometry-dependent.

### 4.2.7 I(V) characteristic

Now that we know that gating can affect the electronic structure of and equilibrium conductance through the nano-junction, it is interesting to take a look at the bias dependence of the I(V) characteristics of the discussed systems. The spin-resolved I(V) curves for differently stretched contacts are plotted in Fig 4.9. Here we present both fully-self-consistent non-equilibrium calculation results (markers in Fig. 4.9) and the estimates (lines) done by integrating the zero-bias transmission around the Fermi level using Eq. (2.3.3). It is apparent, that small biases ( $0.1 - 0.3\text{V}$ ), when the electronic structure of the leads is not strongly changed by the applied bias, equilibrium and non-equilibrium currents are very close to each other. Therefore, simple and quite precise estimation of I(V) characteristics can be done using zero-bias transmission.

The I(V) characteristic of the system have a nearly linear character, which is due to the fact, that transmission-energy dependencies for these systems are relatively smooth around

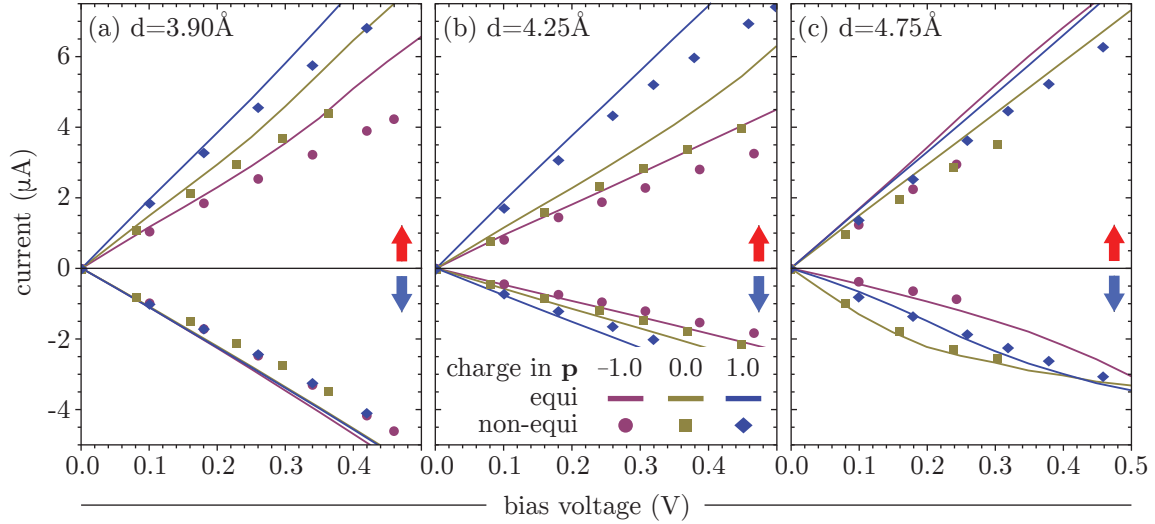


Figure 4.9:  $I(V)$  characteristics for Fe-Pt nano-contact with different distances (a-c)  $d = 3.9\text{\AA} - 4.75\text{\AA}$  respectively and for different gate charges. Non-equilibrium and equilibrium calculations are plotted by markers and solid lines respectively.

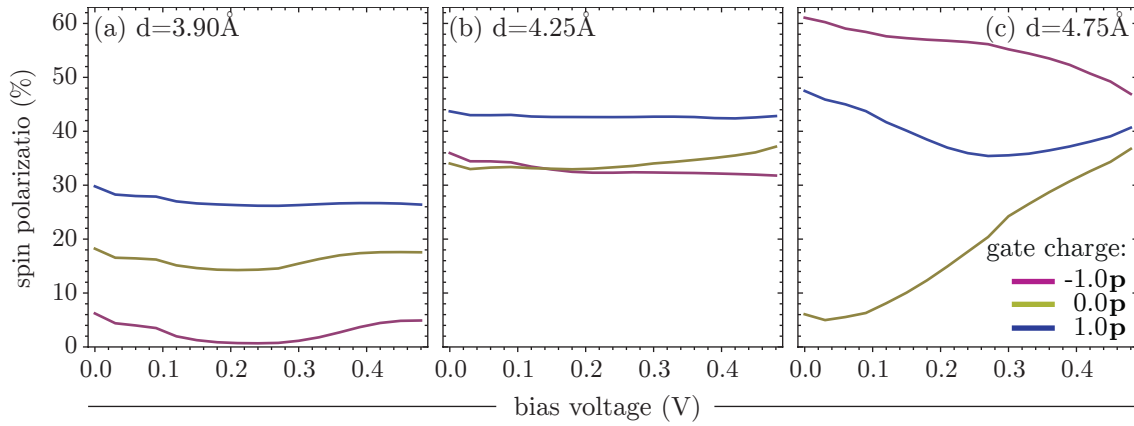


Figure 4.10: Dependence of the current spin polarization on the bias voltage and the gate charge for the distances  $d = 3.90\text{\AA} - 4.75\text{\AA}$  respectively.

the Fermi level. Gate induced motion of the PDOS and transmission peaks leads to a accompanying change in the slope of the  $I(V)$  curve for the corresponding channel. So we see a pronounced influence of the gate bias on majority  $I(V)$  curves for the junctions with  $d = 3.90$  and  $4.25\text{\AA}$  and for the minority  $I(V)$  curve for the  $d = 4.75\text{\AA}$  case. Any non-linearity of the  $I(V)$  curves are due to the sensitivity of the PDOS of the contact atoms to the bias applied between the electrodes, which is only really pronounced in the case of minority electrons of the  $d = 4.75\text{\AA}$  system.

Otherwise, applying a gate voltage between  $-1\text{ p}$  and  $1\text{ p}$  we can change the majority  $I(V)$  slope for  $d = 3.9\text{\AA}$  and  $4.25\text{\AA}$  by a factor of two (Fig. 4.9(a,b)). For the minority  $I(V)$  of the  $d = 4.75\text{\AA}$  system this behavior is slightly more erratic, but for certain voltages the  $I(V)$  slope can be changed by as much as 200% with the same gate biases as discussed above (Fig. 4.9(c)).

Since the  $I(V)$  characteristics of the contact are sensitive to the gate bias, and moreover this sensitivity is spin-selective, we can expect the spin-polarization of the current through

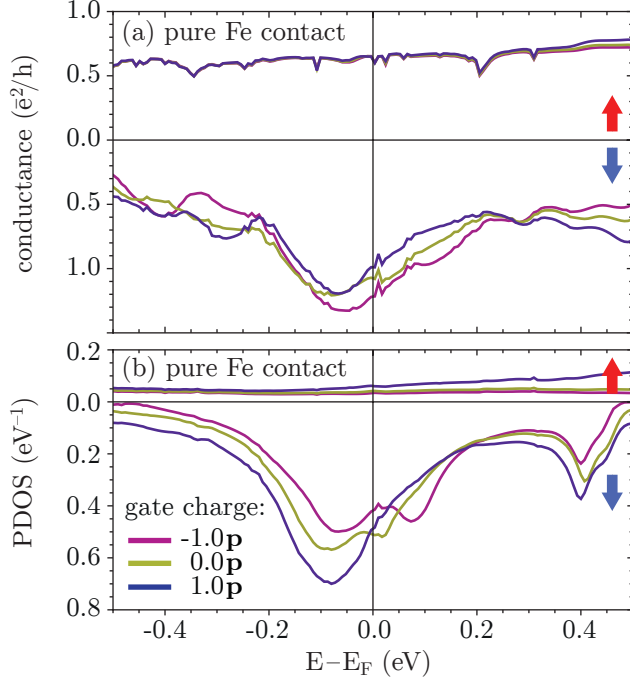


Figure 4.11: (a) Conductance and (b) projected density of  $p$ -states of pure Fe nano-contact in comparing with the  $Fe^C$   $p$ -PDOS (c) of Fe-Pt mixed nano-contact.  $d = 4.25\text{\AA}$

the junction to be equally sensitive to the gate voltage applied. We present in Fig. 4.10 the spin-polarizations as a function of applied inter-lead bias and for different gate biases for the three junctions described above. For  $d = 3.90$  and  $4.25\text{\AA}$  the spin polarization of the current is practically independent of the inter-lead bias but is very sensitive to the gate bias and to the junction geometry. By carefully choosing  $d$  and gate bias we can thus tune the spin-polarization of the current in a wide range of values (0 to 45%). For  $d = 4.75\text{\AA}$  the situation is a bit more tricky. Here as well applying a gate bias can help one tune the polarization of the current by an order of magnitude (from 5 to 60%). The polarization dependence is, however, not constant with the inter-lead bias. Such behavior is caused by the described peak in the transmission, integration of which in Eq. (2.3.3).

#### 4.2.8 The role of Pt in mixed chains

Before we move on to further generalizing the above observations by considering other systems than just Fe-Pt we should spend a few lines to elaborate on the reason, why we have chosen mixed Fe-Pt chains as our test subject in the first place. The reason shall become clear if we consider the difference in conductances of mixed Fe-Pt and pure Fe chains between Pt electrodes. We replaced Pt atoms by Fe in the system with  $d = 4.25\text{\AA}$  and performed test calculation of transport. In this case the system has stable FM configuration. It was found, that total transmission of such system is 2 times higher, but the effect of the gate is less, which in relative values becomes negligible [Fig. 4.11(a)]. From the energy resolved transmission one can see, that minority channel is nearly 4 times larger, than the minority transmission of Pt-Fe mixed contact [Fig. 4.5(b)], but majority one remains at almost the same level. Large value of the minority transmission is connected with a presence of large density of  $p$ -states near the Fermi-level in the pure Fe contact, but in the mixed chain  $p$ -states of Fe

are hybridized with  $p$  states of Pt, which are mostly unoccupied and consequently shifted above the Fermi level. The second reason, why the pure Fe contact has larger conductance is a stable FM configuration, which allows it to form minority  $p$  conducting channel. In the case of AFM mixed Fe-Pt contact the central atom has electronic structure inverted by spin. Therefore, electron hopping from atom to atom in the same channel is suppressed.

Also it was found, that  $p$ -states of Fe has less response to the gate, than  $s$ -states. Since in the pure Fe contact  $p$ -states give main contribution in the transport, the transmission and conductance are less affected by the gate.

As a summary, one can underline the most important results. The electronic structure of the Pt-Fe nanocontact is strongly affected by the magnitude of the gate potential, while the direction of the electric field and, therefore, electronic polarization of the contact are much less important. The shift of the Hartree potential, caused by the gate potential, leads to a shift of the spin-polarized confined states of the Pt-Fe chain, which causes spin-dependent changes in the conductance due to resonant tunneling. The role of the Pt atom in the mixed contact is connected with the presence of the AFM stable configuration and mismatching of electronic states, which leads to the creation of more localized confined states due to the reduced electron hopping between atoms. Another effect of Pt, which will be a subject of future investigations, is a high magnetic anisotropy, which can fix atomic magnetic moments along a certain direction, thus providing a measure of spin-dependent properties in experiments.

## 4.3 Fe-Pd contact

While we have seen that contrary to mixed Fe-Pt, pure Fe chain contacts do not exhibit strong susceptibility to gating, there are other classes of systems that are worth considering. One would be a mixed system, where a  $3d$  element (we remain with Fe) is interspaced with a  $4d$  element (for example, Pd or Rh). Being almost isoelectronic to Pt, Pd and Rh are non-relativistic and more compact, which makes them interesting candidates to check the generality of our conclusions.

### 4.3.1 Geometry

Let us start by considering a contact with geometry similar to the above one (see Fig. 4.1) but consisting of Pd electrodes and a 5-atomic mixed Fe-Pd chain. The equilibrium bulk lattice constant of Pd obtained in our calculations is  $3.86\text{\AA}$ . We shall again denote the atoms of the chain as  $\text{Fe}^{\text{C}}$  for central Fe and  $\text{Pd}^{\text{N}}$  for neighboring Pd atoms (instead of  $\text{Pt}^{\text{N}}$  in Fig. 4.1).

Since Pd has the same valence shell occupation as Pt, certain similarities in electronic structure of Fe-Pt and Fe-Pd systems can be expected to be found. It must, however, be noted that the relativistic nature of Pt often leads to significant differences in the properties of nanostructures comprised thereof. [166] Looking at the relaxed bond angles  $\alpha$  (Fe-Pd-Pd) and  $\beta$  (Fe-Fe-Pd) and comparing them with the bond angle  $\gamma$  of an infinite Fe-Pd chain (Fig. 4.12(a)), we can see that the angle  $\beta$  behaves similarly to  $\gamma$ , while  $\alpha$  reveals a more complicate behavior even than in the case of Fe-Pt. One difference in the relaxation of Fe-Pd nano-contact from the Fe-Pt is that its chain stays buckled ( $\alpha \neq \beta$ ) right up to the point

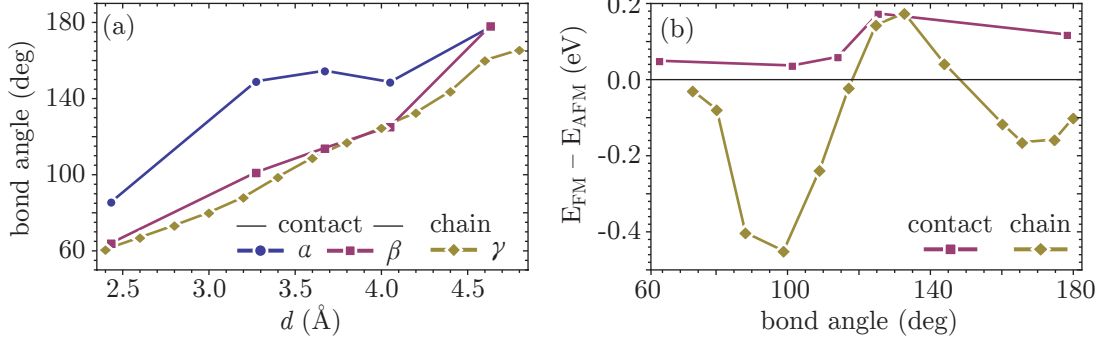


Figure 4.12: Bond angles (a) and exchange interaction of Fe atoms (b) in a Fe-Pd nano-contact compared to an infinite chain.

when it becomes linear ( $\alpha = \beta = 180^\circ$ ) while in Fe-Pt almost-linear contacts already assume a geometry closely resembling Fe-Pt infinite chains.

### 4.3.2 Gating Fe-Pd nano-contacts

For the calculation of transport and magnetic properties under the influence of a gate bias the same technique was used as previously described for Fe-Pt systems in Sec 4.2. The size of the gate was  $4.0 \times 1.5 \times 3.9 \text{ \AA}^3$  and the distance between the gate and the contact axis was  $3.0 \text{ \AA}$ .

Let us consider the magnetic properties of the Fe-Pd nano-contact and compare them with those of an infinite Fe-Pd chain. Fig. 4.12(b) shows the exchange energy values for the nano-contact and the infinite chain as a function of the bond angles  $\beta$  and  $\gamma$ . The infinite chain exhibits a feature-rich behavior having angle ranges with both FM and AFM coupling with FM–AFM transitions at  $\gamma \approx 120^\circ$  ( $d = 3.8 \text{ \AA}$ ) and  $\gamma \approx 157^\circ$  ( $d = 4.4 \text{ \AA}$ ). Dependence of the exchange energy on bond angle  $\beta$  in a Fe-Pd nano-contact is, however, significantly different. In contrast to Fe-Pt system, Fe-Pd nano-contact has no FM–AFM transition and stays AFM-coupled in the whole stretching range. Nonetheless, one can see some correlations between the nano-contact and the infinite Fe-Pd chain, for example the peaks of exchange energy in both systems at bond angles  $\beta, \gamma \approx 130^\circ$ .

### 4.3.3 Transport calculations

Similar to the case of the Fe-Pt system, in Fe-Pd nano-contacts we have found strong dependence of conductance on the applied gate bias. In Fig. 4.13(a) we plot the spin-resolved conductance of the Fe-Pd junction as a function of the stretching parameter  $d$  for different gate charge values. One can see, that most significant changes of the conductance are observed for the distances  $d = 2.4 \text{ \AA}$ ,  $4.0 \text{ \AA}$  and  $4.6 \text{ \AA}$ . Majority conductance for  $d = 2.4 \text{ \AA}$  decreases with increasing of the minority conductance as the gate charge is changed from  $-1$  to  $1$   $\mathbf{p}$ , which causes a sharp increase of the conductance spin-polarization from  $-20$  to  $-60\%$  calculated as per Eq. (4.2.1) and plotted in Fig. 4.13(b). Even more interestingly, for the distances  $d = 4.0 \text{ \AA}$  and  $4.6 \text{ \AA}$  an increase of the majority and a decrease of the minority conductance can be observed, which causes conductance spin-polarization to switch from  $-20$  to  $20\%$ . Therefore, we see that changing the gate bias one can tune not only the degree of the spin-polarization of conductance but also its sign.

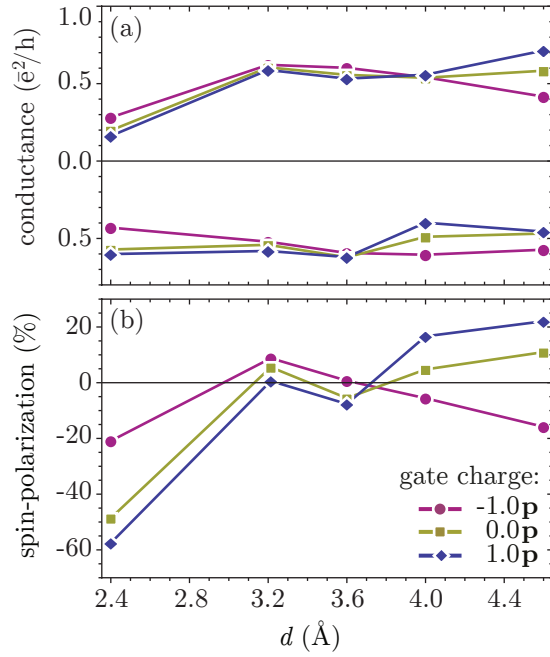


Figure 4.13: (a) Dependence of bond angles of the infinite ( $\gamma$ ) and nano-contact ( $\alpha$ ,  $\beta$ ) chains on stretching distance  $d$ . (b) Exchange energy of infinite chain dependent on bond angle  $\gamma$  and nano-contact chain dependent on bond angle  $\beta$ .

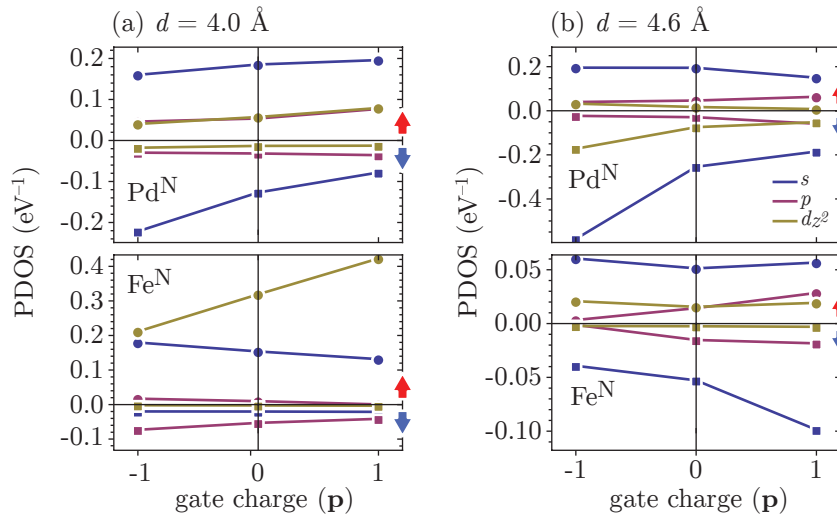


Figure 4.14: PDOS at the Fermi level of the Fe-Pd nano-contact with (a)  $d = 4.0 \text{\AA}$  and (b)  $d = 4.6 \text{\AA}$  for Fe<sup>C</sup> and Pd<sup>N</sup> atoms.

To briefly illustrate the physical mechanism behind the polarization switching let us consider the behavior of the PDOS of the contact at the Fermi level (Fig. 4.14) since it defines the conductance. In the majority channel of the Fe-Pd system with  $d = 4.0\text{\AA}$  (Fig. 4.13(a)) the main strongest influence from the gate bias is received by the  $d_{z^2}$  states of  $\text{Fe}^{\text{C}}$  while in the minority channel the  $s$  states of  $\text{Pd}^{\text{N}}$  change most. However, our analysis shows that  $d_{z^2}$  states of  $\text{Fe}^{\text{C}}$  contribute the least to the total conductance, which is primarily determined by the strong overlap of  $s$  and  $p$  (mainly  $p_z$ ) and thus the response of the majority electrons to the gate bias is determined mostly by  $s$  electrons, the PDOS of which is slightly increased at  $\text{Pd}^{\text{N}}$  and decreased at  $\text{Fe}^{\text{C}}$  resulting in an unchanged net majority conductance. In the minority channel the change of the  $s$  states of  $\text{Pd}^{\text{N}}$  is much more pronounced. Following the  $s$ -PDOS the minority conductance decreases with increasing gate bias. The asymmetric response of majority and minority channels is what makes the spin-polarization of conductance change so rapidly. For the contact with  $d = 4.6\text{\AA}$  the picture is more complicated, since the individual atoms are less screened from the influence of the gate and more of the orbital symmetries are susceptible to gating. The net result is, however close to the case of  $d = 4.0\text{\AA}$ , *i.e.* the spin-polarization of conductance can be switched and subsequently increased if the bias is swept from  $-1\text{ p}$  to  $1\text{ p}$ .

As a side remark, one can note that *a priori* no general statement can be made about which orbitals play the most important role in any particular case. Due to a slight zigzag structure of the chain with  $d = 4.0\text{\AA}$  ( $\alpha = 150^\circ$ ,  $\beta = 120^\circ$ ) the overlap of  $p_z$  symmetry states is lower, than it can be for the linear chain. The states  $p_x$  and  $p_y$ , in turn, lie perpendicular to the transport direction and, therefore, have even smaller overlapping. Consequently, a logical thing to conclude would be that mainly the contribution to the conductance is given by  $s$ -states of Pd and Fe atoms. However, the system with  $d = 4.6\text{\AA}$  has a linear structure and, therefore, overlap of  $p_z$  symmetry orbitals is maximal. Moreover, the  $p$  orbitals have a larger radius, than  $s$  orbitals. Consequently, the hopping integral between  $p$  orbitals will be larger in the case of a linear structure, than the hopping integral between  $s$  orbitals. From here one can say, that, despite magnitude of  $p$  PDOS on Pd and Fe atoms is relatively small,  $p$ -states (mainly  $p_z$ ) give significant contribution to the conductance.

To address the question of finite-inter-lead-bias current, we present  $I(V)$  characteristics for the systems which have proven to be most responsive to the external bias – the nanocontacts with  $d = 4.0\text{\AA}$  and  $4.6\text{\AA}$  – in Fig. 4.15. Here, as in the case of Fe-Pt the current calculated from the zero-bias transmission characteristics coincides well with the fully self-consistently calculated non-equilibrium current. We thus kept the amount of numerically intensive non-equilibrium calculations to a minimum necessary to ascertain the convergence and have calculated the full range of the curves presented in Fig. 4.15 from the zero-bias transmission curves.

Looking at Fig. 4.15 one can see that  $I(V)$  dependence behaves almost linearly, as was the case for Fe-Pt. According to the conductance, presented at the Fig. 4.13(a), slope angle of  $I(V)$  lines differs by a factor of two for different gate charges in the minority channel for  $d = 4.0\text{\AA}$  (Fig. 4.15(a)) and the majority one for  $d = 4.6\text{\AA}$  (Fig. 4.15(b)). Since  $I(V)$  characteristics are linear, their spin polarization doesn't depend on voltage and equals to the spin polarization of the conductance and with the latter can be deliberately tuned in a wide range by choosing the appropriate gate bias.

To conclusion, conductance of the Fe-Pd nano-contact can also be significantly influenced by gating the junction. Despite the general similarity of electronic structure of Pt and Pd, slight differences (f.e. strong  $s - p$  hybridization) give raise to new effects in the conductance

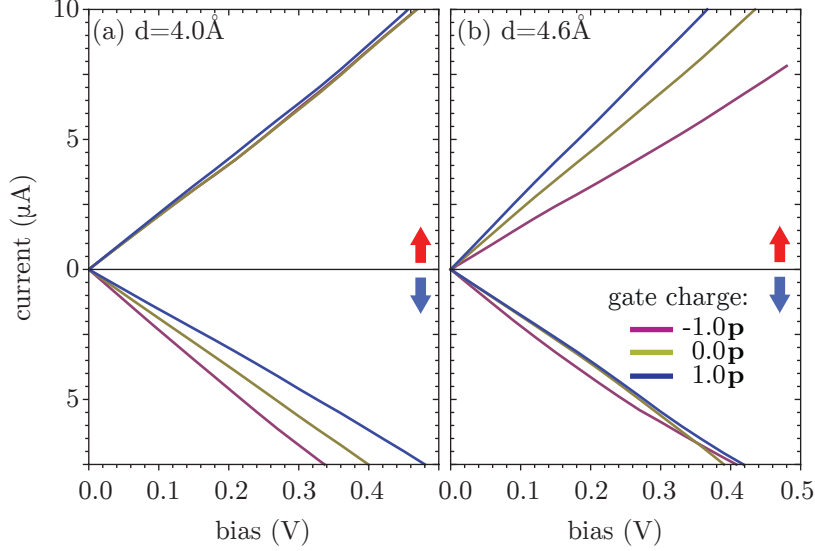


Figure 4.15:  $I(V)$  characteristics for Fe-Pd nano-contact with different distances (a,b)  $d = 4.0\text{\AA}$ ,  $4.6\text{\AA}$  respectively and for different gate charges, calculated by the equilibrium method.

of a Fe-Pd junction, such as the change of spin-polarization sign. Test calculations with pure Fe chain between Pd electrodes showed similar effect, as were found in pure Fe chains between Pt electrodes, *i.e.* large amplitude of  $p$ -states near the Fermi level, which form an efficient conduction channel but are only weakly affected by the gate.

## 4.4 Rh-Fe atomic contact

For completeness we also investigated the conductance through Rh-Fe mixed chains between Rh electrodes with an equilibrium lattice constant of  $3.740\text{\AA}$ , which were constructed analogous to the ones discussed above.

As in the previous systems magnetic configuration of Rh-Fe nano-contact was found to be AFM in the investigated  $d$  range of  $2.4\text{\AA}$  to  $4.0\text{\AA}$ . At the same time an infinite Rh-Fe chain reveals a FM–AFM transition at  $d = 3.4\text{\AA}$ , which is close to the FM–AFM transition geometries of the Fe-Pt and Fe-Pd infinite chains.

We plot in Fig. 4.16(a) the conductance of the Fe-Rh nano-contact for three different distances  $d$  in dependence on the gate charge. Most significant changes are observed for  $d = 4.0\text{\AA}$  where we can see that the spin-polarization of the conductance changes its sign due to an increase in majority and a decrease in minority conductances. We find that such behavior is caused by a slightly different reactions of  $s - d_{z^2}$ -hybridized states of the  $\text{Rh}^N$  in different spin channels. Looking at the PDOS in Fig. 4.16(b) one can see that with changing of the gate charge the majority  $s$ -states peak around the Fermi level is shifted to lower energies increasing the Fermi level PDOS, which leads to an increase in transmission and consequently the conductance. Minority peak in  $s$  and  $d_{z^2}$ -states around the Fermi level moves away from the Fermi level faster, which causes decreasing of the minority PDOS at the Fermi level and thus also the conductance of the minority channel. Regarding another electronic states we can say, that, as it follows from our analysis, their contribution to the conductance is significantly lower due to low magnitude of PDOS on the Fermi level.

Equilibrium  $I(V)$  characteristic and bias voltage dependent spin polarization calculated



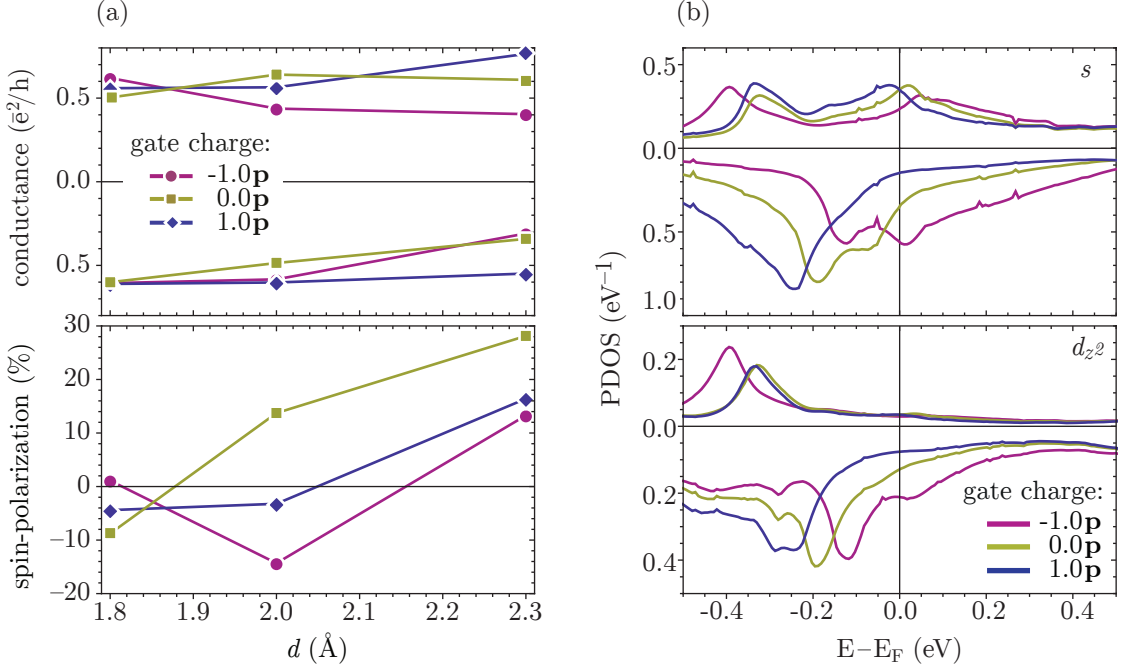


Figure 4.16: (a) Conductance (top) and its spin-polarization (bottom) of the nano-contact for different distances  $d$  and different gate charges. (b) Projected density of  $s$  (top) and  $d_{z^2}$  (bottom) states of the  $\text{Rh}^N$  atom, which gives most important contribution to the transport.

for Fe-Rh junctions with  $d = 4.0\text{\AA}$  and  $4.6\text{\AA}$  are presented in Fig. 4.17. As we see,  $I(V)$  characteristics have a slight deviation from the linear structure, which affects the spin polarization dependence on the bias voltage. As already mentioned, the systems have a peak in transmission at the Fermi level which moves under the applied gate bias. Therefore, we see the same effect as in the Fe-Pt system. The polarization is reduced due to an integration of the peak in transmission. For the system with  $d = 4.0\text{\AA}$  the spin-polarization goes to zero with increasing gate bias. For  $d = 4.6\text{\AA}$  the spin polarization goes toward a value of 20%.

## 4.5 Summary

To summarize the chapter, we have shown by the example of mixed Fe-Pt/Pd/Rh nano-contacts shaped as mixed chains between non-magnetic (Pt/Pd/Rh) electrodes, that due to a direct coupling of the chains to the electrodes (strong coupled quantum dot) the systems form conducting channels with relatively high transmission. At the same time due to the appearance of confined states in the chain transmission at some energies has a resonant tunneling character. Magnetic splitting of the states due to the presence of magnetic Fe atoms causes a difference in Fermi level transmission in different spin channels. Most importantly, applied gate bias was shown to induce a shift of the confined states thus directly affecting the conductance. The latter can be thus tuned within a factor of 2 in different spin channels and its polarization can be enhanced by as much as 200%, quenched or even reversed in sign.

We hope that this investigation shall incite further interest in gate-control over the spin-polarized transport in atomic-scale junctions and belt both science and technology towards on the way towards the creation of new gate-manipulated spintronic devices.

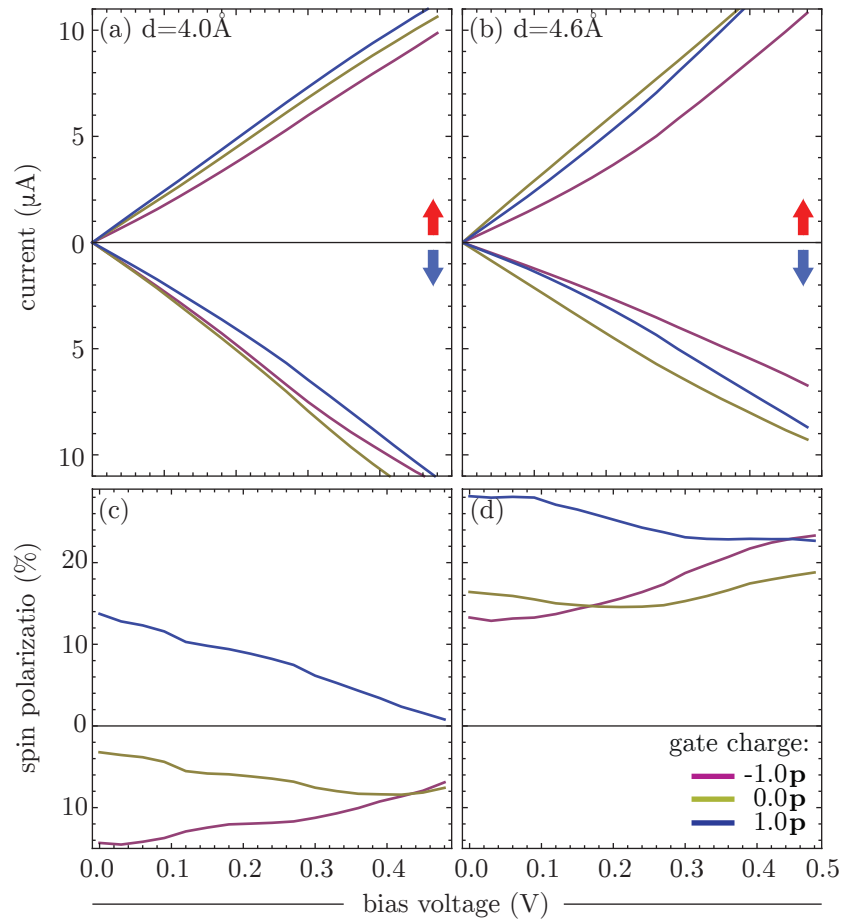


Figure 4.17: (a,b)  $I(V)$  characteristics and (c,d) current spin polarization for Fe-Pd nanocontact with distances  $d = 4.0 \text{ \AA}$ ,  $4.6 \text{ \AA}$  respectively and for different gate charges, calculated by the equilibrium method.

# Chapter 5

## GdN-based systems as a spin-filter devices

Up to now, when we were speaking of nano-scale contacts we have been implying single-atomic junctions, where the magnetic properties of the junction and its spin-filtering characteristics stemmed from the atomic dimensions of the contact's geometry perpendicular to the direction of electron transport. It is, however not always advantageous to work with such junctions, especially when what one requires is ease of production or higher current throughputs. In those cases it is often better to resort to atomic-scale planar junctions, where *atomic-scale* refers to the lateral dimensions of the junction only in the direction of electron transport, which in itself can lend the system unique electronic and magnetic properties.

Since the main subject of the present work is spin-polarized electron transport, we are particularly interested in the magnetic properties of planar junctions. As already briefly discussed in the introductory chapter, with regard to spin-polarized transport layered ferromagnet/insulator junctions deserve special attention. [79–86]

In this chapter we shall tackle the spin-filtering properties of gadolinium nitride – a compound that has a high potential to be used as an efficient spin-filtering tunneling barrier. It is ferromagnetically ordered with Gd showing a magnetic moment of  $7 \mu_B$  per unit cell and a half-metallic electronic structure [6, 112–115] with a gap at the Fermi level in minority spin channel. It is this half-metallicity which makes GdN a promising candidate material for spin-filter devices, as was already suggested by Duan and coworkers. [6] In recent works [116–118] transport properties of GdN films were investigated experimentally and Ludbrook and coworkers [116] were able to achieve a tunneling magnetoresistance ratio (TMR) of 35%. Later, Pal *et al.* and Senapati *et al.* [117, 118] reported observing a spin-polarization of conductance reaching 90% in a GdN film sandwiched between NbN electrodes.

Despite such extensive interest in GdN in recent years, there is a definite lack of theoretical investigations of the transport and spin-filtering properties of the compound which would give a quantitative or qualitative description of the dependence of spin-filtering properties of GdN on different characteristics of the system, such as the lattice parameter or barrier thickness. In the present a detailed explanation of GdN transport properties is given in dependence on the GdN layer thickness and the possibility to achieve spin-filtering efficiency of 100% is highlighted.

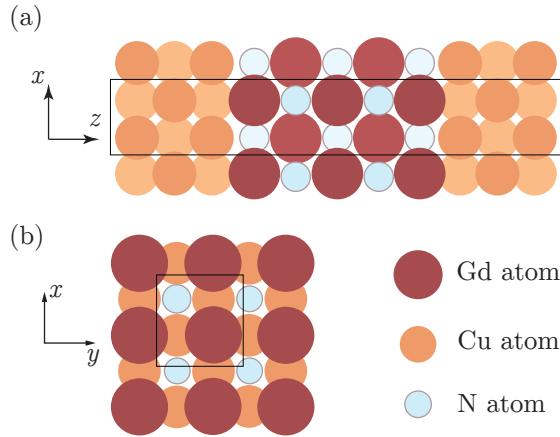


Figure 5.1: (color online) (a) Sketch of the studied system – a Cu/GdN/Cu planar nano-contact. (b) Top view of the last Cu layer and the first GdN layer at the Cu/GdN interface. Black frames denote one unit cell, used for calculation.

## 5.1 Details of calculations

For the calculation of the self-consistent electronic structure and geometry of the systems once again the SIESTA code was used. [140, 141] Transport calculations were performed using the SMEAGOL code. [147, 148]

As an LCAO basis-set for Gd  $6s$  double- $\zeta$  and  $6p, 5d, 4f$  single- $\zeta$  basis orbitals were chosen. The basis for N consisted of  $2s, 2p$  double- $\zeta$  and  $3d$  single- $\zeta$  orbitals. For Cu we chose to include  $4s, 3d$  double- $\zeta$  and  $4p$  single- $\zeta$ .

For the exchange-correlation functional we chose the GGA approximation, since it is known to be more accurate in the description of electronic structure. In the particular case of GdN, GGA yields a gap of 0.68 eV in the minority channel, which is in good agreement with previous studies. [6, 112–115] At the same time, LDA approximation predicts the electronic structure to be metallic in both spin channels.

Since Gd has strongly localized  $f$  valence states, one's calculations need to be able to account of the strong on-site correlation of the  $f$ -shell. To this end, GGA+U approximation was used with  $U = 6.7$  and  $J = 0.7$  as per Ref. 167, where these parameters were calculated from first principles.

## 5.2 Thin GdN film between plane Cu contacts

### 5.2.1 Geometry of the system

The considered model of a planar GdN contact was constructed as an  $fcc$  (001) slab of GdN placed between two Cu(001) electrodes, as shown in Fig. 5.1. A calculation of GdN bulk yields an equilibrium lattice constant of 5.027 Å. The length of face diagonal of Cu(001) is  $a_{\text{Cu}} \cdot \sqrt{2} = 5.191 \text{Å}$ , which is 5% more, than the lattice constant of GdN bulk. Therefore, GdN films can be epitaxially grown on Cu surface at a  $45^\circ$  to Cu(001) lattice with a reasonable mismatch. To simulate this, the lattice constant of GdN was stretched to match that of Cu  $fcc$  face diagonal. A number of layers in the GdN slab varied from 1 to 19 in bilayer steps. The interlayer distances of GdN were allowed to relax freely, thus simulating the case when GdN is grown epitaxially in Cu(001) and subsequently capped again by Cu to form a contact

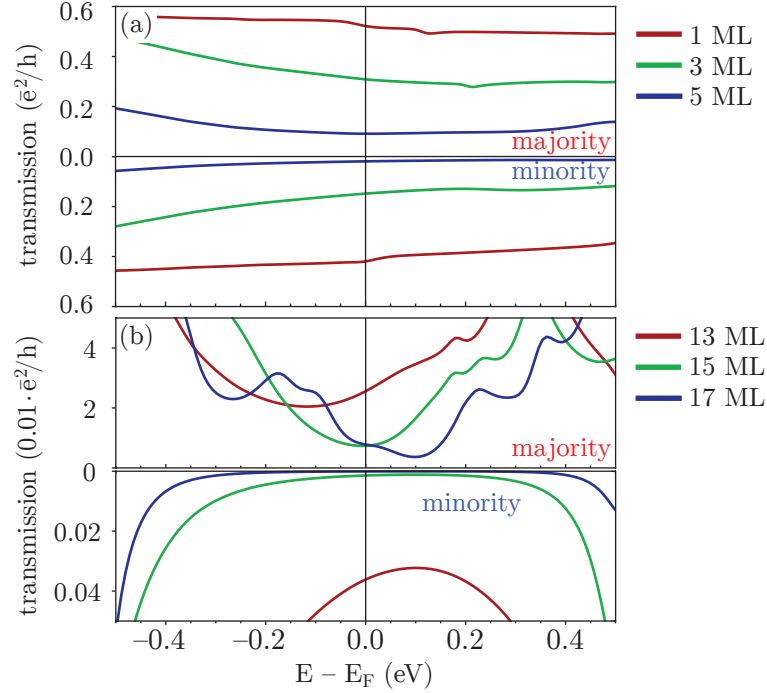


Figure 5.2: Energy-resolved transmission probability of a Cu/GdN/Cu tunneling junction for (a) 1, 3, 5 layers of GdN and (b) 13, 15, 17 layers of GdN.

junction. Our cartesian reference frame had its  $xy$  plane parallel to the Cu–GdN interface and the electron transport was considered to take place along the  $z$  direction.

### 5.2.2 Spin-polarization of conductance

Let us start by considering electron transmission through a Cu/GdN/Cu junction with a varying thickness of the GdN layer. In Fig. 5.2 the energy-resolved transmission curves for thin (1-5 layers) and thick (13-17 layers) films of GdN are presented. It is apparent that for thin films transmission is practically flat in a wide energy range (Fig. 5.2(a)). The increase of GdN thickness is accompanied by a decrease of transmission amplitude in both spin channels while the shape of the transmission's energy-dependence remains largely unaltered. One may

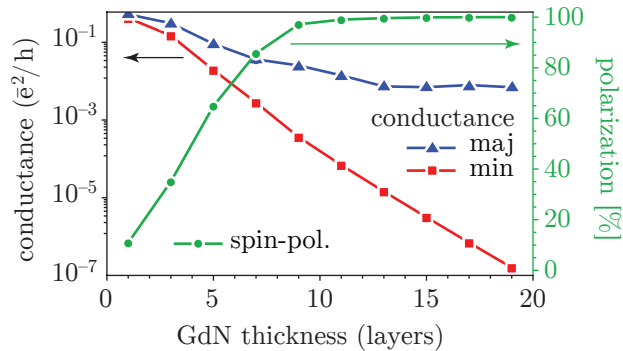


Figure 5.3: Majority (blue triangles) and minority (red squares) conductance of a Cu/GdN/Cu tunneling junction at the Fermi level (logarithmic scale) and the resulting polarization of conductance (green circles) as a function of GdN-layer thickness.

thus see the GdN slab as a tunneling barrier of a homogeneous structure. Transmission of systems with thick GdN films (Fig. 5.2(b)) has a more complicate form and there the GdN electronic structure plays principal role. One can also note a growing difference between majority and minority transmissions with increasing GdN-slab thickness, which is directly reflected in the spin-polarization of conductance.

Fig. 5.3 shows the zero-bias conductance (transmission at the Fermi-level) of a Cu/GdN/Cu nano-junction as a function of GdN layer thickness. The conductance is split into majority and minority electron contributions (blue triangles and red squares, respectively) and is given in logarithmic scale. The spin-polarization of conductance, calculated as  $P = (G_{\uparrow} - G_{\downarrow}) / (G_{\uparrow} + G_{\downarrow}) \times 100\%$  (where  $G_{\uparrow}$  and  $G_{\downarrow}$  are the conductance values in spin-up and spin-down channels, respectively) is plotted in green circles with a corresponding axis on the right. It can be seen that with increasing number of layers the total conductance decreases. The noteworthy fact is, however, that while minority conductance shows a continuous exponential decay with thickness (linear behavior in log scale), majority conductance “saturates” at  $0.007 e^2/h$  when the thickness of GdN exceeds  $\sim 15$  layers. Therefore, the difference in conductance between spin-up and spin-down channels gradually increases, reaching several orders of magnitude and causing the spin-polarization of conductance to approach 100%.

Thus the GdN-thickness dependence of conductance has two distinctly different behavior ranges. For thinner slabs, the transport shall be determined mostly by the interface effects, while for thicker slabs the tunneling can be expected to approach slab-GdN characteristics. Judging from the curves in Fig. 5.3, for GdN the boundary between those two regimes can be drawn at about 12-15 layers. We shall attempt to understand the electronic properties responsible for the conductance characteristics in both regimes.

### 5.2.3 Ballistic view of transport

Since we are interested in GdN’s impressive spin-filtering ability we shall start by analyzing the bulk-like conductance, which is observed for thicker GdN slabs. Even without having a detailed knowledge of the electronic structure of GdN, but only from analyzing the thickness dependence of conductance (Fig. 5.3) we can surmise, that the exponential decay of zero-bias minority conductance is caused by a band gap, while constant majority conductance is a hint, that conductance channels exist in GdN bulk for majority electrons around  $E_F$ . According to Landauer and Büttiker [44], ballistic conductance of the system is determined by the conductance channels, which could be analyzed by considering the density of states and band structure of the bulk of the system.

First of all, let us take a look at the symmetry decomposed projected density of states (PDOS) of GdN-bulk. In Fig. 5.4 the LDOS of  $p_x, p_y, p_z$  states of N and  $d_{xy}, d_{xz}, d_{yz}$  of Gd are shown. The densities of states of other orbitals are too small to be discernible at the scale of the graph and are thus omitted, as they are unlikely to significantly contribute to the ballistic transport. As it was mentioned, GdN and Cu lattices have a mismatch of about 5%, thus GdN/Cu is strained in the plane of the interface. This distortion has an effect of raising the degeneracy between of  $p_x, p_y$  and  $p_z$  states of N (green dotted and solid red curves in Fig. 5.4(a), respectively) as well as of  $d_{xy}$  and  $d_{xz}, d_{yz}$  states of Gd (green dotted and solid red curves in Fig. 5.4(b), respectively). Corresponding  $p$  and  $d$  states of N and Gd in bulk GdN are degenerate and are shown with shaded areas in Figs. 5.4 (a) and (b).

To understand the ballistic transport in GdN and Cu we need to consider their band structures. For simplicity we shall neglect here the distortion of GdN, caused by the Cu–

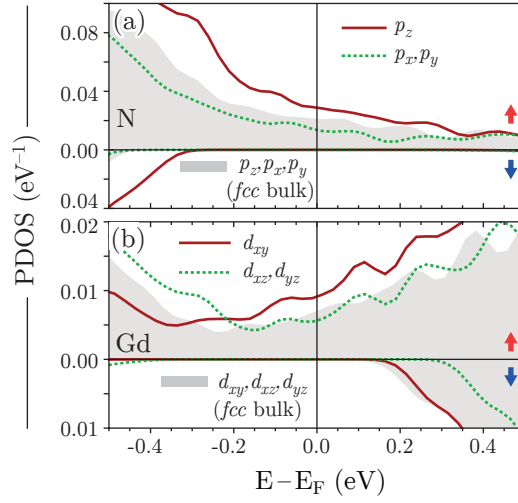


Figure 5.4: (color online) Spin resolved projected density of states of N- $p_x, p_y, p_z$  (a) and Gd- $d_{xy}, d_{xz}, d_{yz}$  states for an infinitely thick slab of GdN epitaxially sandwiched between Cu electrodes (stretched in the  $xy$  plane by 5% and allowed to relax along the  $z$  direction, see text for discussion). Shaded areas present the corresponding DOS of an ideal GdN bulk.

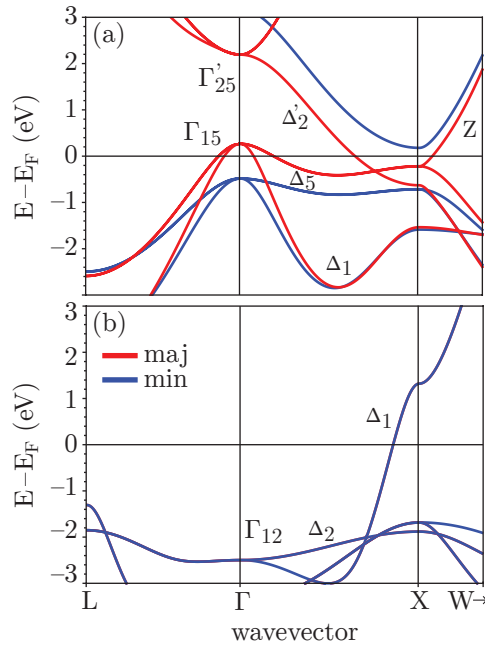


Figure 5.5: Band structure of (a) GdN bulk with equilibrium lattice constant  $5.02\text{\AA}$  (GGA+U) and (b) Cu-bulk with equilibrium lattice constant  $3.63\text{\AA}$  (GGA).

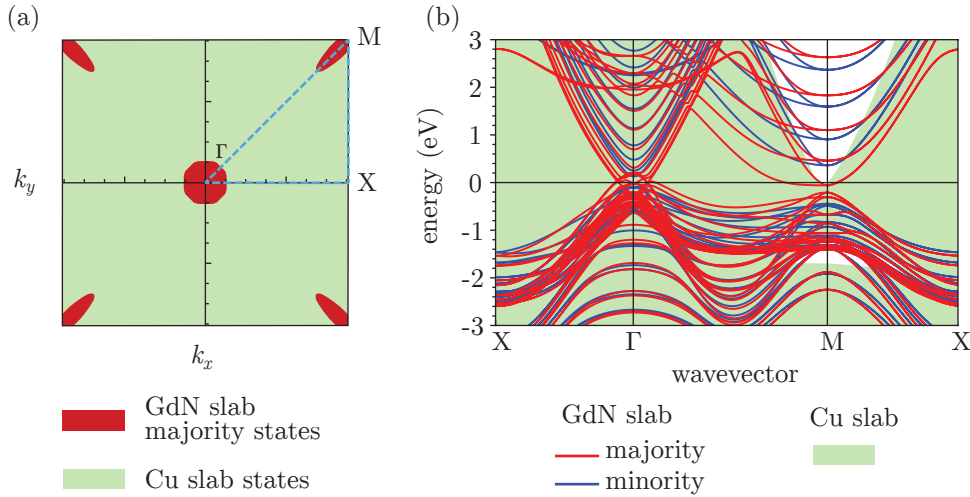


Figure 5.6: (a) Fermi-surfaces of GdN slab (red areas) and Cu slab (light-green area). (b) Band structure of Cu semi-infinite slab (light-green area) and GdN slab with 8 monolayers (red lines – majority, blue lines - minority)

GdN lattice mismatch, since the difference caused thereby is of quantitative character and shall not affect the qualitative understanding. In Figs. 5.5(a) and 5.5(b) the band structures of GdN and Cu bulks along several high-symmetry lines of the Brillouin zone are presented.<sup>1</sup> In Fig. 5.5(b) we can see that the Fermi-level of Cu-bulk is crossed only by the  $\Delta_1$  band, which is comprized mostly of  $sp$  states. These states have almost free-electron behavior, which is reflected in the almost spherical Fermi surface of Cu which is almost spherical [168]. Consequently, interaction of GdN and Cu states can be considered as interaction of GdN states with free-like  $sp$ -electrons, injected from the Cu slab.

In Fig.5.5(a) we can see that the Fermi-level of GdN is crossed by majority  $\Delta_1$  and  $\Delta_5$  valence bands close to the  $\Gamma$  point (red lines). These bands form hole pockets [115] of the Fermi-surface and mainly represent  $p$  states of N. Conduction bands crossing the Fermi level near the  $X$  point and form electron pockets are  $\Delta'_2$  band of Gd  $d_{xy}$  states. Another conduction band  $Z$  along the  $X$ - $W$  direction, which is a continuation of the  $\Delta_5$  band, is represented by  $p_x, p_y$  states of N.

If we consider the band structure of a GdN slab(001) projected onto the (001) plane ( $(k_x, k_y)$  in our cartesian frame), the Brillouin-zone of the system shall have the shape of a square. In Fig. 5.6(a) the Fermi-surfaces of GdN and Cu slabs are presented. Symmetry point  $X$  of the GdN bulk Brillouin-zone is projected onto the  $M$  point of the square Brillouin-zone. Fermi-surface of GdN has several separate sheets (red areas in the Fig. 5.6(a)). Central part around the  $\Gamma$  point is represented by  $p$  states of N and  $d_{xy}$  states of Gd. Other four parts in the  $M$  point reflections with coordinates  $(\pm\pi/a, \pm\pi/a)$  and  $(\pm\pi/a, \mp\pi/a)$  will be represented by Gd( $d_{yz}$ ),N( $p_y, p_z$ ) and Gd( $d_{xz}$ ),N( $p_x, p_z$ ) states respectively. The Fermi-surface of the Cu slab has no features and looks like a uniform background (light-green area in Fig. 5.6(a)), represented mostly by conduction  $sp$  states. Thus we see that in ballistic approximation electron conduction is supported by the GdN bands overlapping with Cu states, *i.e.* states around the  $\Gamma$  point and near the  $M$  point reflections.

To assess the energy dependence of conductance let us look at the band structure of Cu and GdN slabs along the  $X$ - $\Gamma$ - $M$ - $X$  line in the Brillouin zone shown in Fig. 5.6(b). Cu states

<sup>1</sup>A more detailed band structure can be found in Ref. 115, 168.



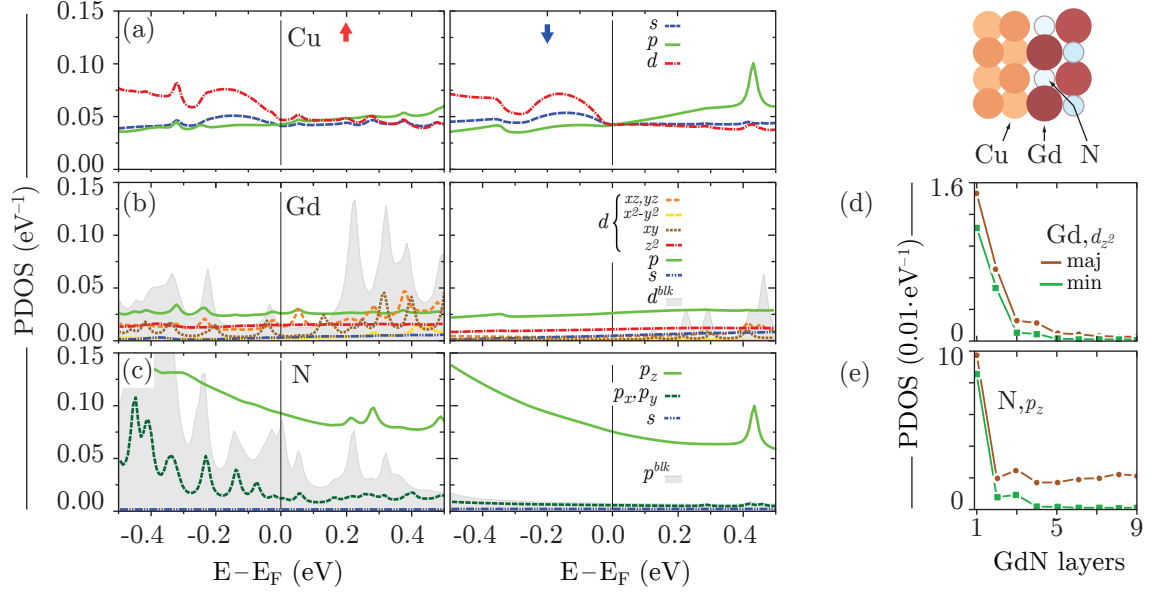


Figure 5.7: (color online) Symmetry decomposed PDOS of the interface Cu (a), Gd (b) and N (c) atoms of a Cu/GdN/Cu junction with 19 GdN layers. Shaded areas in (b) and (c) represent the Gd- $d_{tot}$  and N- $p_{tot}$  PDOS of the central layer of the junction, which is nigh-identical to bulk GdN. Layer resolved Fermi level PDOS of Gd- $d_{z^2}$  and N- $p_z$  states is shown in (d) and (e) respectively.

are represented by a uniform background, since we assume the Cu slab to be semi-infinite. GdN slab is taken as a thin film, Therefore the band-structure looks like a set of dispersion lines. The highest density of band-lines of GdN (and, therefore, density of states) can be observed in majority channel (red lines) at the Fermi level in the vicinity of the  $\Gamma$  point of the square Brillouin-zone. Those are the states (mostly N  $p$  and Gd  $d_{xy}$ ) which can be expected to contribute most to the conductance of the system. The M point can also give a contribution (through Gd  $d_{xz}$  and  $d_{yz}$  states), but it should be much smaller. It can also be seen, that minority channel can give contribution to the ballistic transmission at the energies outside of the band gap (for this GdN slab the gap ranges from  $-0.2$  to  $0.2$  eV. For these energies minority transmission should be determined also primarily by  $\Gamma$  point states.

## 5.2.4 Hybridization and tunneling effects

It must be noted, however, that even at large thicknesses of GdN the conductance is not determined solely by the bulk-like-GdN band structure, but also by the electron injection dynamics from Cu into GdN, which is in turn determined by the hybridization and band alignment at the interface. This hybridization is even more important for electron transport through thin GdN layers, since then it becomes the main factor determining the transmission properties of the junction. To understand the electronic structure of the interface we plot in Fig. 5.7(a-c) the symmetry decomposed projected density of states of the interface Cu, Gd and N atoms (particular atoms are marked with arrows in the inset) of a Cu/GdN/Cu junction with a 19-layer-thick GdN slab. As was the case with the band structure, Cu atoms at the interface have a relatively flat LDOS around the Fermi level with comparable densities of  $s$ ,  $p$  and  $d$  electrons, providing a good basis for hybridization with GdN. Gd atoms at the interface, similar to the bulk ones, have a fairly low density of states around

the Fermi level. Compared to bulk (gray shaded area in Fig. 5.7<sup>2</sup>) the  $d$  states of interface Gd are slightly shifted, due to a mild hybridization with Cu. However only majority  $d_{z^2}$ ,  $d_{xz,yz}$  and  $d_{x^2-y^2}$  are non-vanishing, and even they have a fairly small density, only weakly contribution to the conduction through the interface. The  $p$  states, on the contrary, are non-zero in both spin channels (while their density in bulk is almost zero at the Fermi level) due to hybridization with Cu atoms. In particular,  $p$  LDOS (mainly  $p_z$ , as could be expected) exceeds the density of  $d$  states in both spin channels, thus contributing to conductance, but reducing the polarization thereof. The main hybridization effect, however, can be traced in the density of  $p$  states of interface N atoms. Even in GdN bulk, minority  $p$  LDOS is the dominant contribution at the Fermi level. At the interface not only is the majority  $p_z$  LDOS greatly enhanced, but in the minority channel  $p_z$  states are filled by the overlap with Cu states. Thus nitrogen  $p$  states exceed by almost an order of magnitude the density of any other GdN state at the interface. This efficient hybridization of both majority and minority  $p$  states of N with Cu determine the conductance at the interface, drastically reducing its polarization for thin GdN junctions.

To see how deep into GdN the hybridization goes we plot in Fig. 5.7(d) and (e) the value of the spin-resolved local density of states at  $E_F$  of the dominant hybridized orbitals (N- $p_z$  and Gd- $d_{z^2}$  are shown as representative examples) for different layers of GdN. High at the interface due to hybridization with Cu, both N- $p_z$  and Gd- $d_{z^2}$  LDOS decay as one goes deeper into the GdN slab, achieving their respective equilibrium bulk values by about the 5-th layer. Thus the “direct” electron injection length from Cu into GdN can be estimated to be about 10 – 15 Å. For system with comparable GdN layer thickness the transport shall be determined by the interface properties, rather than by the properties of GdN bulk. A careful examination of conductance behavior with GdN thickness (shown in Fig. 5.3) will reveal at a thickness of about 10 layers (twice 5) a small bend in the exponential decay of the minority and a saturation of majority conductances.

At the end of this section one can summarize, that GdN films between Cu electrodes exhibit spin-filtering properties due to differences in majority and minority electron tunneling, resulting in spin-polarization of conductance reaching 100%. At the Cu/GdN interface, electrons are injected from Cu primarily into  $p$  states of N and  $d_{z^2}$  and  $p_z$  states of Gd. At GdN thicknesses exceeding 5-10 monolayers the gap opens in the minority LDOS, leading to an exponential decay of minority-channel conductance. The tunneling of majority electrons carries a resonant character (based on the GdN bulk electronic levels/bands) and saturates at GdN thicknesses over 10 – 15 monolayers. At those thicknesses the spin-polarization of conductance reaches 100%, producing a high-perfect spin-filtering junction.

### 5.2.5 I(V) characteristics

To give a more application-oriented overview of Cu/GdN/Cu junctions we investigate the behavior of the system under applied bias voltage performing non-equilibrium calculation for biases ranging from 0.0 to 0.5 V. The I(V) curves shown in Fig. 5.8 have a nearly linear structure reflecting the flatness of the non-equilibrium energy-resolved transmission probability around the Fermi level (not shown here). For the voltage range 0.4 – 0.5 V we

---

<sup>2</sup>In fact, the shaded area represents the  $d$  LDOS of the central atom of the 19-atom slab and slightly deviates from the true bulk density shown in Fig. 5.4, exhibiting several peaks, which we ascribe the formation of quantum well states in the finite-thickness GdN slab. The same holds for the appearance of similar peaks in the  $p_{x,y}$  density of states of N (see shaded area in Fig. 5.7(c))

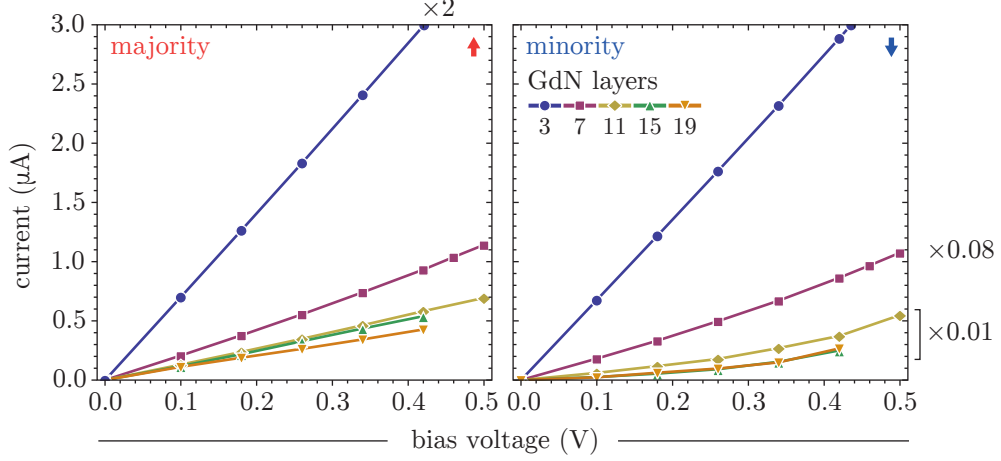


Figure 5.8: Current-voltage characteristics for Cu-GdN-Cu planar contact for different amount of monolayers in the GdN film.

see that minority  $I(V)$  lines of the system with 11-19 monolayers slightly curve up, showing the influence of the edge of a minority GdN bands.

### 5.3 Gd-N chains

While our investigation of GdN was mainly motivated by its exceptional spin-filtering properties in layered-junction geometry, it is conceptually intriguing to see what transmission and spin-filtering properties are exhibited by GdN atomic chains.

We have therefore performed transport calculations for a planar infinite zigzag GdN chain. The chain was constructed of alternating Gd and N atoms ordered in a zig-zag or linear fashion along the  $z$  axis (Fig. 5.9). Calculations were performed for different distances between neighboring Gd atoms  $d$ . The N atoms were always allowed to assume equilibrium positions by fully relaxing the system. The only constrain imposed was the requirement for the system to stay planar in the  $yz$  plane. In this manner, electronic structure and transport properties were obtained for differently stretched GdN chains.

Energy of the chain and equilibrium width  $h$  (extent of the zig-zag along the  $y$  axis) are presented in Fig. 5.9(a) (black circles and gray rectangles, respectively). The chain has a global energy minimum at  $d = 3.8 \text{ \AA}$ , which corresponds to a zigzag structure with parameter  $h = 1.2 \text{ \AA}$ . Transition to a linear structure is rather sharp and occurs after a small energetic barrier at about  $d = 4.2 \text{ \AA}$ .

The coupling between Gd atoms was found to be ferromagnetic regardless of the stretching parameter  $d$ , while N atoms were always coupled antiferromagnetically to Gd. Such GdN magnetic structure coincides with the bulk one. Magnetic moments of N and Gd in the chain are slightly larger, than they are in the bulk ( $0.75 \mu_B$  and  $7.75 \mu_B$  vs  $0.25 \mu_B$  and  $7.25 \mu_B$  respectively), and remain constant practically in the whole studied range of  $d$  (from  $3.2 \text{ \AA}$  to  $4.4 \text{ \AA}$ ). The chain, similar to the GdN bulk, has a gap in minority DOS around the Fermi level for all studied stretching parameters  $d$ . The filled minority band is not affected by stretching, which results in the magnetic moment of the whole system staying constant at ( $7.0 \mu_B$ ) during stretching. Despite the changes in geometry of the zig-zag chain, stretching-induced charge transfer within the chain is small, keeping partial magnetic moments of Gd

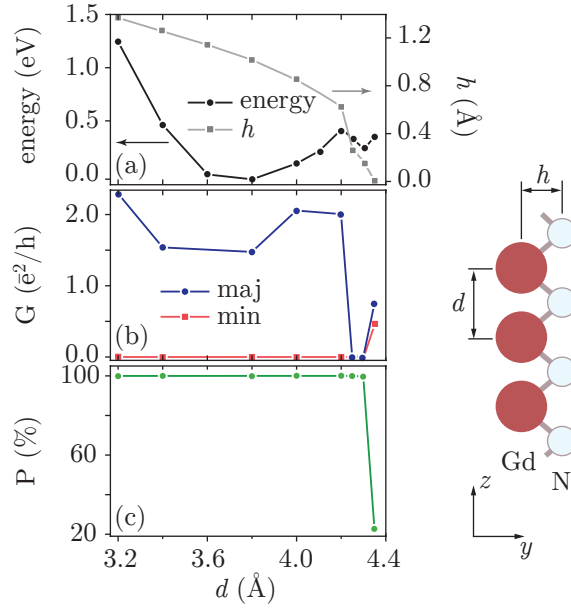


Figure 5.9: (color online) Energy and equilibrium parameter  $h$  (a), spin resolved zero-bias conductance (b) and spin-polarization of conductance (d) of a planar GdN chain (sketch on the right) as a function of the chain stretching parameter  $d$ .

and N constant.

The spin-resolved conductance and its resulting spin-polarization are presented in Fig. 5.9(b) and (c), respectively. In agreement with the gap in minority DOS, the minority channel has zero conductance practically in the whole studied stretching range, which results in a 100% spin-polarization of conductance, making a GdN chain as good a spin-filter as the planar GdN junctions are. There is, however, one intriguing feature in conduction at  $d = 4.3 \text{ \AA}$ . This configuration corresponds to a linear chain and displays an insulating behavior in both spin-channels suppressing conductance altogether (Fig. 5.9(b)). While this feature might have been of interest to technological applications,  $d = 4.3 \text{ \AA}$  is also very close to the point of structural instability of the chain and thus we shall leave its detailed discussion to be a matter of future studies.

Analysis of the projected density of states of Gd and N has shown that the conductance of majority electrons is mostly contributed to by the hybridization of N- $p$  and Gd- $s, d$  states (plotted in Figs. 5.10(upper and middle panels) for  $d = 3.8 \text{ \AA}$ ,  $4.0 \text{ \AA}$  and  $4.3 \text{ \AA}$  (Figs. 5.10(a,b) and (c), respectively). The N- $p$  states are mainly represented by  $p_y, p_z$  symmetries, reflecting the geometry of the chain lying in the  $yz$  plain. Gd  $d$  states are mostly represented by  $d_{z^2}, d_{yz}$  and  $d_{x^2-y^2}$  states. A narrow majority PDOS peak at  $0.4 \text{ eV}$  for a chain of  $d = 3.8 \text{ \AA}$  (which is in fact a narrow band) moves towards the Fermi-level and expands during the stretching of the chain to  $d = 4.0 \text{ \AA}$  forming an additional conductance channel. This explains the increase of majority-spin conduction, as can be observed in Fig. 5.9(b). The shift of that peak can also explain the observed insulating behavior at  $d = 4.3 \text{ \AA}$ . As the chain is stretched from  $4.0 \text{ \AA}$  to  $4.3 \text{ \AA}$  the above-mentioned band shifts away from the Fermi level leaving it devoid of conductance channels (Fig. 5.10(c)).

We thus see that GdN chain share the exceptional spin-filtering properties of planar GdN junctions. Moreover, the adjustability of the chain shape by stretching opens the possibility of switching the transmission properties of the chain between highly spin-polarized

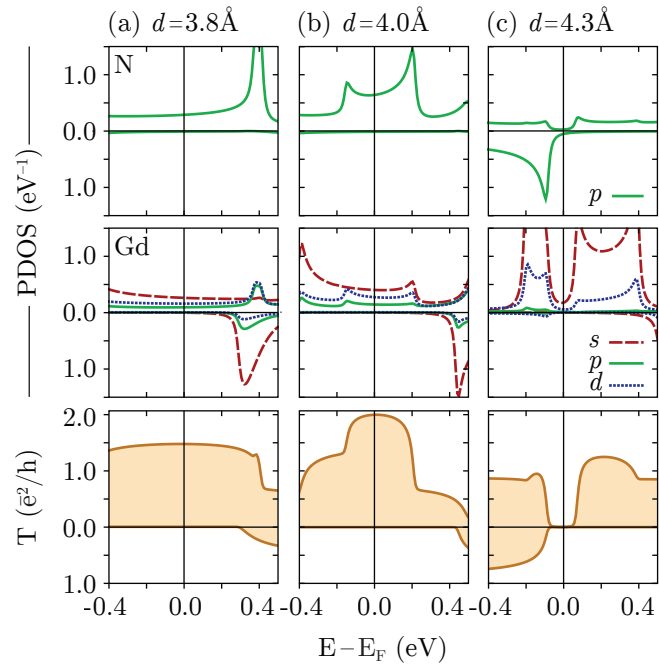


Figure 5.10: (color online) Projected density of states (top panels – N- $p$ , middle – Gd- $s, p, d$ ) and zero-bias transmission coefficients (bottom panels) of infinite Gd-N chain at stretching parameters  $d$  of 3.8 Å (a), 4.0 Å (b) and 4.3 Å (c).

conducting and non-conducting states.



# Conclusion

In the present work, ways of creating and controlling spin-polarized currents in mixed magnetic 1D and 2D systems were investigated. Using a combination of the non-equilibrium Green's function formalism with density functional theory realized in the Smeagol code we performed a series of calculation to understand the behavior of electronic and transport properties of Au–Co nano-contacts, mixed Fe–Pt/Pd/Rh atomic-scale junctions under the influence of a gate electrode bias and planar GdN magnetic tunnel junctions between Cu electrodes.

We find that Au chains suspended between Co electrodes reveal high spin-polarization of conductance due to the strong spin-dependent hybridization of Co–*d* states and Au–*s* states at the Co–Au interface. Each of the two Co–Au interfaces plays the role of a spin-filter, which polarizes the current along the magnetization of the neighboring electrode. Resulting GMR values reach 70% in ballistic and 400% in tunnel regimes (the latter can be achieved, f.e., by over stretching or braking the Au chain). Obtained results explain the surprisingly high GMR values measured previously in similar systems.

As an extension of the set of tools for tuning the spin-polarization of conductance we look into the possibility of affecting the latter with gate bias voltage in a three-terminal device scheme. The junction itself is represented by a mixed Fe–Pt(Pd,Rh) chain suspended between Pt(Pd,Rh) electrodes. The gate is considered as a third electrode brought laterally into the proximity of the chain and put under bias. The redistribution of electrons in the chain in response to the electrostatic potential imposed by the biased gate electrode is found to be strongly spin-dependent and to result in a shift of the confined states of the chain which act as transmission channels. Furthermore, the impact of the gate is found to vary for chains with linear and compressed/buckled geometries. As a result, even small gate biases can cause conductance to change by as much as 200%. More importantly, by adjusting the bias the spin-polarization of conductance can be enhanced, quenched or even reversed which is exactly what is required for potential atomic-scale spintronic applications.

For the cases when planar contact geometry might be preferable to the single-atomic-junction one, we consider an interesting compound, GdN, for the role of a spin filter. Transport properties of a junction consisting of a GdN layer sandwiched between Cu electrodes are investigated and found to depend strongly on the thickness of the GdN layer. This thickness dependence is found to have two distinct regimes. For thick layers the conductance polarization is high and governed by the half-metallic properties of the GdN bulk, while for thin GdN layers the conductance is found to depend on the hybridization at the GdN–Cu interface and be strongly reduced thereby. We find, that in the thick-layer regime the conductance has a ballistic character in majority channel and is provided for by *p* states of GdN,

while in the minority channel the conductance has a purely tunneling character and falls off exponentially with GdN layer thickness. This allows one to tune the spin-polarization of the current to a desired value by adjusting the thickness of the GdN layer. Obtained results of spin polarization dependence on thickness of the layer are in good agreement with recently performed experiments.



# Bibliography

- [1] D. Howe, M. Costanzo, P. Fey, T. Gojobori, L. Hannick, W. Hide, D. P. Hill, R. Kania, M. Schaeffer, S. St Pierre, S. Twigger, O. White and S. Y. Rhee. *Big data: The future of biocuration*. Nature, **455**, 47 (2008).
- [2] X. Espinal, G. Adde, B. Chan, J. Iven, G. L. Presti, M. Lamanna, L. Mascetti, A. Pace, A. Peters, S. Ponce and E. Sindrilaru. *Disk storage at CERN: Handling LHC data and beyond*. J. Phys. Conf. Ser., **513**, 042017 (2014).
- [3] I. Žutić and S. Das Sarma. *Spintronics: Fundamentals and applications*. Rev. Mod. Phys., **76**, 323 (2004).
- [4] A. Bernand-Mantel, P. Seneor, N. Lidgi, M. Muñoz, V. Cros, S. Fusil, K. Bouzehouane, C. Deranlot, A. Vaures, F. Petroff and A. Fert. *Evidence for spin injection in a single metallic nanoparticle: A step towards nanospintronics*. Appl. Phys. Lett., **89**, 062502 (2006).
- [5] S. Egle, C. Bacca, H.-F. Pernau, M. Huefner, D. Hinzke, U. Nowak and E. Scheer. *Magnetoresistance of atomic-size contacts realized with mechanically controllable break junctions*. Phys. Rev. B, **81**, 134402 (2010).
- [6] C.-G. Duan, R. Sabiryanov, J. Liu, W. Mei, P. Dowben and J. Hardy. *Strain Induced Half-Metal to Semiconductor Transition in GdN*. Phys. Rev. Lett., **94**, 237201 (2005).
- [7] M. N. Baibich, J. M. Broto, A. Fert, F. N. Van Dau and F. Petroff. *Giant Magnetoresistance of (001)Fe/(001)Cr Magnetic Superlattices*. Phys. Rev. Lett., **61**, 2472 (1988).
- [8] G. Binasch, P. Grünberg, F. Saurenbach and W. Zinn. *Enhanced magnetoresistance in layered magnetic structures with antiferromagnetic interlayer exchange*. Phys. Rev. B, **39**, 4828 (1989).
- [9] P. Grünberg, R. Schreiber, Y. Pang, M. B. Brodsky and H. Sowers. *Layered Magnetic Structures: Evidence for Antiferromagnetic Coupling of Fe Layers across Cr Interlayers*. Phys. Rev. Lett., **57**, 2442 (1986).
- [10] W. Thomson. *On the Electro-Dynamic Qualities of Metals: Effects of Magnetization on the Electric Conductivity of Nickel and of Iron*. Proc. R. Soc. London, **8**, 546 (1856).
- [11] T. Valet and A. Fert. *Theory of the perpendicular magnetoresistance in magnetic multilayers*. Phys. Rev. B, **48**, 7099 (1993).

- [12] S. Zhang and P. M. Levy. *Conductivity perpendicular to the plane of multilayered structures*. J. Appl. Phys., **69**, 4786 (1991).
- [13] J. Bass and W. Pratt. *Current-perpendicular (CPP) magnetoresistance in magnetic metallic multilayers*. J. Magn. Magn. Mater., **200**, 274 (1999).
- [14] M. Gijs, S. Lenczowski and J. Giesbers. *Perpendicular giant magnetoresistance of microstructured Fe/Cr magnetic multilayers from 4.2 to 300 K*. Phys. Rev. Lett., **70**, 3343 (1993).
- [15] L. Piraux, J. M. George, J. F. Despres, C. Leroy, E. Ferain, R. Legras, K. Ounadjela and A. Fert. *Giant magnetoresistance in magnetic multilayered nanowires*. Appl. Phys. Lett., **65**, 2484 (1994).
- [16] W. Pratt, S.-F. Lee, J. Slaughter, R. Loloee, P. Schroeder and J. Bass. *Perpendicular giant magnetoresistances of Ag/Co multilayers*. Phys. Rev. Lett., **66**, 3060 (1991).
- [17] M. Gijs and M. Okada. *Magnetoresistance study of Fe/Cr magnetic multilayers: Interpretation with the quantum model of giant magnetoresistance*. Phys. Rev. B, **46**, 2908 (1992).
- [18] R. E. Camley and J. Barnaś. *Theory of giant magnetoresistance effects in magnetic layered structures with antiferromagnetic coupling*. Phys. Rev. Lett., **63**, 664 (1989).
- [19] P. Levy, S. Zhang and A. Fert. *Electrical conductivity of magnetic multilayered structures*. Phys. Rev. Lett., **65**, 1643 (1990).
- [20] N. F. Mott. *The Electrical Conductivity of Transition Metals*. Proc. R. Soc. A Math. Phys. Eng. Sci., **153**, 699 (1936).
- [21] A. Fert and I. Campbell. *Two-Current Conduction in Nickel*. Phys. Rev. Lett., **21**, 1190 (1968).
- [22] A. Fert and I. A. Campbell. *Transport Properties of Ferromagnetic Transition Metals*. Le J. Phys. Colloq., **32**, C1 (1971).
- [23] B. Loegel and F. Gautier. *Origine de la resistivite dans le cobalt et ses alliages dilues*. J. Phys. Chem. Solids, **32**, 2723 (1971).
- [24] A. Fert and I. A. Campbell. *Electrical resistivity of ferromagnetic nickel and iron based alloys*. J. Phys. F Met. Phys., **6**, 849 (1976).
- [25] A. Fert. *Nobel Lecture: Origin, development, and future of spintronics*. Rev. Mod. Phys., **80**, 1517 (2008).
- [26] A. Fert and L. Piraux. *Magnetic nanowires*. J. Magn. Magn. Mater., **200**, 338 (1999).
- [27] F. J. Albert, J. A. Katine, R. A. Buhrman and D. C. Ralph. *Spin-polarized current switching of a Co thin film nanomagnet*. Appl. Phys. Lett., **77**, 3809 (2000).
- [28] M. Johnson and R. Silsbee. *Thermodynamic analysis of interfacial transport and of the thermomagnetolectric system*. Phys. Rev. B, **35**, 4959 (1987).

- [29] C. Chappert, A. Fert and F. N. Van Dau. *The emergence of spin electronics in data storage*. Nat. Mater., **6**, 813 (2007).
- [30] S. S. P. Parkin. *Giant Magnetoresistance in Magnetic Nanostructures*. Annu. Rev. Mater. Sci., **25**, 357 (1995).
- [31] S. Parkin, C. Kaiser, A. Panchula, K. Roche and M. Samant. *Magnetically engineered spintronic sensors and memory*. Proc. IEEE, **91**, 661 (2003).
- [32] H. Ohnishi, Y. Kondo and K. Takayanagi. *Quantized conductance through individual rows of suspended gold atoms*. Nature, **395**, 2 (1998).
- [33] A. I. Yanson, G. Rubio Bollinger, H. E. van den Brom, N. Agraït and J. M. van Ruitenbeek. *Formation and manipulation of a metallic wire of single gold atoms*. Nature, **395**, 783 (1998).
- [34] E. Scheer, P. Joyez, D. Esteve, C. Urbina and M. Devoret. *Conduction Channel Transmissions of Atomic-Size Aluminum Contacts*. Phys. Rev. Lett., **78**, 3535 (1997).
- [35] N. Agraït, A. L. Yeyatib and J. M. van Ruitenbeek. *Quantum properties of atomic-sized conductors*. Phys. Rep., **377**, 81 (2003).
- [36] N. Néel, J. Kröger and R. Berndt. *Quantized Conductance of a Single Magnetic Atom*. Phys. Rev. Lett., **102**, 086805 (2009).
- [37] G. Binnig and H. Rohrer. *Scanning tunneling microscopy*. Helv. Phys. Acta, **55**, 726 (1982).
- [38] W. Wulfhekel and J. Kirschner. *Spin-polarized scanning tunneling microscopy on ferromagnets*. Appl. Phys. Lett., **75**, 1944 (1999).
- [39] A. M. Moore and P. S. Weiss. *Functional and spectroscopic measurements with scanning tunneling microscopy*. Annu. Rev. Anal. Chem. (Palo Alto, Calif.), **1**, 857 (2008).
- [40] R. Wiesendanger. *Spin mapping at the nanoscale and atomic scale*. Rev. Mod. Phys., **81**, 1495 (2009).
- [41] J. Moreland and J. W. Ekin. *Electron tunneling experiments using Nb-Sn “break” junctions*. J. Appl. Phys., **58**, 3888 (1985).
- [42] A. R. Champagne, A. N. Pasupathy and D. C. Ralph. *Mechanically adjustable and electrically gated single-molecule transistors*. Nano Lett., **5**, 305 (2005).
- [43] J. I. Pascual, J. Méndez, J. Gómez-Herrero, A. M. Baró, N. Garcia, U. Landman, W. D. Luedtke, E. N. Bogachek and H. P. Cheng. *Properties of metallic nanowires: from conductance quantization to localization*. Science, **267**, 1793 (1995).
- [44] M. Büttiker, Y. Imry, R. Landauer and S. Pinhas. *Generalized many-channel conductance formula with application to small rings*. Phys. Rev. B, **31**, 6207 (1985).
- [45] J. L. Costa-Krämer. *Conductance quantization at room temperature in magnetic and nonmagnetic metallic nanowires*. Phys. Rev. B, **55**, R4875 (1997).

- [46] T. Ono, Y. Ooka, H. Miyajima and Y. Otani.  *$2e^2/h$  to  $e^2/h$  switching of quantum conductance associated with a change in nanoscale ferromagnetic domain structure.* Appl. Phys. Lett., **75**, 1622 (1999).
- [47] B. Ludoph and J. Ruitenbeek. *Conductance fluctuations as a tool for investigating the quantum modes in atomic-size metallic contacts.* Phys. Rev. B, **61**, 2273 (2000).
- [48] C. Sirvent, J. Rodrigo, S. Vieira, L. Jurczyszyn, N. Mingo and F. Flores. *Conductance step for a single-atom contact in the scanning tunneling microscope: Noble and transition metals.* Phys. Rev. B, **53**, 16086 (1996).
- [49] E. Emberly and G. Kirczenow. *Electron standing-wave formation in atomic wires.* Phys. Rev. B, **60**, 6028 (1999).
- [50] V. Stepanyuk, P. Bruno, A. Klavsyuk, A. Baranov, W. Hergert, A. Saletsky and I. Mertig. *Structure and quantum effects in atomic-sized contacts.* Phys. Rev. B, **69**, 033302 (2004).
- [51] A. Smogunov, A. Dal Corso and E. Tosatti. *Ballistic conductance of magnetic Co and Ni nanowires with ultrasoft pseudopotentials.* Phys. Rev. B, **70**, 045417 (2004).
- [52] A. Dal Corso, A. Smogunov and E. Tosatti. *Ab initio ballistic conductance with spin-orbit coupling: Application to monoatomic wires.* Phys. Rev. B, **74**, 045429 (2006).
- [53] A. Rocha, T. Archer and S. Sanvito. *Search for magnetoresistance in excess of 1000% in Ni point contacts: Density functional calculations.* Phys. Rev. B, **76**, 054435 (2007).
- [54] A. Smogunov, A. Dal Corso, A. Delin, R. Weht and E. Tosatti. *Colossal magnetic anisotropy of monatomic free and deposited platinum nanowires.* Nat. Nanotechnol., **3**, 22 (2008).
- [55] K. Tao, I. Rungger, S. Sanvito and V. S. Stepanyuk. *Quantum conductance of a single magnetic atom: An ab initio study.* Phys. Rev. B, **82**, 085412 (2010).
- [56] E. C. Stoner. *Collective Electron Specific Heat and Spin Paramagnetism in Metals.* Proc. R. Soc. A, **154**, 656 (1936).
- [57] J. Krans, C. Muller, I. Yanson, T. Govaert, R. Hesper and J. van Ruitenbeek. *One-atom point contacts.* Phys. Rev. B, **48**, 14721 (1993).
- [58] R. Smit, C. Untiedt, A. Yanson and J. van Ruitenbeek. *Common Origin for Surface Reconstruction and the Formation of Chains of Metal Atoms.* Phys. Rev. Lett., **87**, 266102 (2001).
- [59] C. Untiedt, D. Dekker, D. Djukic and J. van Ruitenbeek. *Absence of magnetically induced fractional quantization in atomic contacts.* Phys. Rev. B, **69**, 81401 (2004).
- [60] N. García, M. Muñoz and Y.-W. Zhao. *Magnetoresistance in excess of 200% in Ballistic Ni Nanocontacts at Room Temperature and 100 Oe.* Phys. Rev. Lett., **82**, 2923 (1999).
- [61] W.-C. Chiang, C. Ritz, K. Eid, R. Loloee, W. Pratt and J. Bass. *Search for mean-free-path effects in current-perpendicular-to-plane magnetoresistance.* Phys. Rev. B, **69**, 184405 (2004).

- [62] C. Obermair, F.-Q. Xie and T. Schimmel. *The Single-Atom Transistor: perspectives for quantum electronics on the atomic-scale*. Europhys. News, **41**, 25 (2010).
- [63] E. A. Osorio, T. Bjørnholm, J.-M. Lehn, M. Ruben and H. S. J. van der Zant. *Single-molecule transport in three-terminal devices*. J. Phys. Condens. Matter, **20**, 374121 (2008).
- [64] H. Park, A. K. L. Lim, A. P. Alivisatos, J. Park and P. L. McEuen. *Fabrication of metallic electrodes with nanometer separation by electromigration*. Appl. Phys. Lett., **75**, 301 (1999).
- [65] S. W. Kim, Y. Hashimoto, Y. Iye and S. Katsumoto. *Novel blockade due to spin-filtering with spin-orbit interaction*. J. Phys. Conf. Ser., **400**, 42032 (2012).
- [66] J. Barnaś and A. Fert. *Magnetoresistance Oscillations due to Charging Effects in Double Ferromagnetic Tunnel Junctions*. Phys. Rev. Lett., **80**, 1058 (1998).
- [67] S. Mitani, S. Takahashi, K. Takanashi, K. Yakushiji, S. Maekawa and H. Fujimori. *Enhanced Magnetoresistance in Insulating Granular Systems: Evidence for Higher-Order Tunneling*. Phys. Rev. Lett., **81**, 2799 (1998).
- [68] L. Schelp, A. Fert, F. Fettar, P. Holody, S. Lee, J. Maurice, F. Petroff and A. Vaurès. *Spin-dependent tunneling with Coulomb blockade*. Phys. Rev. B, **56**, R5747 (1997).
- [69] S. Takahashi and S. Maekawa. *Effect of Coulomb Blockade on Magnetoresistance in Ferromagnetic Tunnel Junctions*. Phys. Rev. Lett., **80**, 1758 (1998).
- [70] K. K. Likharev. *Single-electron devices and their applications*. Proc. IEEE, **87**, 606 (1999).
- [71] D. V. Averin and K. K. Likharev. *Coulomb blockade of single-electron tunneling, and coherent oscillations in small tunnel junctions*. J. Low Temp. Phys., **62**, 345 (1986).
- [72] T. Fulton and G. Dolan. *Observation of single-electron charging effects in small tunnel junctions*. Phys. Rev. Lett., **59**, 109 (1987).
- [73] Y. P. Lin, J. I. Perez-Barraza, M. K. Husain, F. M. Alkhalil, N. Lambert, D. A. Williams, A. J. Ferguson, H. M. H. Chong and H. Mizuta. *VLSI Compatible Parallel Fabrication of Scalable Few Electron Silicon Quantum Dots*. IEEE Trans. Nanotechnol., **12**, 897 (2013).
- [74] R. Parekh, A. Beaumont, J. Beauvais and D. Drouin. *Simulation and Design Methodology for Hybrid SET-CMOS Integrated Logic at 22-nm Room-Temperature Operation*. IEEE Trans. Electron Devices, **59**, 918 (2012).
- [75] J. R. Hauptmann, J. Paaske and P. E. Lindelof. *Electric-field-controlled spin reversal in a quantum dot with ferromagnetic contacts*. Nat. Phys., **4**, 373 (2008).
- [76] J. S. Lee, J.-W. Park, J. Y. Song and J. Kim. *Asymmetric magnetoconductance and magneto-Coulomb effect in a carbon nanotube single electron transistor*. Nanotechnology, **24**, 195201 (2013).

- [77] S. Lipiński and D. Krychowski. *Spin-polarized current and shot noise in a carbon nanotube quantum dot in the Kondo regime*. Phys. Rev. B, **81**, 115327 (2010).
- [78] H. Yang, M. E. Itkis, R. Moriya, C. Rettner, J.-S. Jeong, D. S. Pickard, R. C. Haddon and S. S. P. Parkin. *Nonlocal spin transport in single-walled carbon nanotube networks*. Phys. Rev. B, **85**, 52401 (2012).
- [79] P. Tedrow and R. Meservey. *Spin-Dependent Tunneling into Ferromagnetic Nickel*. Phys. Rev. Lett., **26**, 192 (1971).
- [80] M. Julliere. *Tunneling between ferromagnetic films*. Phys. Lett. A, **54**, 225 (1975).
- [81] J. S. Moodera, L. R. Kinder, T. M. Wong and R. Meservey. *Large Magnetoresistance at Room Temperature in Ferromagnetic Thin Film Tunnel Junctions*. Phys. Rev. Lett., **74**, 3273 (1995).
- [82] X.-F. Han, T. Daibou, M. Kamijo, K. Yaoita, H. Kubota, Y. Ando and T. Miyazaki. *High-Magnetoresistance Tunnel Junctions Using  $\text{Co}_{75}\text{Fe}_{25}$  Ferromagnetic Electrodes*. Jpn. J. Appl. Phys., **39**, L439 (2000).
- [83] M. Tsunoda, K. Nishikawa, S. Ogata and M. Takahashi. *60% magnetoresistance at room temperature in  $\text{Co-Fe/Al-O/Co-Fe}$  tunnel junctions oxidized with  $\text{Kr-O}_2$  plasma*. Appl. Phys. Lett., **80**, 3135 (2002).
- [84] M. Bibes, M. Bowen, A. Bartheélémy, A. Anane, K. Bouzehouane, C. Carrétéro, E. Jacquet, J.-P. Contour and O. Durand. *Growth and characterization of  $\text{TiO}_2$  as a barrier for spin-polarized tunneling*. Appl. Phys. Lett., **82**, 3269 (2003).
- [85] J. Zhu and C. Park. *Magnetic tunnel junctions*. Mater. Today, **9**, 36 (2006).
- [86] K. Kazuo and H. Akimoto. *TMR Film and Head Technologies*. FUJITSU Sci. Tech. J, **42**, 139 (2006).
- [87] B. M. Karanov and V. P. Krainov. *WKB Approximation in Atomic Physics*. Springer Berlin Heidelberg (2013).
- [88] Y. Ando, M. Hayashi, S. Iura, K. Yaoita, C. C. Yu, H. Kubota and T. Miyazaki. *Growth mechanism of thin insulating layer in ferromagnetic tunnel junctions prepared using various oxidation methods*. J. Phys. D. Appl. Phys., **35**, 2415 (2002).
- [89] M. K. Ho, C. H. Tsang, R. E. Fontana, S. S. Parkin, K. J. Carey, S. MacDonald, P. C. Arnett and J. O. Moore. *Study of magnetic tunnel junction read sensors*. IEEE Trans. Magn., **37**, 1691 (2001).
- [90] J. Nowak, P. Kolbo, E. Linville, D. Saunders, E. Murdock and P. Ryan. *Spin tunneling heads above  $20 \text{ Gb/in}^2$* . IEEE Trans. Magn., **38**, 78 (2002).
- [91] G.-X. Miao, M. Münzenberg and J. S. Moodera. *Tunneling path toward spintronics*. Reports Prog. Phys., **74**, 36501 (2011).
- [92] W. Butler, X.-G. Zhang, T. Schulthess and J. MacLaren. *Spin-dependent tunneling conductance of  $\text{Fe-MgO-Fe}$  sandwiches*. Phys. Rev. B, **63**, 54416 (2001).

- [93] S. S. P. Parkin, C. Kaiser, A. Panchula, P. M. Rice, B. Hughes, M. Samant and S.-H. Yang. *Giant tunnelling magnetoresistance at room temperature with MgO (100) tunnel barriers*. Nat. Mater., **3**, 862 (2004).
- [94] S. Ikeda, J. Hayakawa, Y. Ashizawa, Y. M. Lee, K. Miura, H. Hasegawa, M. Tsunoda, F. Matsukura and H. Ohno. *Tunnel magnetoresistance of 604% at 300 K by suppression of Ta diffusion in CoFeB/MgO/CoFeB pseudo-spin-valves annealed at high temperature*. Appl. Phys. Lett., **93**, 82508 (2008).
- [95] S. Yuasa and D. D. Djayaprawira. *Giant tunnel magnetoresistance in magnetic tunnel junctions with a crystalline MgO(001) barrier*. J. Phys. D. Appl. Phys., **40**, R337 (2007).
- [96] S. Yuasa, T. Nagahama, A. Fukushima, Y. Suzuki and K. Ando. *Giant room-temperature magnetoresistance in single-crystal Fe/MgO/Fe magnetic tunnel junctions*. Nat. Mater., **3**, 868 (2004).
- [97] S. Fusil, V. Garcia, A. Barthélémy and M. Bibes. *Magnetoelectric Devices for Spintronics*. Annu. Rev. Mater. Res., **44**, 140321171007006 (2013).
- [98] S. Bader and S. Parkin. *Spintronics*. Annu. Rev. Condens. Matter Phys., **1**, 71 (2010).
- [99] A. Brataas, A. D. Kent and H. Ohno. *Current-induced torques in magnetic materials*. Nat. Mater., **11**, 372 (2012).
- [100] J. Slonczewski. *Current-driven excitation of magnetic multilayers*. J. Magn. Magn. Mater., **159**, L1 (1996).
- [101] L. Berger. *Emission of spin waves by a magnetic multilayer traversed by a current*. Phys. Rev. B, **54**, 9353 (1996).
- [102] S. S. P. Parkin, M. Hayashi and L. Thomas. *Magnetic domain-wall racetrack memory*. Science, **320**, 190 (2008).
- [103] L. Esaki, P. Stiles and S. Molnar. *Magnetointernal Field Emission in Junctions of Magnetic Insulators*. Phys. Rev. Lett., **19**, 852 (1967).
- [104] J. Moodera, X. Hao, G. Gibson and R. Meservey. *Electron-Spin Polarization in Tunnel Junctions in Zero Applied Field with Ferromagnetic EuS Barriers*. Phys. Rev. Lett., **61**, 637 (1988).
- [105] J. Moodera, R. Meservey and X. Hao. *Variation of the electron-spin polarization in EuSe tunnel junctions from zero to near 100% in a magnetic field*. Phys. Rev. Lett., **70**, 853 (1993).
- [106] R. H. Fowler and L. Nordheim. *Electron Emission in Intense Electric Fields*. Proc. R. Soc. A Math. Phys. Eng. Sci., **119**, 173 (1928).
- [107] J. S. Moodera, T. S. Santos and T. Nagahama. *The phenomena of spin-filter tunnelling*. J. Phys. Condens. Matter, **19**, 165202 (2007).

- [108] P. Tedrow, J. Tkaczyk and A. Kumar. *Spin-Polarized Electron Tunneling Study of an Artificially Layered Superconductor with Internal Magnetic Field: EuO-Al*. Phys. Rev. Lett., **56**, 1746 (1986).
- [109] E. Negusse, J. Holroyd, M. Liberati, J. Dvorak, Y. U. Idzerda, T. S. Santos, J. S. Moodera and E. Arenholz. *Effect of electrode and EuO thickness on EuO-electrode interface in tunneling spin filter*. J. Appl. Phys., **99**, 08E507 (2006).
- [110] N. Jutong, I. Rungger, C. Schuster, U. Eckern, S. Sanvito and U. Schwingenschlögl. *Electronic transport through EuO spin-filter tunnel junctions*. Phys. Rev. B, **86**, 205310 (2012).
- [111] J. G. Simmons. *Generalized Formula for the Electric Tunnel Effect between Similar Electrodes Separated by a Thin Insulating Film*. J. Appl. Phys., **34**, 1793 (1963).
- [112] C. Mitra and W. Lambrecht. *Magnetic exchange interactions in the gadolinium pnictides from first principles*. Phys. Rev. B, **78**, 134421 (2008).
- [113] P. Larson and W. Lambrecht. *Electronic structure of Gd pnictides calculated within the LSDA+U approach*. Phys. Rev. B, **74**, 085108 (2006).
- [114] C. Aerts, P. Strange, M. Horne, W. Temmerman, Z. Szotek and A. Svane. *Half-metallic to insulating behavior of rare-earth nitrides*. Phys. Rev. B, **69**, 045115 (2004).
- [115] A. Petukhov, W. Lambrecht and B. Segall. *Electronic structure of rare-earth pnictides*. Phys. Rev. B, **53**, 4324 (1996).
- [116] B. M. Ludbrook, I. L. Farrell, M. Kuebel, B. J. Ruck, A. R. H. Preston, H. J. Trodahl, L. Ranno, R. J. Reeves and S. M. Durbin. *Growth and properties of epitaxial GdN*. J. Appl. Phys., **106**, 063910 (2009).
- [117] A. Pal, K. Senapati, Z. H. Barber and M. G. Blamire. *Electric-field-dependent spin polarization in GdN spin filter tunnel junctions*. Adv. Mater., **25**, 5581 (2013).
- [118] K. Senapati, M. G. Blamire and Z. H. Barber. *Spin-filter Josephson junctions*. Nat. Mater., **10**, 849 (2011).
- [119] L. H. Thomas. *The calculation of atomic fields*. Math. Proc. Cambridge Philos. Soc., **23**, 542 (1927).
- [120] D. R. Hartree. *The Wave Mechanics of an Atom with a Non-Coulomb Central Field. Part II. Some Results and Discussion*. Math. Proc. Cambridge Philos. Soc., **24**, 111 (1928).
- [121] P. Hohenberg and W. Kohn. *Inhomogeneous electron gas*. Phys. Rev., **136**, B864 (1964).
- [122] W. Kohn and L. J. Sham. *Self-Consistent Equations Including Exchange and Correlation Effects*. Phys. Rev., **140**, A1133 (1965).
- [123] D. M. Ceperley and B. J. Alder. *Ground State of the Electron Gas by a Stochastic Method*. Phys. Rev. Lett., **45**, 566 (1980).



- [124] J. P. Perdew and A. Zunger. *Self-interaction correction to density-functional approximations for many-electron systems*. Phys. Rev. B, **23**, 5048 (1981).
- [125] U. von Barth and L. Hedin. *A local exchange-correlation potential for the spin polarized case. I*. J. Phys. C Sol. St. Phys., **5**, 1629 (1972).
- [126] S. H. Vosko and L. Wilk. *Influence of an improved local-spin-density correlation-energy functional on the cohesive energy of alkali metals*. Phys. Rev. B, **22**, 3812 (1980).
- [127] J. Perdew, K. Burke and M. Ernzerhof. *Generalized Gradient Approximation Made Simple*. Phys. Rev. Lett., **77**, 3865 (1996).
- [128] V. I. Anisimov, J. Zaanen and O. K. Andersen. *Band theory and Mott insulators: Hubbard  $U$  instead of Stoner  $I$* . Phys. Rev. B, **44**, 943 (1991).
- [129] V. I. Anisimov, I. V. Solovyev and M. A. Korotin. *Density-functional theory and NiO photoemission spectra*. Phys. Rev. B, **48**, 16929 (1993).
- [130] J. P. Perdew, M. Levy and J. L. Balduz. *Density-Functional Theory for Fractional Particle Number: Derivative Discontinuities of the Energy*. Phys. Rev. Lett., **49**, 1691 (1982).
- [131] S. Blügel, N. Helbig, V. Meden and D. Wortmann. *Computing Solids: Models, ab-initio methods and supercomputing - JuSER*. Schriften des Forschungszentrums Jülich Reihe Schlüsseltechnologien / Key Technologies 74, ca. 1000 pp (2014) (2014).
- [132] A. A. Abrikosov, L. P. Gorkov and I. E. Dzyaloshinski. *Methods of Quantum Field Theory in Statistical Physics*. Dover Books on Physics. Dover Publications Inc. (1975).
- [133] J. Schwinger. *Brownian Motion of a Quantum Oscillator*. J. Math. Phys., **2**, 407 (1961).
- [134] L. V. Keldysh. *Diagram Technique for Nonequilibrium Processes*. J. Exp. Theor. Phys., **20**, 1018 (1965).
- [135] A. I. Larkin and Y. N. Ovchinnikov. *Nonlinear conductivity of superconductors in the mixed state*. J. Exp. Theor. Phys., **41**, 960 (1976).
- [136] J. Maciejko. *An Introduction to Nonequilibrium Many-Body Theory*. Springer (2007).
- [137] D. Langreth and J. Wilkins. *Theory of Spin Resonance in Dilute Magnetic Alloys*. Phys. Rev. B, **6**, 3189 (1972).
- [138] D. C. Langreth. *Linear and Nonlinear Response Theory with Applications*. Linear Nonlinear Electron Transp. Solids, pp. 3–32 (1976).
- [139] D. Fisher and P. Lee. *Relation between conductivity and transmission matrix*. Phys. Rev. B, **23**, 6851 (1981).
- [140] P. Ordejón, E. Artacho and J. Soler. *Self-consistent order- $N$  density-functional calculations for very large systems*. Phys. Rev. B, **53**, R10441 (1996).

- [141] J. M. Soler, E. Artacho, J. D. Gale, A. García, J. Junquera, P. Ordejón and D. Sánchez-Portal. *The SIESTA method for ab initio order-N materials simulation*. J. Phys. Condens. Matter, **14**, 2745 (2002).
- [142] N. Troullier and J. L. Martins. *Efficient pseudopotentials for plane-wave calculations*. Phys. Rev. B, **43**, 1993 (1991).
- [143] L. Kleinman and D. Bylander. *Efficacious Form for Model Pseudopotentials*. Phys. Rev. Lett., **48**, 1425 (1982).
- [144] E. Artacho, D. Sánchez-Portal, P. Ordejón, A. García and J. M. Soler. *Linear-Scaling ab-initio Calculations for Large and Complex Systems*. Phys. status solidi, **215**, 809 (1999).
- [145] J. Junquera, O. Paz, D. Sánchez-Portal and E. Artacho. *Numerical atomic orbitals for linear-scaling calculations*. Phys. Rev. B, **64**, 235111 (2001).
- [146] S. Huzinaga. *Basis sets for molecular calculations*. Computer Physics Reports, **2**, 281 (1985).
- [147] A. R. Rocha, V. M. García-Suárez, S. W. Bailey, C. J. Lambert, J. Ferrer and S. Sanvito. *Towards molecular spintronics*. Nat. Mater., **4**, 335 (2005).
- [148] A. R. Rocha, V. M. García-Suárez, S. W. Bailey, C. J. Lambert, J. Ferrer and S. Sanvito. *Spin and molecular electronics in atomically generated orbital landscapes*. Phys. Rev. B, **73**, 085414 (2006).
- [149] J. L. Mozos, P. Ordejón, M. Brandbyge, J. Taylor and K. Stokbro. *Simulations of quantum transport in nanoscale systems: application to atomic gold and silver wires*. Nanotechnology, **13**, 346 (2002).
- [150] W. Porod, Z.-A. Shao and C. Lent. *Resonance-antiresonance line shape for transmission in quantum waveguides with resonantly coupled cavities*. Phys. Rev. B, **48**, 8495 (1993).
- [151] S. Heers. *Effect of spin-orbit scattering on transport properties of low-dimensional dilute alloys*. Schlüsseltechnologien / Key Technologies. Forschungszentrums Jülich GmbH, Jülich (2011).
- [152] A. Bagrets, N. Papanikolaou and I. Mertig. *Magnetoresistance of atomic-sized contacts: An ab initio study*. Phys. Rev. B, **70**, 064410 (2004).
- [153] B. Lee, R. Alsenz, A. Ignatiev and M. Van Hove. *Surface structures of the two allotropic phases of cobalt*. Phys. Rev. B, **17**, 1510 (1978).
- [154] V. A. de la Peña O'Shea, I. d. P. R. Moreira, A. Roldán and F. Illas. *Electronic and magnetic structure of bulk cobalt: the  $\alpha$ ,  $\beta$ , and  $\varepsilon$ -phases from density functional theory calculations*. J. Chem. Phys., **133**, 024701 (2010).
- [155] B. Hardrat, N.-P. Wang, F. Freimuth, Y. Mokrousov and S. Heinze. *One-dimensional ballistic transport with FLAPW Wannier functions*. Phys. Rev. B, **85**, 245412 (2012).

- [156] N. Nilius, T. M. Wallis and W. Ho. *Development of one-dimensional band structure in artificial gold chains*. *Science*, **297**, 1853 (2002).
- [157] M. Häfner, J. Viljas, D. Frustaglia, F. Pauly, M. Dreher, P. Nielaba and J. Cuevas. *Theoretical study of the conductance of ferromagnetic atomic-sized contacts*. *Phys. Rev. B*, **77**, 104409 (2008).
- [158] A. Smogunov, A. Dal Corso and E. Tosatti. *Magnetic phenomena, spin-orbit effects, and Landauer conductance in Pt nanowire contacts: Density-functional theory calculations*. *Phys. Rev. B*, **78**, 014423 (2008).
- [159] T. R. Dasa, P. Ruiz-Díaz, O. O. Brovko and V. S. Stepanyuk. *Tailoring magnetic properties of metallic thin films with quantum well states and external electric fields*. *Phys. Rev. B*, **88**, 104409 (2013).
- [160] P. Ruiz-Díaz, T. R. Dasa and V. S. Stepanyuk. *Tuning Magnetic Anisotropy in Metallic Multilayers by Surface Charging: An Ab Initio Study*. *Phys. Rev. Lett.*, **110**, 267203 (2013).
- [161] M. Tsujikawa and T. Oda. *Finite Electric Field Effects in the Large Perpendicular Magnetic Anisotropy Surface Pt/Fe/Pt(001): A First-Principles Study*. *Phys. Rev. Lett.*, **102**, 247203 (2009).
- [162] S. Imada, A. Yamasaki, S. Suga, T. Shima and K. Takanashi. *Perpendicular magnetization of  $L1_0$ -ordered FePt films in the thinnest limit*. *Appl. Phys. Lett.*, **90**, 132507 (2007).
- [163] O. O. Brovko, P. Ruiz-Díaz, T. R. Dasa and V. S. Stepanyuk. *Controlling magnetism on metal surfaces with non-magnetic means: electric fields and surface charging*. *J. Phys. Condens. Matter*, **26**, 093001 (2014).
- [164] T. R. Dasa, P. A. Ignatiev and V. S. Stepanyuk. *Effect of the electric field on magnetic properties of linear chains on a Pt(111) surface*. *Phys. Review B*, **85**, 205447 (2012).
- [165] R. S. Mulliken. *Electronic Population Analysis on LCAO-MO Molecular Wave Functions. I*. *J. Chem. Phys.*, **23**, 1833 (1955).
- [166] O. O. Brovko, N. N. Negulyaev and V. S. Stepanyuk. *Relativistic peculiarities at stepped surfaces: Energetics and diffusion patterns obtained from ab initio calculations*. *Phys. Rev. B*, **82**, 155452 (2010).
- [167] B. Harmon, V. Antropov, A. Liechtenstein, I. Solovyev and V. Anisimov. *Calculation of magneto-optical properties for 4f systems: LSDA + Hubbard U results*. *J. Phys. Chem. Solids*, **56**, 1521 (1995).
- [168] B. Segall. *Fermi surface and energy bands of copper*. *Phys. Rev.*, **125** (1962).



# Publications (Veröffentlichungen)

The results presented in this thesis have been partly published in the following articles:  
Teile der vorliegenden Arbeit wurden an folgenden Stellen veröffentlicht:

1. Ilia N. Sivkov, Oleg O. Brovko, Valeri S. Stepanyuk,  
*Spin-polarized transport properties of GdN nanocontacts*,  
Phys. Rev. B **89**, 195419 (2014)
2. Ilia N. Sivkov, Oleg O. Brovko, Dmitry I. Bazhanov, Valeri S. Stepanyuk,  
*Emergence of high spin polarization of conductance in atomic-size Co–Au contacts*,  
Phys. Rev. B **89**, 075436 (2014)



# Curriculum vitae (Lebenslauf)

<b>Name</b>	Ilia N. Sivkov
<b>Geburtsdatum</b>	02.12.1987
<b>Geburtsort</b>	Krasnouralsk, Russland
<b>Staatsangehörigkeit</b>	Russisch
<b>Familienstand</b>	Verheiratet
<b>Adresse (privat)</b>	Kardinal-Albrecht Str., 46, D-06114, Halle/Saale
<b>Adresse (dienstlich)</b>	Weinberg 2, D-06120, Halle/Saale

## Ausbildung und Qualifikation

<b>1994–2002</b>	Primary school, Krasnouralsk (Russland)
<b>2002–2004</b>	Specialized Educational Scientific Center of Ural State University, Ekaterinburg (Russland)
<b>2004–2010</b>	Ural State University, Physics Department, Ekaterinburg (Russland)
<b>2011-present</b>	Doktorand and der Martin-Luther-Universität Halle-Wittenberg und der International Max-Planck Research School for Nanoscience and Technology, wissenschaftlicher Mitarbeiter am Max-Planck-Institut für Mikrostrukturphysik, Halle, Deutschland





# Erklärung

Ich versichere hiermit, die vorliegende Dissertation

## **Tuning spin-dependent transport properties of atomic-scale junctions: an *ab initio* Study**

selbständig und ohne fremde Hilfe verfasst und keine anderen als die von mir angegebenen Quellen und Hilfsmittel verwendet zu haben. Den benutzten Werken wörtlich oder inhaltlich entnommene Stellen sind als solche gekennzeichnet.

Halle (Saale), 03.11.2015

Ilia N. Sivkov



# Erklärung

Ich versichere hiermit, dass ich mich an keiner wissenschaftlichen Hochschule im Geltungsbereich des deutschen Grundgesetzes bereits früher um den Doktorgrad beworben habe.

Halle (Saale), 03.11.2015

Ilia N. Sivkov



# Acknowledgments

I would like to acknowledge the large support of my supervisor Prof. Dr. Valeriy Stepanyuk and my mentor Prof. Dr. Wolfram Hergert. Also I am very thankful for the help in science and preparation of the dissertation to my colleagues: Oleg Brovko, Tamene R. DASA, Pedro Ruiz-Díaz, Srijan K. Saha and to former members of the our group: Pavel Ignatiev, Larissa Niebergall and Kun Tao. Special thanks to Ivan Rungger for the useful discussions and advices, regarding to the main calculation method, used in the current work.

For the help in administrative questions and formalities I want to thank the secretary of the theory department Ina Goffin. Many thanks to our system administrator Udo Schmidt for the support and help in setting up all the computational facilities.

I am very grateful to the head of the theory department Prof. Dr. Eberhard Gross and the director of the Max-Planck Institute of Microstructure Physics Prof. Dr. Jürgen Kirschner for the very interesting working environment.

Also I sincerely thank Maria Santo for her help in accommodation in Halle. And, finally, great thanks to my wife Marina Sivkova for the support during all these three years of PhD.

Once again thank you all!